12-2016

Studies of Uncertainties in Smart Grid: Wind Power Generation and Wide-Area Communication

Can Huang
University of Tennessee, Knoxville, chuang16@vols.utk.edu

To the Graduate Council:

I am submitting herewith a dissertation written by Can Huang entitled "Studies of Uncertainties in Smart Grid: Wind Power Generation and Wide-Area Communication." I have examined the final electronic copy of this dissertation for form and content and recommend that it be accepted in partial fulfillment of the requirements for the degree of Doctor of Philosophy, with a major in Electrical Engineering.

Fangxing Li, Major Professor

We have read this dissertation and recommend its acceptance:

Yilu Liu, Leon M. Tolbert, Xueping Li

Accepted for the Council:

Carolyn R. Hodges

Vice Provost and Dean of the Graduate School

(Original signatures are on file with official student records.)

Studies of Uncertainties in Smart Grid:

Wind Power Generation and Wide-Area Communication

A Dissertation Presented for the

Doctor of Philosophy

Degree

The University of Tennessee, Knoxville

Can Huang

December 2016

Acknowledgements

I would like to express my deepest gratitude to my advisor, Dr. Fangxing (Fran) Li, for his continuous guidance and support during my Ph.D. study.

I would like to thank my committee members: Dr. Yilu Liu, Dr. Leon M. Tolbert, and Dr. Xueping Li, for their time and valuable comments on my research work.

I would also like to thank all the professors and students of the CURENT who create a loving and friendly atmosphere for study and research.

At last, I would like to thank my parents for giving me tremendous understanding and support. It is their love that helps me overcome all hardships over the years.

Abstract

This research work investigates the uncertainties in Smart Grid, with special focus on the uncertain wind power generation in wind energy conversion systems (WECSs) and the uncertain wide-area communication in wide-area measurement systems (WAMSs).

For the uncertain wind power generation in WECSs, a new wind speed modeling method and an improved WECS control method are proposed, respectively. The modeling method considers the spatial and temporal distributions of wind speed disturbances and deploys a box uncertain set in wind speed models, which is more realistic for practicing engineers. The control method takes maximum power point tracking, wind speed forecasting, and wind turbine dynamics into account, and achieves a balance between power output maximization and operating cost minimization to further improve the overall efficiency of wind power generation. Specifically, through the proposed modeling and control methods, the wind power control problem is developed as a min-max optimal problem and efficiently solved with semi-definite programming.

For the uncertain communication delay and communication loss (i.e. data loss) in WAMSs, the corresponding solutions are presented. First, the real-world communication delay is measured and analyzed, and the bounded modeling method for the communication delay is proposed for wide-area applications and further applied for system-area and substation-area protection applications, respectively. The proposed bounded modeling method is expected to be an important tool in the planning, design, and operation of time-critical wide-area applications. Second, the real synchronization signal loss and synchrophasor data loss events are measured and analyzed. For the synchronization signal loss, the potential reasons and solutions are explored. For the synchrophasor data loss, a set of estimation methods are presented, including substitution, interpolation, and forecasting. The estimation methods aim to improve the accuracy and availability of WAMSs, and mitigate the effect of communication failure and data loss on wide-area applications.

Table of Contents

List of Tables

List of Figures

1 Introduction

This research work studies the uncertainties in Smart Grid, with special focus on the uncertain wind power generation and the uncertain wide-area communication. In this chapter, the research background is introduced, including Smart Grid, wind energy conversion system (WECS), and wide-area measurement system (WAMS). Also, the research objectives, the research approaches, and the dissertation organization are presented.

1.1 Research Background

1.1.1 Smart Grid

A power grid is a group of interconnected power components and systems for delivering electric power from suppliers to consumers. It primarily consists of the generation system that supplies the power, the transmission system that carries the power from suppliers to consumers, and the distribution system that feeds the power to consumers. The U.S. power grid was first deployed in 1890s (e.g., Pearl Street Station in New York City in 1885) and is evolving into Smart Grid [1]-[3].

"What is Smart Grid?" as an open question, has obtained a lively discussion in the past few years. The worldwide academic and industrial communities as well as government officials actively participate in the discussion and develop a number of different Smart Grid definitions with different perspectives. Some significant definitions are listed as follows:

The U.S. Department of Energy in 2008 stated that "*Smart Grid uses digital technology to improve reliability, security, and efficiency (both economic and energy) of the electric system from large generation, through the delivery systems to electricity consumers and a growing number of distributed-generation and storage resources"* [4].

The U.S. Department of Energy in 2013 further stated that "*Smart Grid generally refers to a class of technology people are using to bring utility electricity delivery systems into the 21st century, using computer-based remote control and automation. These systems are made possible* *by two-way communication technology and computer processing that has been used for decades in other industries"* [5].

Electric Power Research Institute (EPRI) in the U.S. explained that "*Smart Grid is the one that incorporates information and communications technology into every aspect of electricity generation, delivery and consumption in order to minimize environmental impact, enhance markets, improve reliability and service, and reduce costs and improve efficiency"* [6].

National Institute of Standards and Technology (NIST) in the U.S. defined "*Smart Grid as a planned nationwide network that uses information technology to deliver electricity efficiently, reliably, and securely. Smart Grid also can be viewed as a modernized grid that enables bidirectional flows of energy and uses two-way communication and control capabilities that will lead to an array of new functionalities and applications"* [7].

Smart Grid deployment is imperative, not just in the U.S. but around the world. For example, European Technology Platform in 2006 stated that *"Smart Grid is an electricity network that can intelligently integrate the actions of all users connected to it – generations of all users connected to it do both – in order to efficiently deliver sustainable, economic and secure electricity supplies"* [8]. State Grid Corporation of China (SGCC) in 2009 stated that "*China's Smart Grid includes all the components of a power grid, e.g., generation, transmission, substation, distribution, consumption, and dispatching components, and covers all voltage levels, with the aims of achieving the high-degree integration of optimum power flow, information flow, and business flow. China's Smart Grid uses the ultra-high voltage (UHV) transmission system as the backbone and is also called Robust Smart Grid"* [9].

Further, some researchers believed that "*Smart Grid is a concept with many elements where monitoring and control of each element in the chain of generation, transmission, distribution, and end-use allow our electricity delivery and use more efficient"* [10].

In the previous studies, Smart Grid has received a number of different definitions with different perspectives, such as a technology [5], [6] and a physical network [7], [8].

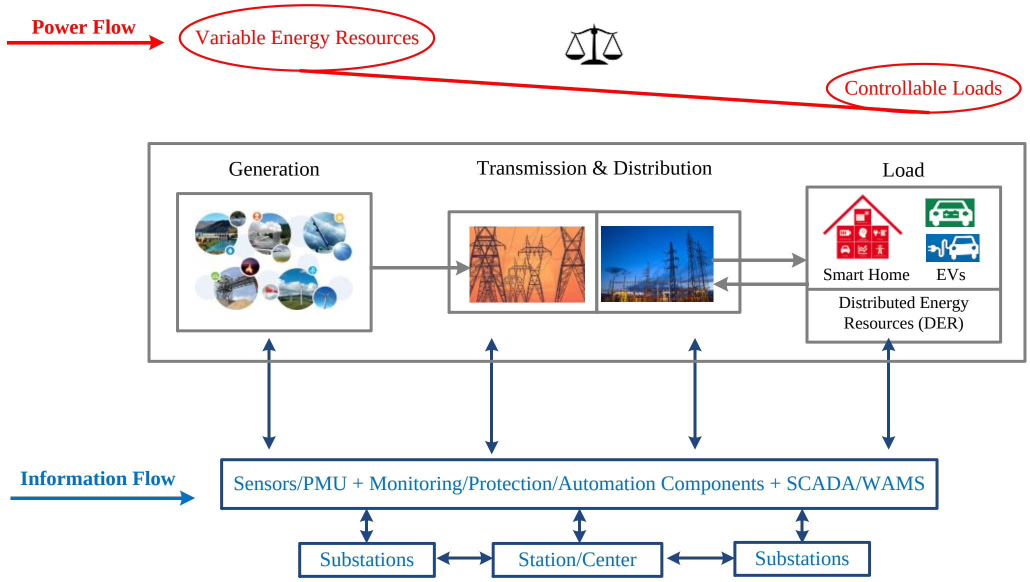

Fig. 1–1. Overview of Smart Grid.

In this dissertation, Smart Grid is viewed as the "power grid with advanced technologies" or "Smart Grid with Smart Grid technologies" as shown in Fig. 1-1, which customizes a variety of advanced technologies for power grids and further supplies, transmits, and uses electric power in a more sustainable, reliable and economic manner. Generally, the Smart Grid technologies include innovative generation technologies like renewable energy generation, distributed energy generation, and energy storage [11]-[20], advanced transmission and distribution technologies like FACTS, HVDC transmission system, and active distribution system [21]-[30], as well as some smart power usage technologies, such as smart meter, smart home, and demand response [31]-[40].

This work studies the uncertainties in Smart Grid, especially the uncertain wind power generation in WECSs and the uncertain wide-area communication in WAMSs [41]-[50].

1.1.2 Wind Power Generation

Wind power generation has been developing rapidly for its environmental, economic, and social benefits [51]-[55]. It is reported that the global wind power capacity increased from 319 GW in 2013 to 370 GW in 2014, which represented a 16% annual growth rate. It is also anticipated that the U.S. wind power market will keep steady growth in the coming years [56].

In practice, WECSs are commonly used to convert wind power to electric power and further deliver the electricity to power grids. They typically consist of aerodynamic, mechanical, and electrical components. The electrical component can further be divided into three main parts, including wind turbine generators, power electronic converters, and power grids.

A variety of WECS configurations can be broadly classified into two types (fixed-speed WECS and variable-speed WECS) or four types as shown in Fig. 1-2 (Type 1/fixed-speed WECS, Type 2/limited-variable-speed WECS, Type 3/variable-speed-with-partial-power-electronic-conversion WECS, and Type 4/variable-speed-with-full-power-electronic-conversion WECS).

Fixed-speed WECSs operate at constant speed. That means that the wind turbine rotor speed is fixed and determined, regardless of the wind speed. Fixed-speed WECSs are typically equipped with squirrel-cage induction generators (SCIG), soft starter, and capacitor bank, and directly connected to the grid as shown in Fig. 1-2 (a). An evolution of the fixed-speed WECSs are the limited-variable-speed WECS. They are normally equipped with a wound-rotor induction generator (WRIG) with variable external rotor resistance as shown in Fig. 1-2 (b).

Variable-speed WECSs are currently the most popular WECS. The variable-speed operation is possible due to the power electronic converters interface, allowing a partial or full decoupling from the grid. In general, as shown in Figs. 1-2 (c) and (d), the partial variable-speed WECS is a wind turbine with doubly-fed induction generator (DFIG) and the full variable-speed WECS a wind turbine with permanent magnet synchronous generator (PMSG).

The DFIG-based WECS is highly controllable via power electronics converters and controllers, allowing variable-speed operation over a large but still restricted range. It can either inject or absorb power from power grids, and thus actively participates at power grid voltage control.

The PMSG-based WECS due to its self-excitation property, allows operation at high power factor and efficiency. In specific, the PMSG can operate at low speeds, and thus the PMSG-based WECS does not require a gearbox. This is a big advantage of PMSG-based WECSs as the gearbox is a sensitive device in wind power generation systems [57]-[60].

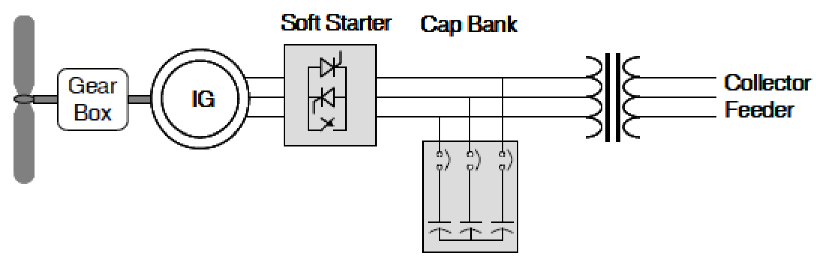

(a) Type 1 WECS

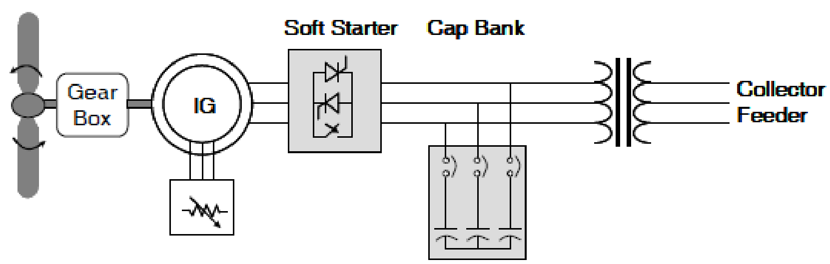

(b) Type 2 WECS

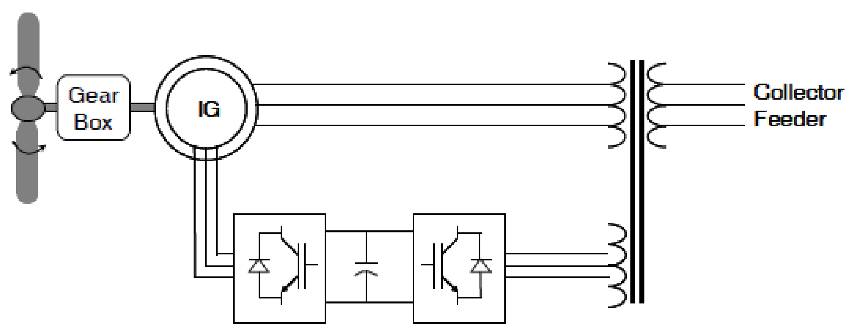

(c) Type 3 WECS

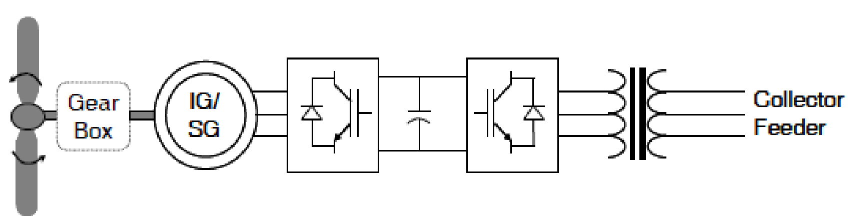

(d) Type 4 WECS

Fig. 1–2. Configurations of WECSs.

1.1.3 Wide-Area Communication

A WAMS, also known as synchrophasor system or synchronized phasor measurement system, is an important smart grid technology. It uses advanced information and communication technologies (ICTs), implements low-latency, high-precision, and time-synchronized power system measurement, and further improves power system planning, operation, and analysis at a more efficient and responsive level [61]-[70].

A typical WAMS is shown in Fig. 1-3, which primarily consists of the phasor measurement unit (PMU), phasor data concentrator (PDC), data storage, and communication network [65].

In general, the PMU is a function or a device that provides synchrophasor, frequency, and rate of change of frequency (ROCOF) measurements from voltage and/or current signals and a time synchronizing signal; the PDC is a function that collects synchrophasor data and discrete event data from multiple PMUs and/or other PDCs, aligns the data by time tags to create a time-synchronized dataset, and transmits the dataset to a control center and/or various applications; and the data storage is used to store synchrophasor data and make them conveniently available for post-event analysis.

In practice, PMUs are typically installed at a substation or a power plant, and PDCs are diversely located at a substation, a regional control room, and a centralized control room. Local PDCs aggregate and align the synchrophasor data from multiple PMUs, and mid- and higher-level PDCs collect the synchrophasor data from multiple PDCs, check the data quality, and deliver the data to a control center or a variety of applications.

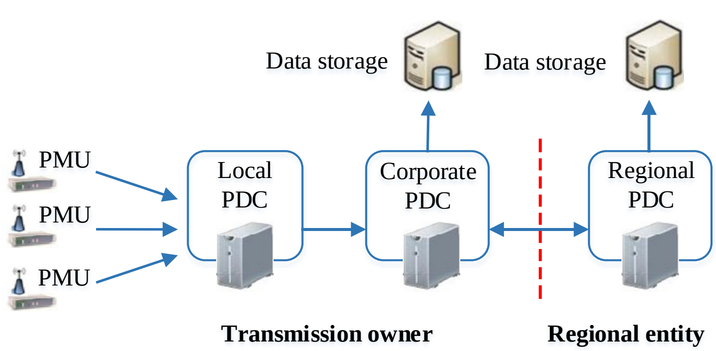

Fig. 1–3. Configuration of a WAMS.

In the mid 1980's, the first PMUs were developed by Dr. Arun Phadke and Dr. James Thorp at Virginia Tech, and now the PMU-based synchrophasor systems are globally deployed. According to the latest statistics from the North American Synchrophasor Initiative (NASPI), there are almost 2,000 commercial-grade PMUs installed across North America, and many local and regional PDCs collecting real-time, high-speed, time-synchronized power grid information.

The map in Fig. 1-4 shows the PMU locations and the way in which the synchrophasor data are being shared between power plant, transmission owners (which own the PMUs), and grid operators [65]. The synchrophasor system and synchrophasor data provide a real-time wide-area view of North America power systems, and enhance wide-area monitoring, protection & control, and other functions for better system performances.

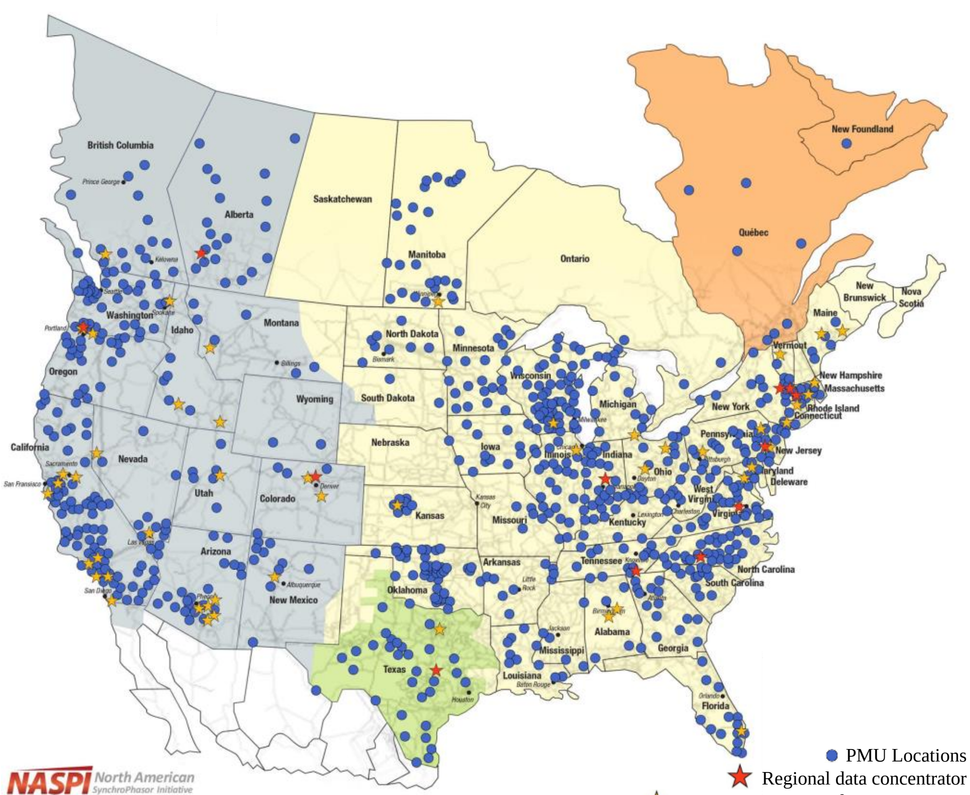

Fig. 1–4. Map of PMU locations in North America.

In addition, in 2003, a low cost and quickly deployable phasor measurement device named frequency disturbance recorder (FDR) was developed, and subsequently a wide-area frequency measurement system known as FNET or FNET/GridEye went online. The FDR, as the key component of the FNET/GridEye, measures voltage magnitude, angle, and frequency at a high precision level. The measured signals are calculated at 100 ms intervals and then transmitted across the public Internet to a PDC, where they are synchronized, analyzed, and archived. Specifically, the FDR is installed at ordinary 120 V outlets and thus is relatively inexpensive and simple to install if compared with a typical PMU at the utility side [66]-[70].

The FNET/GridEye system is currently operated by the University of Tennessee-Knoxville and Oak Ridge National Laboratory. As shown in Fig. 1-5, it collects synchrophasor data from over 200 FDRs located across the continent and around the world. Additional FDRs are constantly being installed so as to provide better observation of power grids [66].

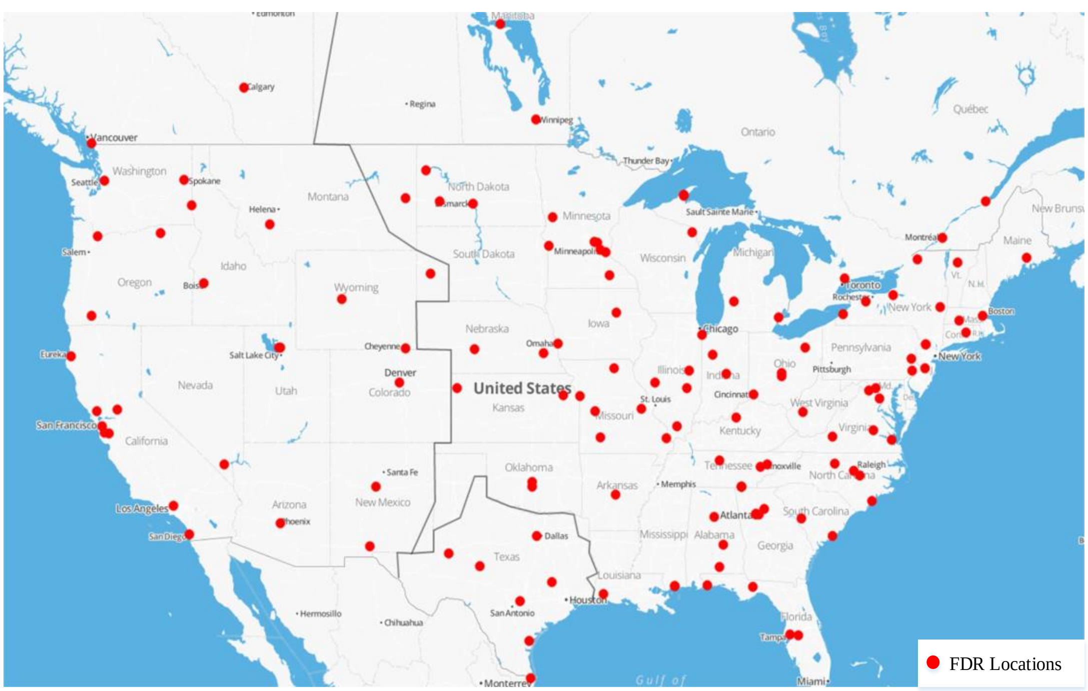

Fig. 1–5. Map of FDR locations in North America.

1.2 Research Objectives and Approaches

This research work investigates the uncertainties in Smart Grid, with special focus on the uncertain wind power generation in WECSs and the uncertain wide-area communication in WAMSs. The research objectives and approaches are briefly introduced as follows:

Study of the uncertain wind power generation in WECSs. First, the challenges of WECSs are analyzed, especially the uncertain wind power generation in WECSs. Second, the new modeling and control methods of WECSs are developed. The new modeling method considers the spatial and temporal distribution of wind speed disturbances and deploys a box uncertain set in wind speed models, which is more realistic for practicing engineers. The improved control method takes wind speed forecasting and wind turbine dynamics into account, with the aim of achieving a balance between power outputs maximization and operating costs minimization and further improving the overall efficiency of wind power generation.

Study of the uncertain communication delay and communication loss in WAMSs. In terms of the communication delay, the real-world communication delay is measured and analyzed, and the bounded modeling method of the communication delay is proposed for wide-area applications and further applied for system-area and substation-area protection applications, respectively. The proposed bounded modeling method is expected to be an important tool in the planning, design, and operation of time-critical wide-area applications. In terms of the communication loss (i.e. data loss), the real synchronization signal loss and synchrophasor data loss events are measured and analyzed. For the synchronization signal loss, the potential reasons and solutions are explored. For the synchrophasor data loss, a set of estimation methods are presented, including substitution, interpolation, and forecasting methods. The estimation methods are expected to improve the accuracy and availability of WAMSs, and mitigate the effect of communication failure and data loss on various wide-area applications.

1.3 Dissertation Organization

This research work mainly studies the uncertain wind power generation in WECSs and the uncertain wide-area communication in WAMSs, and proposes the corresponding solutions. The research work in this dissertation is organized as follows:

Chapter 2 introduces the requirements of WECSs and WAMSs, respectively, and discusses the ongoing challenges of WECSs and WAMSs, respectively. A literature review is provided covering the conventional modeling and control methods for the uncertain wind power generation and the existing solutions for the uncertain wide-area communication.

Chapter 3 investigates the uncertain wind power generation in WECSs, and proposes new modeling and control methods of WECSs, respectively. The uncertain wind power generation problem with the proposed modeling and control methods is developed as a min-max optimal problem, and efficiently solved with programming solvers. The performance of the proposed methods is demonstrated with simulation results.

Chapter 4 works on the uncertain communication delay in WAMSs. The statistics of the communication delay are provided and analyzed. The bounded modeling method of the communication delay is developed for system-area protection and substation-area protection, and further tested in the IEEE 14 bus system and IEC 61850 T2-2 substation system, respectively.

Chapter 5 focuses on the uncertain communication loss in WAMSs. The statistics of the synchronization signal loss and synchrophasor data loss events are provided and analyzed, respectively. For the synchronization signal loss, the potential reasons and solutions are explored. For the synchrophasor data loss, a set of estimation methods are presented, including substitution, interpolation, and forecasting methods, and further tested with real-world measurement data.

Chapter 6 summarizes the contribution of this dissertation and discusses the future work that may be undertaken in this area.

2 Literature Review

The research work in this dissertation studies the methods to deal with the uncertain wind power generation in WECSs and the uncertain wide-area communication in WAMSs. In this chapter, the requirements and challenges of WECSs and WAMSs are presented, respectively, and a literature review is provided covering the conventional solutions of the uncertain wind power generation in WECSs and the uncertain wide-area communication in WAMSs.

2.1 Uncertain Wind Power Generation

2.1.1 Requirements of WECSs

In general, the operating requirements of a WECS depends on its operating regions. To be specific, a characteristic curve of a variable-speed variable-pitch WECS is shown in Fig. 2-1, where v_{ci}, v_{rat}, and v_{co} are the cut-in speed, the rated speed, and the cut out speed, respectively, and the WECS operating in different regions is assigned different tasks [41]-[43].

In the partial load region ($v_{ci} \leq v \leq v_{rat}$), the WECS is primarily expected to maximize wind power capture, which is also known as maximum power point tracking (MPPT). In the full load region ($v_{rat} \leq v \leq v_{co}$), the WECS should extract the rated power (i.e., wind power regulation). These objectives can be achieved by tracking the optimal generator rotor speed ω_g^* and/or manipulating the desired pitch angle β^*.

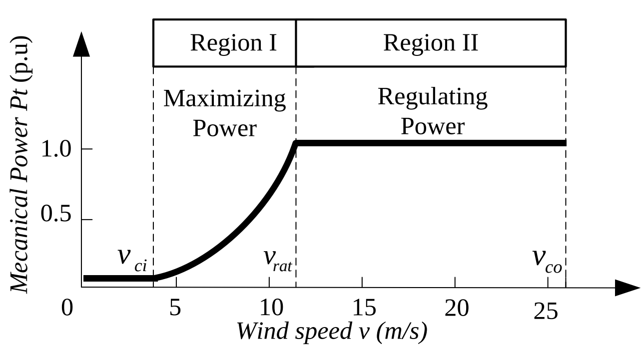

Fig. 2–1. Wind turbine characteristic curve.

In addition to generating effective electric power, alleviating aerodynamic and mechanical loads for extended installation life is also required in the control design, especially in the WECSs equipped with large-scale turbines with expensive and complex components.

Thus, the control system of a WECS is a multiple input multiple output (MIMO) system with multiple objectives. Moreover, the wind speed's randomness, the system nonlinearity, and physical constraints on control variables, such as limits on the pitch angle and the pitch angle rate, render the control design task more difficult.

2.1.2 Challenges of WECSs

Wind energy is variable and intermittent, and wind power generation presents strong uncertainties. In order to make the wind power generation stable and profitable, it is crucial to develop efficient modeling and control methods of WECSs. However, there are numerous challenges for the modeling and control of WECSs, especially with the trend of developing large-scale wind turbines and installing wind farms in low wind speed areas [41]-[43].

A. Wind Speed Modeling

Wind speed is difficult to model since it is affected by a number of factors, such as geographic location, climate characteristics, height above ground, and surface topography. Wind speed is also difficult to measure because the randomness of wind speed is subject to a spatial and temporal distribution as shown in Fig. 2-2 [41]-[43], [51]-[53].

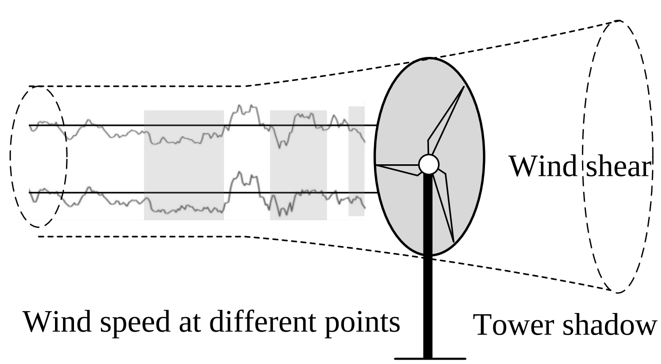

Fig. 2–2. Spatial and temporal distributions of wind speed.

First, the wind speed working on an entire turbine is different from the one working at a specific location of the turbine. This means that the measured wind speed at a particular location will not be the same as the actual wind speed at different points over the blades.

Second, the wind speed working on the turbine is different from the wind speed measured by an anemometer. In reality, the wind speed anemometer is normally installed at the rear of the nacelle, and because of the effect of wind shear and tower shadow, the real wind speed going through the blade and the tower becomes variable.

As a result, there is a measurement error between the real value and the measured value. The error may lead to a series of problems in wind power control and operation.

B. WECS Control

In wind power industry, WECSs are expected to maximize the electric power generated from the wind and minimize the overall operational cost. One challenge is the optimization of MPPT control methods in WECSs. The performance of MPPT plays a decisive role in WECS efficiency since more than 50% of the annual energy capacity for a typical turbine comes from the partial load region (wind speed below the rated speed). Unfortunately, it has been shown that a 5% error is common in conventional MPPT control methods leading to a 1%–3% energy loss, which is considered significant in the wind energy industry [71], [72].

A great deal of research effort in academia and industry has been devoted to advanced MPPT methods and the proposed approaches and experiments are primarily based on small to medium scale (1–100 kW) wind turbines. As turbines increase in size and capacity, the efficiency and quality constraints of WECSs become more difficult to attain. Optimization of MPPT methods for multi-MW wind power generation systems is worthy of further study [41]-[43], [71]-[73].

Other challenges primarily stem from the stochastic nature of wind power generation. First, the important input signal of the control system - wind speed is difficult to model or measure. Second, the gusty and intermittent wind power gives rise to the issue of drive train torque fluctuation, which is highly analogous to the cost of wind turbine operation and maintenance. This problem becomes increasingly important with the ongoing trend of installing large-scale wind turbines with expensive and complex components. Hence, there is a serious interest within the research and industrial communities to employ advanced MPPT methods with sophisticated wind speed modeling, such that various factors like economic merit of power harvesting and technical merit of alleviating mechanical damage can be taken into account collectively.

Further, as discussed before, the WECS control system is a MIMO system with multiple objectives, and the input's randomness, system nonlinearity, and physical constraints on control variables render the control design more difficult.

2.1.3 Solutions of Uncertain Wind Power Generation

A. Wind Speed Modeling Methods

The majority of the previous studies model the wind speed using the Van der Hoven spectrum, in which the wind speed is modeled with two components as follows

$$v = v_m + v_d \tag{2.1}$$

where v_m is the mean wind speed representing the long-term and slow variable component, and v_d is a disturbance describing the rapidly variable component.

Commonly, v_m is assumed to be the measured or estimated value at a given site and over a certain time period and v_d is designed as Gaussian, e.g., $\mathbf{d} \sim \mathcal{N}(\boldsymbol{\mu}, \boldsymbol{\Sigma})$ [41], [42]. However, this assumption may not hold in many cases and in the real world the disturbance does not always follow a regular probability distribution.

B. WECS Control Methods

Advanced control strategies for WECSs have been investigated over a few decades, which are broadly classified into the classic control, modern control, and intelligent control as Table 2-1.

Table 2-1 Classification of WECS control.

Control theory	Classical control	Modern control	Intelligent control
Control objective	SISO, linear time-invariant system	SISO/SIMO/MISO/MIMO, linear/nonlinear, time-invariant/time-variant, univariate/multivariate, discrete/ continuous system	Large-scale, complex structure, incomplete information, multivariate system
Analysis method	Frequency-domain approach	Time-domain approach	Time-domain approach
Mathematical model	Transfer Function	State-Space Equation	Subsystem
Mathematical tool	Laplace transform	Matrix theory, vector space theory	Cybernetics, operations research, artificial intelligence
Control method	PID control	Optimal control Robust control Adaptive control Sliding model control Predictive model control	Bayesian control Fuzzy (logic) control Neural network control Expert Systems Genetic control Intelligent agents

SISO-single input single output; SIMO-single input multiple output, and MISO-multiple input single output.

In the partial load regime, the main control objective is to capture the maximum power available from the wind. The rotor speed and the pitch angle should be controlled in a way such that the MPPT is obtained.

To achieve the MPPT, the classical PI controller is used for MPPT [74], [75]. The PI control method is simple and practical, but needs to tune the PI parameters repeatedly. Also, to cope with the system nonlinearity, a gain-scheduling linear quadratic Gaussian (LQG) method is used in [76], and a gain-scheduling H_∞ approach to control variable speed WECS in the context of linear parameter-varying (LPV) systems is proposed in [77].

In the full load regime, the main control objectives are to regulate both the generator power and the generator speed at their rated values, respectively. These objectives can be achieved by manipulating the desired pitch angle and/or the generator torque set point.

The majority of works in the literature dealing with the controller in the full load region use a decentralized approach as shown in Fig. 2-3 [74], [78]. In this approach, two separate controllers are designed to regulate the generator speed and the generator power independently. Actually, designing these two controllers is a difficult task owing to the presence of interaction between the two control loops. Moreover, this kind of control configuration often leads to large torsional torque variations and electric power fluctuations. In order to improve these drawbacks, a multivariable WECS control strategy is proposed in [78].

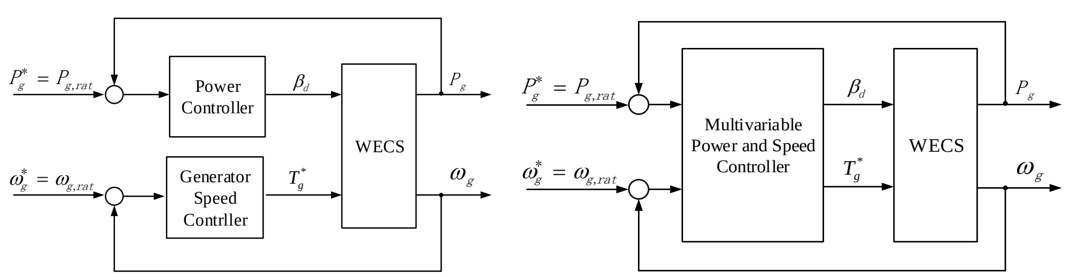

Fig. 2–3. Decentralized control method.

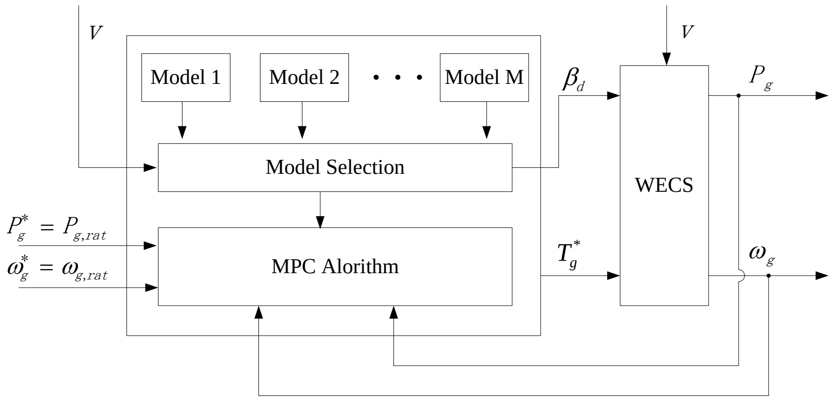

Fig. 2–4. Multivariable MPC method.

Further, the presence of two control regions with different control structures requires the ability to switch between the controllers. Several recent studies indicate that when wind speed fluctuates around its rated value, undesirable drive train transient loads and power overshoots can occur. To solve this issue, a model predictive control (MPC) based overall control strategy that can work in both the partial and the full load region is proposed as shown in Fig. 2-4 [79]. However, the MPC-based method needs to predict the disturbance of the control input in a finite horizon. Thus, ref. [79] applies a state-space model for the disturbance while parameters of the model are assumed known, which is somewhat a challenge in practice [80].

2.2 Uncertain Wide-Area Communication

2.2.1 Standards of WAMSs

In order to promote the synchrophasor system development, the NASPI, National Institute for Standards and Technology (NIST), IEEE, IEC, and electric industry (e.g., utilities, vendors, and academics) put joint effort to developing a set of synchrophasor system standards and guides. A brief review is presented below to provide a picture of the history and key points of these technical rules [45]-[46], [81]-[95].

IEEE Std. 1344-1995 (R2001), released in 1995 and reaffirmed in 2001, is the first IEEE standard for synchrophasors for power systems. It defined phasor and synchronized phasor, and specified synchronizing resources, synchronization methods, and synchrophasor message format (i.e. data frame, configuration frame, and header frame). IEEE Std. 1344-1995(R2001) defined the synchrophasor measurement in terms of the waveform sampling, timing, and basic phasor definition, and did not specify the synchrophasor communication.

IEEE Std. C37.118-2005 is the revision of IEEE Std. 1344-1995(R2001). It revised the synchronized phasor definition, and specified the synchronization requirements, accuracy requirements under steady-state conditions, and synchrophasor message format (i.e. data frame, configuration frame, header frame, and command frame). In specific, IEEE Std. C37.118-2005 introduced the total vector error (TVE) criterion to quantify synchrophasor measurements. This shifted the focus from measurement methods to measurement results, allowing the use of any method or algorithm that produces good results.

IEEE Std. C37.118-2011 is the current IEEE standard for synchrophasors for power systems. In order to gain a wider international acceptance, the IEEE and the IEC initiated a joint project in 2009 to harmonize IEEE Std. C37.118 with IEC 61850 standard. As a result, IEEE Std. C37.118-2011 is split into two parts.

The first part, IEEE Std.118.1-2011 for synchrophasor measurements, deals with synchrophasor measurements and related performance requirements. It included the steady-state synchrophasor measurements and their performance requirements in IEEE Std. C37.118-2005; it also introduced the dynamic synchrophasor measurements and frequency and ROCOF estimates, and their performance requirements. The second part, IEEE Std. C37.118.2-2011 for synchrophasor data transfer, standardizes the synchrophasor communication. It is based on the portion of IEEE Std. C37.118-2005 specifying data communication and portion of IEC 61850-90-5 standard. IEEE Std. C37.118.2-2011 allows more communication protocols and systems to be used with synchrophasor measurements and communication, which greatly promotes the development and deployment of synchrophasor systems.

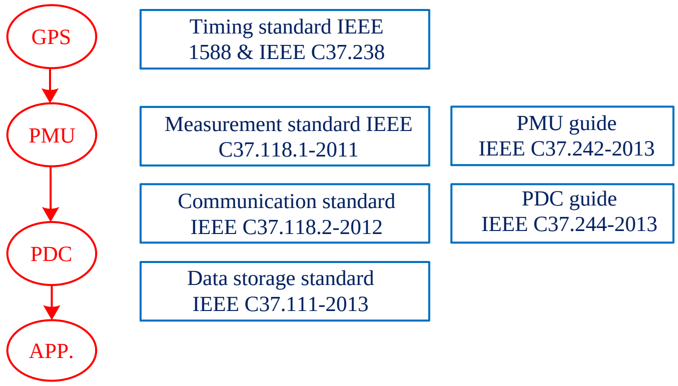

Fig. 2–5. IEEE Standards for synchrophasor systems.

In addition, IEEE Std. C37.238-2011 specifies the precision time protocol for power system applications, IEEE Std. C37.111-2013 standardizes the common format for transient data exchange (COMTRADE) for power systems, and IEEE Std. C37.242-2013 and C37.244-2013 are developed to guide PMU utilization (e.g., synchronization, calibration, testing, and installation), and PDC definitions and functions, respectively. These critical standards and guides for synchrophasor systems are compactly shown in Fig. 2-5.

2.2.1 Requirements of WAMSs

In the past decade, synchrophasor systems have become prevalent in power grids and a large number of actual and potential synchrophasor applications have been reported in the literature. These applications' classifications and data requirements and sensitivities are discussed [45].

Synchrophasor applications can be broadly classified into two categories: real-time and off-line applications. The former require real-time data and response within seconds or even sub-seconds after receiving the data; and they improve real-time operations with enhanced visibility and situational awareness, and also support wide-area protection and control actions, such as special protection scheme, remedial action scheme, emergency control sys-tem, and wide-area control system. In contrast, the latter use archived data and may be conducted off-line days or months after the data were collected; and they primarily improve power system analysis and planning, such as baselining, post-event analysis, and model calibration and validation.

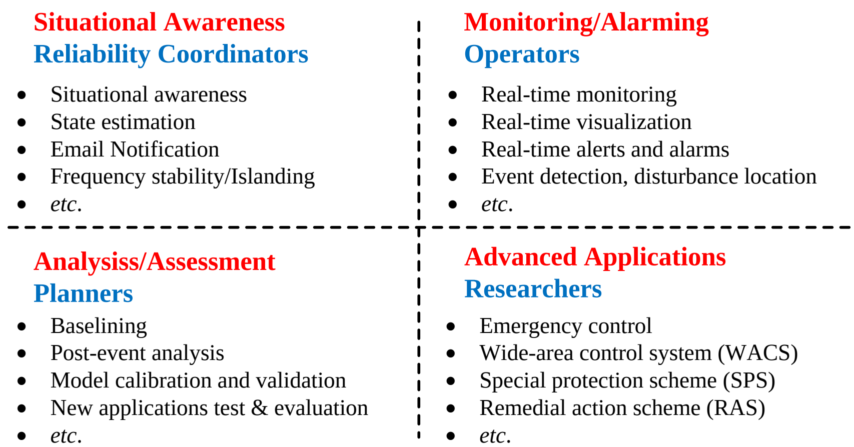

Fig. 2–6. Classification of synchrophasor applications.

Specifically, the NASPI has been working on the phasor application taxonomy. In 2008, the NASPI created a table for phasor application classification and condensed various applications into four categories as shown in Fig. 2-6, including the situational awareness, monitoring/alarming, analysis/assessment, and advanced applications [91].

Later, the applications were classified with their working fields in [92]-[93], e.g., reliability operation, market operation, planning, and others, and grouped in accordance with their maturity levels in [94], e.g., Level-1 (conceptualization), Level-2 (development), Level-3 (implementation), Level-4 (operationalized), and Level-5 (integrated and highly mature). A set of metrics to describe and characterize each maturity level were also given in [94].

In engineering, different groups of synchrophasor applications have different requirements on synchrophasor data, such as data rate, data volume, data quality, and data security. It is important to understand the variety of synchrophasor applications and their data requirements. It is also advantageous to develop a set of consistent and quantifiable data requirements for the applications, which help existing and new users learn the applications' capability and suitability in their particular scenarios. The data quality requirements for synchrophasor applications are investigated in this research.

In the past decade, an increasing number of PMUs were installed around the world and a variety of PMU-based WAMSs were available in power grids. It should be noted that most of these projects are subsidized. The technical and economic benefits of WAMSs are not fully identified, and the potentials of various WAMS applications need further explored.

In practice, the WAMS as a physical network involves communication constraints, such as uncertain communication and bad data issues. Many wide-area applications' robustness to data quality issues is relatively unknown, and their performances may be affected or even disabled due to communication failure and data flaws. Therefore, this work investigates the uncertain communication issue for synchrophasor applications.

The "data quality" term for synchrophasor applications has not been defined in the existing standards. The data quality issue in this work is characterized by three qualities, including data accuracy, data availability, and data timeliness.

Generally, data accuracy demands the synchrophasor measurements, such as phasor measurements, frequency estimates, and time synchronization, within acceptable errors; data availability requires the measurement data to be complete, consistent, and without loss; and data timeless refers to the measurement data delivered to their destinations within acceptable latencies.

Data accuracy is largely determined by PMU performances, since the measurement data are measured, digitalized, and packaged by PMUs. As aforementioned, the data accuracy requirements under steady-state and dynamic conditions are well specified in C37. 118.1-2011, and TVE is used to quantify the measurement accuracy. For example, the maximum TVE is required to be 1% in steady-state synchrophasor measurement and the corresponding maximum timing error of PMU is 26.4 μs for 60 Hz power grid (Assuming PMU has no magnitude measurement error, 1% TVE corresponds to 0.57 degree phase error or 26.4 μs timing error). Moreover, two PMU performance classes "M" class and "P" class are also standardized in C37. 118.1-2011. The former emphasizes high precision and supports applications that are sensitive to signal aliasing but immune to delays (e.g., measurement devices), whereas the latter emphasizes low latencies and is used for applications that require minimal delays in responding to dynamic changes (e.g., protective relays).

Data availability and timeliness depends on the joint performance of PMUs, PDCs, and communication links. IEEE standards mention the data loss and latency issues for synchrophasor systems and applications, but have not formalized the related quantitative requirements. In recent years, the NASPI was working on synchrophasor application classification, and attempted to define the applications' requirements on data accuracy, loss, and latency. For example, a list of applications' requirements are shown in Table 2-2, in which the applications are condensed into four categories and three metrics [45].

Table 2-2 Classification of PMU applications.

Attributes	Class A	Class B	Class C	Class D
Accuracy	4	2	4	2
Availability	4	2	3	1
Latency	4	3	1	1
Application examples	Protection & control	State estimator	Post-event analysis	Visualization & monitoring

4 stands for critical; 3 stands for important; 2 stands for somewhat important; 1 stands for not very important

Note that Table 1 only gives high-level analysis. Actually, many applications robustness to data quality issues is relatively unknown, and various applications' requirements and sensitivities on data quality still worth to be further investigated.

This section reviews synchrophasor applications' classifications and data requirements, and points out that it is necessary to formalize a set of consistent and quantifiable data quality requirements for synchrophasor applications. These requirements and technical rules can help existing and new users understand various applications' capability and suitability in their particular scenarios, and further promote the development of synchrophasor systems and enhance the performance of power grids.

2.2.2 Solutions of Uncertain Wide-Area Communication

In WAMSs, the actual measurement and communication systems inevitably involve data quality issues. For instance, a measurement device may cause a data accuracy issue because of device errors or timing signal loss, and a communication link may induce data loss and latency issues due to unintentional reasons (e.g., equipment malfunctions and communication infrastructure limits) or intentional cyber-attacks. These data quality issues may impact or even disable certain application functionalities. Consequently, a great deal of research effort in academia and industry has been devoted to addressing the data quality issue, especially the data accuracy, latency, and loss issues.

First, the data accuracy issue primarily derives from measurement equipment and devices, such as instrument transformers and PMUs. Conventional instrument transformers have inherent limitations on high-voltage measurement and isolation; while classic PMUs using discrete-Fourier-transform algorithms have a low computational burden but their accuracy degrades in the presence of frequency offsets and dynamic conditions. Accordingly, advanced instrument transformers like electronic instrument transformers [96]-[97] and alternative PMUs using sophisticated measurement algorithms [98]-[100] have been developed. Those approaches greatly improve the synchrophasor measurement accuracy under both steady-state and dynamic conditions.

Second, for the data latency, the previous researches primarily focus on three aspects 1) modeling the communication delay in theoretical and statistical perspectives, such as constant modeling, stochastic modeling, and bounded modeling [44], [101], 2) developing special protection schemes and control strategies with the consideration of latencies [102]-[105], and 3) optimizing the communication infrastructure, like communication architecture, medium, and protocols, and restricting the delay to an acceptable range [106]-[110]. Those design and approaches have been selectively used in wide-area protection & control and other advanced applications.

Further, for the data incompleteness and missing, numerous researches work on reducing the risk of data loss, such as the ones enhancing communication performance in terms of communication architecture, bandwidth, and redundancy. In addition, some researches deal with the data loss issue in a positive way. For example, a predictive control strategy for wide-area damping control was presented in [111] with the consideration of data loss and other physical constraints, and a data reconstruction method using the low-rank matrix completion approach was provided in [112], in which way the lost data could be partially recovered at a control center.

3 Uncertain Wind Power Generation in WECSs

In this chapter, the uncertain wind power generation in WECSs is studied, and improved modeling and control methods of WECSs are proposed, respectively. The uncertain wind power generation problem with the proposed modeling and control methods is developed as a min-max optimal problem, and efficiently solved with programming solvers. The performance of the proposed methods is demonstrated with simulation results.

3.1 WECS Modeling

DFIG and PMSG are the two most common applications of variable-speed variable-pitch WECSs. This work focuses on the later with respect to the dynamic characteristics of multi-pole low-speed PMSGs [60].

A typical PMSG-based WECS is shown in Fig. 3-1, consisting of aerodynamic, mechanical, and electrical parts. The wind power captured by the wind turbine is converted into mechanical power, then transformed to electric power by the generator, and finally delivered to the grid through a conversion system. The important components include the wind turbine, the pitch actuator, the drive train, and the generator. Their mathematical models are introduced as follows [41]-[43].

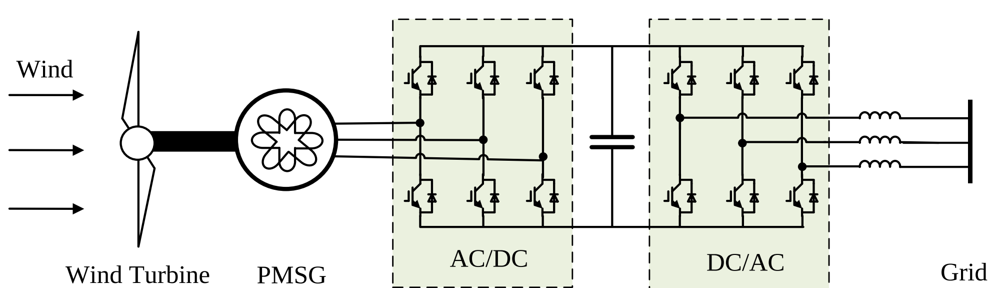

Fig. 3–1. PMSG-based WECS.

A. Wind Turbine Model

The aerodynamics power P_t captured by the wind turbine can be written as

$$P_t = \frac{1}{2}\rho\pi R^2 C_p\left(\frac{\omega_t R}{v}, \beta\right)v^3 = \frac{1}{2}\rho\pi R^2 C_p\left(\lambda, \beta\right)v^3 \tag{3.1}$$

with $C_p\left(\lambda, \beta\right) = 0.5176\left(\frac{116}{\lambda_i} - 0.4\beta - 5\right)e^{-21/\lambda_i} + 0.0068\lambda$ (3.2)

$$\frac{1}{\lambda_i} = \frac{1}{\lambda + 0.08\beta} - \frac{0.035}{\beta^3 + 1} \tag{3.3}$$

where ρ is the air density, R is the blade length, λ is the tip speed ratio (TSR) of the turbine rotational speed ω_t to the wind speed v, β is the blade pitch angle, and $C_p(\lambda, \beta)$ is the power coefficient.

The wind turbine torque T_t can be calculated as

$$T_t = \frac{P_t}{\omega_t} = \frac{\rho\pi R^5}{2\lambda^3} C_p\left(\lambda, \beta\right)\omega_t^2 \tag{3.4}$$

In addition, a wind turbine can produce its maximum power when it operates at the maximum power coefficient point $C_{p\max}(\lambda_{opt}, \beta_{opt})$, where $\lambda_{opt} = \omega_{opt} R / v$. The maximum power output from the wind turbine is given by

$$P_{t\max} = \frac{\rho\pi R^5 C_{p\max}}{2\lambda_{opt}^3}\omega_{opt}^3 = k_{opt}\omega_{opt}^3 \tag{3.5}$$

B. Pitch Actuator Model

The blade pitch angle β and its operating limits can be written respectively as

$$\dot{\beta} = (\beta^* - \beta) / \tau_\beta \tag{3.6}$$

$$\beta_{\min} \le \beta \le \beta_{\min} \tag{3.7}$$

$$\dot{\beta}_{\min} \le \dot{\beta} \le \dot{\beta}_{\min} \tag{3.8}$$

where β^* is the pitch angle set point, τ is the time constant of the pitch system, and $\bullet_{max}$ ($\bullet_{min}$) represents the constraint of •.

C. Drive Train Model

The drive train component is described by a one-mass model, since the rotors of the wind turbine and the generator are connected directly. The one-mass model can be expressed with the following expressions

$$\dot{\omega} = (T_t - T_g - F\omega) / J \tag{3.9}$$

$$T_g = \begin{cases} 0 & v < v_{ci} \\ k_{opt}\omega^2 & v_{ci} \le v \le v_{rat} \\ T_{rat} & v_{rat} < v < v_{ct} \end{cases} \tag{3.10}$$

where T_g is the generator torque, J is the turbine's moment of inertia, F is the viscous friction coefficient, and v_{ci}, v_{rat}, and v_{ct} are the cut-in speed, the rated speed, and the cut-out speed, respectively, which divide the system into three operating regions.

If the friction torque is ignored, (3.9) can be rewritten as

$$\dot{\omega} = (T_t - T_g) / J \tag{3.11}$$

D. Generator Model

Since the electrical dynamics of the generator are faster than the mechanical dynamics of the turbine, a first-order model in (13) is used to represent the electrical dynamics.

$$\dot{T}_g = (T_g^* - T_g) / \tau_g \tag{3.12}$$

where T_g^* is the set point of the generator torque and τ_g is the time constant of the generator system.

E. WECS Model

The described WECS model above can be linearized around its operating point (OP) with the following expressions.

$$
\begin{aligned}
dT_t &= \frac{\partial f}{\partial \omega_t}|_{op}\ d\omega_t + \frac{\partial f}{\partial \nu}|_{op}\ d\nu + \frac{\partial f}{\partial \beta}|_{op}\ d\beta \\
&= L_\omega d\omega_t + L_\nu d\nu + L_\beta d\beta
\end{aligned}
\tag{3.13}
$$

$$
L_\omega = \frac{\partial f}{\partial \omega_t}|_{op} = \frac{\rho\pi R^2 \nu^2}{2\omega_t}\left(-C_p(\lambda,\beta)\frac{\nu}{\omega_t} + R\frac{\partial C_p(\lambda,\beta)}{\partial \lambda}\right) \tag{3.14}
$$

$$
L_\nu = \frac{\partial f}{\partial \nu}|_{op} = \frac{\rho\pi R^2 \nu}{2}\left(3C_p(\lambda,\beta)\frac{\nu}{\omega_t} - R\frac{\partial C_p(\lambda,\beta)}{\partial \lambda}\right) \tag{3.15}
$$

$$
L_\beta = \frac{\partial f}{\partial \beta}|_{op} = \frac{\rho\pi R^2 \nu^3}{2\omega_t}\frac{\partial C_p(\lambda,\beta)}{\partial \beta} \tag{3.16}
$$

where the symbol *d* corresponds to the deviation of a variable from the OP.

In addition, the wind speed is modeled with the mean wind speed over a certain time period v_m and the wind speed disturbance v_d in (2.1). Typically, the disturbance v_d is designed as Gaussian $N(\boldsymbol{\mu},\boldsymbol{\sigma}^2)$ or Weibull $W(\boldsymbol{\alpha},\boldsymbol{\beta})$. In this work, the empirical design is replaced by a more physically relevant model called Norm-bounded disturbance. No assumption is made to the distribution of the disturbance; instead, a bound on the amplitude of the noise is assumed, e.g., $\mathbb{D}_\gamma = \{\mathbf{d} \mid \|\mathbf{d}\|_2 \le \gamma\}$. This is arguably more realistic at high latitudes and in short terms.

In this way, the state vector, the control input, and the measure output are defined as $\boldsymbol{x} = \left[d\omega\ dT_t\ dT_g\ d\beta\right]^T$, $u = \left[dT_g^*\ \ d\beta^*\right]^T$, and $y = \left[d\omega_g\ \ dP_g\right]^T$, respectively. The state space model of the linearized WECS can be written compactly as

$$
\dot{x}(t) = \tilde{A}x(t) + \tilde{B}_u u(t) + \tilde{B}_\nu \Delta\nu(t) \tag{3.17}
$$

$$
y(t) = \tilde{C}x(t) \tag{3.18}
$$

with

$$\tilde{\boldsymbol{A}} = \begin{bmatrix} 0 & \frac{1}{J} & -\frac{1}{J} & 0 \\ L_\omega & 0 & 0 & L_\beta \\ 0 & 0 & -\frac{1}{\tau_g} & 0 \\ 0 & 0 & 0 & -\frac{1}{\tau} \end{bmatrix}, \quad \tilde{\boldsymbol{B}}_{\boldsymbol{u}} = \begin{bmatrix} 0 & 0 \\ 0 & 0 \\ 1/\tau_g & 0 \\ 0 & 1/\tau \end{bmatrix}, \quad \tilde{\boldsymbol{B}}_{\boldsymbol{v}} = \begin{bmatrix} 0 \\ L_v \\ 0 \\ 0 \end{bmatrix}, \text{ and } \tilde{\boldsymbol{C}} = \begin{bmatrix} 1 & T_g \\ 0 & 0 \\ 0 & \omega_g \\ 0 & 0 \end{bmatrix}^T.$$

Thus, the discrete version of the linearized WECS can be written as follows

$$\boldsymbol{x}(k+1) = \boldsymbol{A_d}\boldsymbol{x}(k) + \boldsymbol{B_u}\boldsymbol{u}(k) + \boldsymbol{B_d}\boldsymbol{d}(k) \tag{3.19}$$

$$\boldsymbol{y}(k) = \boldsymbol{C_d}\boldsymbol{x}(k) \tag{3.20}$$

where $\boldsymbol{A_d} = e^{\tilde{A}T}$ and $[\boldsymbol{B_u}, \boldsymbol{B_d}] = \left[\int_0^T e^{\tilde{A}T}\, dt\right]\left[\tilde{\boldsymbol{B}}_{\boldsymbol{u}}, \tilde{\boldsymbol{B}}_{\boldsymbol{v}}\right]$.

To simplify the notation, we set $\boldsymbol{x} := [x(1)^T, ..., x(N)^T]^T$, $\boldsymbol{u} := [u(0)^T, ..., u(N-1)^T]^T$, $\boldsymbol{y} := [y(0)^T, ..., y(N-1)^T]^T$, and $\boldsymbol{d} := [d(0)^T, ..., d(N-1)^T]^T$.

3.2 MPPT Control

The WECS in the partial load region is expected to capture the maximum power available from the wind. The rotor speed and the pitch angle should be controlled in a way so that the power coefficient is maximized. This control is called the MPPT control.

3.2.1 Conventional MPPT

Previous research works primarily focus on three conventional MPPT algorithms, namely, TSR control, hill-climb search (HCS) control, and power signal feedback (PSF) control. These three MPPT algorithms are briefly reviewed in Table 3-1.

Table 3-1 A brief review of three conventional MPPT methods.

MPPT technique	Anemometer	Tracking reference	Prior-knowledge of system	Online updating	Complexity	Tracking speed
TSR	Required	$\omega^* = \lambda_{opt} v_m / R$	Required	No	Low	Fast
PSF	Not required	$P_g^* = k_{opt}\omega^3$	Required	No	Low	Fast
HSF	Not required	N/A	Not required	Yes	High	low

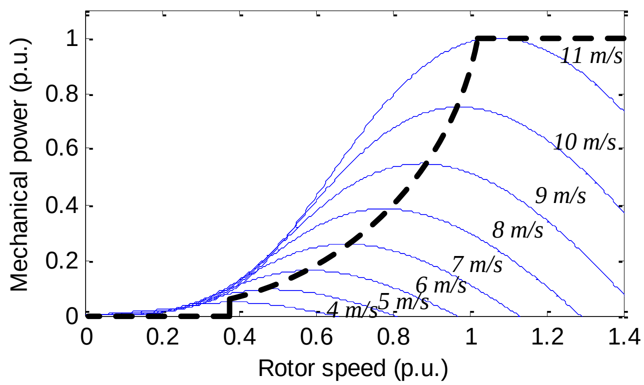

Fig. 3–2. Wind turbine characteristic curves at various wind speeds.

This work studies the WECS with anemometers in which TSR control is widely employed.

MPPT, in essence, is a tracking problem and its success largely depends on a reasonable selection of references. In TSR control, as shown in Fig. 3-2, the maximum wind points under various wind speeds are achieved by tracking the optimal rotor speed in (3.21). The TSR control method requires real-time measurement of the wind speed and thus becomes expensive and difficult to implement in practice.

$$\omega_{ref} = \frac{\lambda_{opt}}{R} v \tag{3.21}$$

3.2.2 Improved MPPT

To solve the above problem, the wind speed estimation (WSE) based MPPT control is proposed in [113]-[116], where the wind speed is estimated from the relationship between system parameters and is then used to calculate the reference value in (3.21). The WSE based MPPT control method utilizes artificial intelligence algorithms [115], [116] or data forecasting techniques [113], [114] and can estimate or predict the wind speed with acceptable accuracy and computational cost. In recent years, the prediction accuracy of advanced forecasting techniques has reached 97% in a few-minutes to 20-minutes ahead. The prediction error is even smaller with the prediction horizon decreasing or/and the historical data's effeteness increasing [117]-[119].

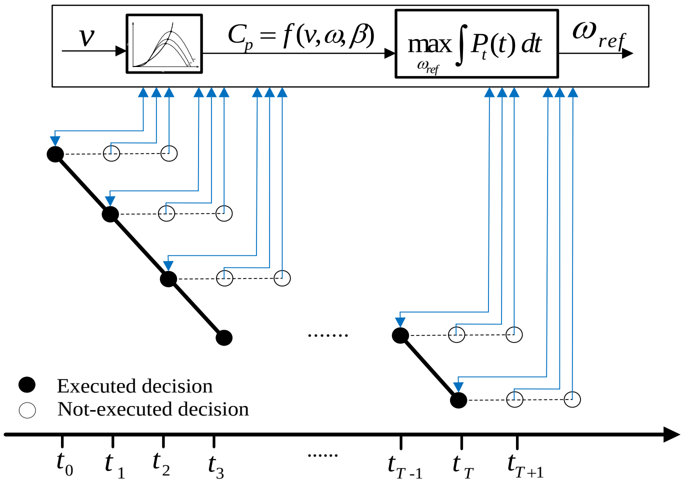

Fig. 3–3. Schematic diagram of IMPPT.

Thus, an Improved MPPT (IMPPT) algorithm is proposed in this work to take advantage of the increasing prediction accuracy in the short term.

A schematic diagram of the IMPPT algorithm is shown in Fig. 3-3, where the turbine characteristic curve is represented as a nonlinear function of wind speed v, turbine angular speed ω, and blade pitch angle β, and the look-ahead time duration is assumed to be two time periods.

At each time period a wind speed and two predicted wind speeds are viewed as the input signal and the optimal control command is computed from the IMPPT algorithm. Here, each time period should be on the scale of tens of seconds to a few minutes and the predicted wind speed will be continuously updated through historical data.

Different from TSR control and WSE control, which simply calculates the tracking reference from (3.21), the proposed IMPPT algorithm considers the short-term wind speed prediction, maximum wind power capture, and wind turbines' dynamic response collectively, and executes the optimal reference command in an intelligent way. Then, IMPPT becomes an optimization problem and the optimal reference can be solved with the following expression.

$$\begin{aligned}\max_{\omega_{ref}} \int_{t_0}^{t_2} P_t \; dt &= \max_{\omega_{ref}} \int_{t_0}^{t_2} \frac{\rho\pi R^2}{2} C_p\left(\lambda,\beta\right) v^3 \; dt \\ &= \max_{\omega_{ref}} \int_{t_0}^{t_2} \frac{\rho\pi R^2}{2} f\left(v,\omega,\beta\right) v^3 \; dt\end{aligned} \tag{3.22}$$

subject to

$$\omega(t) = \omega_0 + \frac{1}{J} \cdot \frac{\rho \pi R^2}{2} \int_{t_0}^{t_2} \left[\frac{C_p(\lambda, \beta) v^3}{\omega} - \frac{C_p(\lambda, \beta) v^3}{\omega_{ref}} \right] dt \tag{3.23}$$

$$\omega_{ref}(t) = \begin{cases} \omega_{ref1}, & t_0 \le t < t_1 \\ \omega_{ref2}, & t_1 \le t < t_2 \end{cases} \tag{3.24}$$

$$0 \le \omega(t) \le \omega_{\max}, \; t_0 \le t \le t_2 \tag{3.25}$$

Note that v_1 and v_2 are the predicted wind speeds at t_1 and t_2 and the pitch angle β is controlled to be zero in the partial load region. Thus, (3.22)-(3.25) can be rewritten as

$$\begin{aligned} &\max_{\omega_{ref}} \left[\int_{t_0}^{t_1} \frac{\rho \pi R^2 v_1^3}{2} C_p(\lambda, \beta)\, dt + \int_{t_1}^{t_2} \frac{\rho \pi R^2 v_2^3}{2} C_p(\lambda, \beta)\, dt \right] \\ = &\max_{\omega_{ref}} \left[\int_{0}^{t_1} \frac{\rho \pi R^2 v_1^3}{2} f(\omega)\, dt + \int_{t_1}^{t_2} \frac{\rho \pi R^2 v_2^3}{2} f(\omega)\, dt \right] \end{aligned} \tag{3.26}$$

subject to (3.24), (3.25), and

$$\omega(t) = \omega_0 + \frac{1}{J} \cdot \frac{\rho \pi R^2}{2} \int_{t_0}^{t_2} \left[\frac{f(\omega) v^3}{\omega} - \frac{f(\omega) v^3}{\omega_{ref}} \right] dt \tag{3.27}$$

Additionally, the performance of MPPT in this work is evaluated with the characteristic of fractional average power η. It is defined as the ratio of the mean captured power to the mean wind power and expressed as

$$\eta = \frac{1}{n} \sum_{k=1}^{N} P_t(i) \Big/ \frac{1}{n} \sum_{k=1}^{N} P_{wind}(i) = \sum_{k=1}^{N} C_p(i) \tag{3.28}$$

To further explain the proposed method, a simple simulation of TSR control and IMPPT control for a 1.5 MW turbine is shown in Fig. 3-4. When the wind speed constantly varies between 4 m/s and 7 m/s, the rotor speed ω_1 in TSR control tracks the reference ω_{ref1} to capture the maximum wind power for each wind speed. Due to the inertia effect on wind turbines' dynamic performances, there is a decrease in coefficient C_p and corresponding power losses in the tacking process. In contrast, the rotor speed ω_2 in IMPPT control tracks a different reference ω_{ref2} computed from

(17)-(20). ω_{ref2} is greater than ω_{ref1} at low wind speeds and becomes the same as ω_{ref1} when the wind speed is higher. Thus, the acceleration distance at the higher wind speed is shortened and the corresponding system efficiency is improved. In other words, even though the IMPPT efficiency is reduced at during low wind speed period, the WECS harvests much more energy when the wind speed is high. This is because the produced wind power is cubic to wind speed.

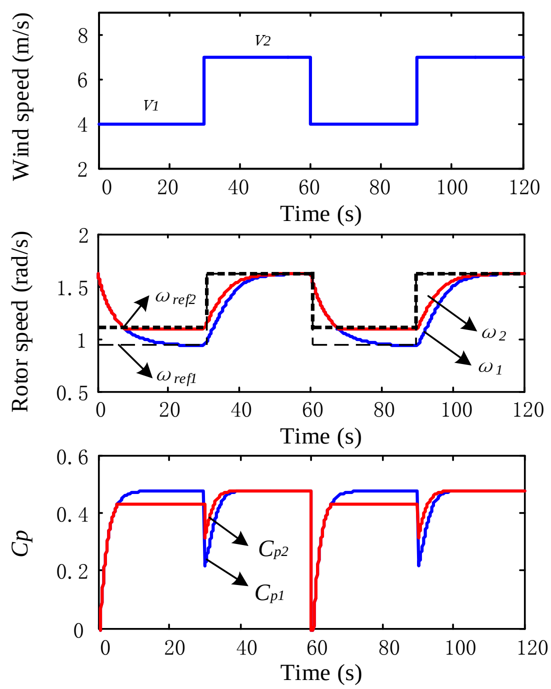

Fig. 3–4. Simulation results of MPPT and IMPPT.

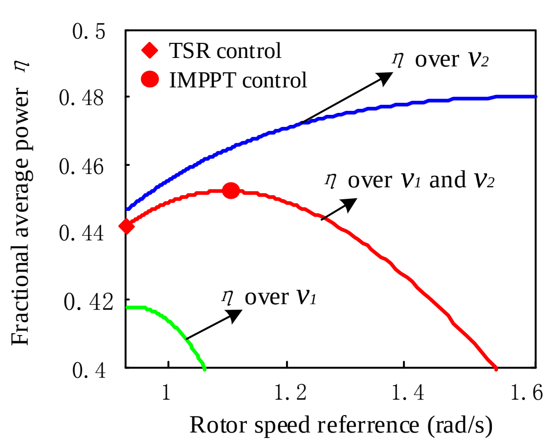

Fig. 3–5. MPPT efficiency with different rotor speed commands.

The simulation results in Fig. 3-5 clearly shows that the optimization of the reference ω_{ref} can achieve a higher overall power output. The fractional average power in IMPPT increases by 2.29% in one perdition horizon, which is a significant improvement in wind power industry.

3.3 WECS Control

The previous sections discussed the WECS model and the IMPPT algorithm, respectively. In this section, the WECS control problem is studied systematically, and multiple issues, such as wind speed uncertainties and wind turbines' mechanical damages, are considered.

Since this work focuses on the WECS operating in both the partial and the full load regions, the control system has multiple objectives. A schematic diagram of a classical control system in the WECS is depicted in Fig. 3-6.

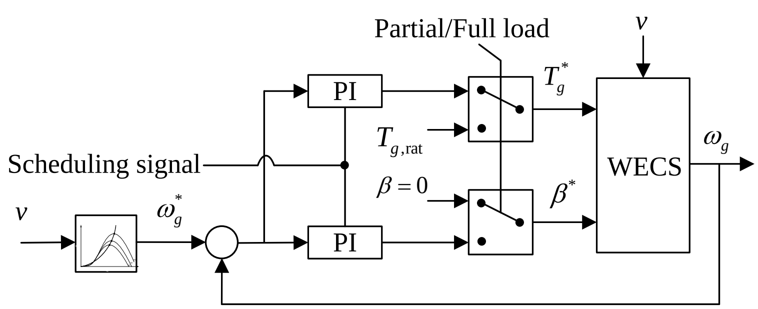

Fig. 3–6. Block diagram of classic WECS control.

In the partial load region, the controller is mainly expected to implement the MPPT, which is developed in Section 3.2. In the full load region, the controller is required to maintain both the generator power and the generator speed at their rated values $P_{g,rat}$ and $\omega_{g,rat}$. These objectives can be achieved by regulating the desired pitch angle β^* and/or the generator torque set point T_g^*.

Moreover, mitigating drive train transient loads and reducing control actuator activities, which have the effect of reducing the cost of wind turbines operation and maintenance as well as increasing the life time of the system's mechanical components, should also be considered in the control design. Thus, the cost function can be written as follows

$$\min\ f_N\left(\boldsymbol{x},\boldsymbol{y},\boldsymbol{u},\boldsymbol{d}\right)=\min\sum_{k=1}^{N}\left[q_1\left(d\omega^*-d\omega\right)_k^2+q_2\left(dP_g^*-dP_g\right)_k^2\right]$$
$$+\sum_{k=0}^{N-1}\left[r_1\left(dT_g^*\right)_k^2+r_2\left(d\beta^*\right)_k^2+r_3\left(\Delta T_g^*\right)_k^2+r_4\left(\Delta\beta^*\right)_k^2\right] \tag{3.29}$$

subject to

$$\boldsymbol{x}\left(k+1\right)=\boldsymbol{A_d}\boldsymbol{x}\left(k\right)+\boldsymbol{B_u}\boldsymbol{u}\left(k\right)+\boldsymbol{B_d}\boldsymbol{d}\left(k\right) \tag{3.30}$$

$$\boldsymbol{y}\left(k\right)=\boldsymbol{C_d}\boldsymbol{x}\left(k\right) \tag{3.31}$$

$$\omega_{g,\min}\le\omega_g\left(k\right)\le\omega_{g,\max}\text{, } k=1,2,\ldots,N \tag{3.32}$$

$$P_{g,\min}\le P_g\left(k\right)\le P_{g,\max}\text{, } k=1,2,\ldots,N \tag{3.33}$$

$$0\le T_g^*(k)\le T_{g,\max}\text{, } k=1,2,\ldots,N\text{-}1 \tag{3.34}$$

$$\beta_{\min}\le\beta^*\left(k\right)\le\beta_{\max}\text{, } k=1,2,\ldots,N\text{-}1 \tag{3.35}$$

$$\Delta\beta_{\min}\le\Delta\beta_d\left(k\right)\le\Delta\beta_{\max}\text{, } k=1,2,\ldots,N\text{-}1 \tag{3.36}$$

$$\boldsymbol{d}_{\min}\le\boldsymbol{d}\left(k\right)\le\boldsymbol{d}_{\max}\text{, } k=1,2,\ldots,N \tag{3.37}$$

where N is the control horizon, Δ means the change of control vector as $\Delta\boldsymbol{u}(k+1)=\boldsymbol{u}(k+1)-\boldsymbol{u}(k)$, and q_1, q_2, r_1, r_2, r_3 and r_4 are weighting coefficients.

For $dP_g=P_g-P_{g_{|op}}\approx d\omega_g T_{g_{|op}}+dT_g\omega_{g_{|op}}$ and $d\omega_g=\omega_g-\omega_{g_{|op}}$, (3.29) can be rewritten as

$$\begin{aligned}V_N\left(\boldsymbol{x}_0,\boldsymbol{u},\boldsymbol{d}\right)&=\sum_{k=1}^{N}\boldsymbol{x}(k)^T\boldsymbol{Q}\ \boldsymbol{x}(k)+\sum_{k=0}^{N-1}\left[\left(\boldsymbol{u}(k)-\boldsymbol{u}(k-1)\right)^T\boldsymbol{R}_1\left(\boldsymbol{u}(k)-\boldsymbol{u}(k-1)\right)+\boldsymbol{u}(k)^T\boldsymbol{R}_2\ \boldsymbol{u}(k)\right]\\&=\sum_{k=1}^{N}\boldsymbol{x}(k)^T\boldsymbol{Q}\ \boldsymbol{x}(k)+\sum_{k=0}^{N-1}\left[\left(\boldsymbol{u}(k)-\boldsymbol{u}(k-1)\right)^T\quad\boldsymbol{u}(k)^T\right]\boldsymbol{R}\left[\left(\boldsymbol{u}(k)-\boldsymbol{u}(k-1)\right)\quad\boldsymbol{u}(k)\right]^T\end{aligned} \tag{3.38}$$

with

$$\boldsymbol{Q}=\begin{bmatrix}0&0&0&0&0\\0&\frac{(q_1+q_2)T_g^{*2}}{\omega_{\mathrm{B}}^2}&0&\frac{q_2\omega^*T_g^*}{\omega_{\mathrm{B}}T_{g,\mathrm{B}}}&0\\0&0&0&0&0\\0&\frac{q_2\omega^*T_g^*}{\omega_{\mathrm{B}}T_{g,\mathrm{B}}}&0&\frac{q_2\omega^{*2}}{T_{g,\mathrm{B}}^2}&0\\0&0&0&0&0\end{bmatrix},\ \boldsymbol{R}_1=\begin{bmatrix}r_1/T_{g,B}^2&0\\0&r_2/\beta_B^2\end{bmatrix},\boldsymbol{R}_2=\begin{bmatrix}r_3/T_{g,B}^2&0\\0&r_4/\beta_B^2\end{bmatrix}\text{ and }\boldsymbol{R}=\begin{bmatrix}\boldsymbol{R}_1&0\\0&\boldsymbol{R}_2\end{bmatrix}.$$

where x_0 is the initial condition at each time step, $\bullet_{\mathrm{B}}$ is the base value of $\bullet$, $\boldsymbol{Q} \succeq 0$ (i.e., semi-definite positive matrix), and $\boldsymbol{R}_1, \boldsymbol{R}_2 \succ 0$ (i.e., positive definite matrix).

Then, with the consideration of the wind speed error *d* as a box uncertain set, (3.38) can be written as a min-max problem to compute the optimal control that minimizes the largest cost in the disturbance space.

Problem: $\boldsymbol{u}(\boldsymbol{x}_0) := \arg\min_{\boldsymbol{u}} \max_{d \in \mathbb{D}_\gamma} V_N$ (3.39)

subject to (3.30), (3.31), (3.35), (3.36), (3.37) and

$$\mathbb{P}\left(\omega_{\min} \le \omega(k) \le \omega_{\max}\right) \ge \alpha_1 \tag{3.40}$$

$$\mathbb{P}\left(P_{g,\min} \le P_g(k) \le P_{g,\max}\right) \ge \alpha_2 \tag{3.41}$$

$$\mathbb{P}\left(0 \le T_g^*(k) \le T_{g,\max}\right) \ge \alpha_3 \tag{3.42}$$

Note that the non-convex chance constraints (3.40)–(3.42) are the probabilistic forms of constraints in (3.32)–(3.34), respectively. Constraints (3.40)–(3.42) can be represented in the form of inequalities, and Problem (3.39) can be developed into a convex optimization problem and can be solved by SDP.

In many previously used WECS controls, the wind speed disturbance is commonly assumed to be Gaussian [78], [79]. This assumption may not hold in many cases and in the real world the disturbance does not always follow a regular probability distribution.

However, it is not difficult to make a reasonable assumption on the bound of the disturbance (i.e., wind speeds or wind speed variations usually go inbounded). This work considers the unknown wind speed error as Norm-Bounded and employs the SDP method to search for an optimal solution. It can be viewed as finding the optimal control that minimizes the worst cost within the disturbance bound. Thus, the advantage of the proposed method is that it is not necessary to know the statistics of the disturbance distribution which is used to compute the expected cost in the MPC based method [80]. Further, through IMPPT and SDP it can be guaranteed that the overall cost will be limited in an appropriate range.

3.4 Case Study

The performance of the proposed MPPT control and WECS control strategies are demonstrated in this section. The simulation is implemented in MATLAB and carried on a computer with a 2.60 GHz core. The proposed problem is solved with the LMIs tool box, which is widely used in the control area. Before the test, several parameters require a reasonable selection, especially the wind speed fluctuation frequency and weighting coefficients in control objectives.

For the wind speed, as the input signal of the WECS control, its frequency largely impacts the performance of control actions. A low frequency could not properly simulate the dynamic characteristics of the real wind speed, and a high frequency may present difficulties in system inertia response. In practice, the cycle of the mean wind speed is normally set to 10 minutes while the frequency of the disturbance is commonly uncertain.

For the weights in the control objective functional, their tuning is also a challenging task, since different parameters give different outputs.

To be specific, the simulation result of the control strategy with different weight r_1 is shown in Fig. 3-7, where the WECS operates under the gradient wind speed. As shown in Fig. 3-7, the tuning of weights obviously contributes to the fast-response and high-stability of WECS control. Moreover, since the control objectives are related to the electrical generation and mechanical losses, the weights tuning requires not only technical skills but also wind power operators' experience and expectation. Parameters selection becomes a multilevel complex problem.

Nevertheless, since the motivation of this work is to apply advanced modeling and control methods to WECSs, simulation parameters are simply selected and listed in Table I. In general, these parameters are consistent with the parameters given in [41]-[43] and the simulation results are comparable with those in [78] and [79].

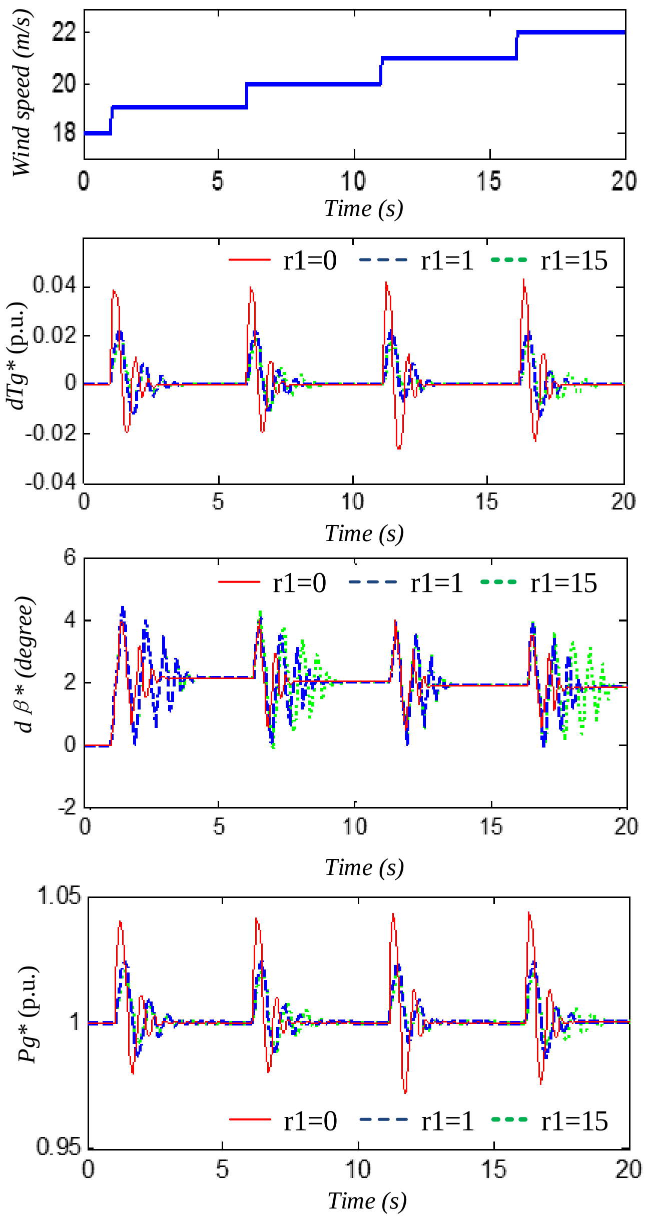

Fig. 3–7. Results of WECS control with different weights.

3.4.1 Case 1: MPPT Control

In Case 1, the proposed MPPT control is tested on a WECS. The motivation is to explore an efficient method for wind power utilization which is implemented in two aspects: maximizing the efficiency of MPPT and minimizing the operation and maintenance cost of WECSs. To simplify the problem formulation we first calculate the optimal references from the IMPPT algorithm and then solve the min-max problem though SDP. Also, parameters used in the simulation are listed in Table 3.2. The weights are set to q_1=1, q_2=0, r_1=0.15, r_2=0, r_3=1, and r_4=0.

Table 3-2 Simulation parameters.

Rated Power [MW]	0.75	1.5	2	3	5
Rotor radius [m]	25	35	40	45	58
Rated rotor speed [rpm]	28.6	20	18	16	14.8
Rated wind speed [m/s]	11	11	12	12	12
Cut-in wind speed [m/s]	4.5	4	4	4	3
Cut-out wind speed [m/s]	25	25	25	25	25
Moment of inertia [10^6 kg·m^2]	0.13	1.86	5.67	12.6	12.9
Optimum tip speed ratio	8.1				
Maximum power coefficient	0.48				
Air density [kg/m^3]	1.225				

With the application of state-of-the-art technologies to wind speed forecasting, the wind speed is assumed to be predicted every minute and the prediction error is ignored in the short-term. As the first step to test the proposed control strategy, the predicted wind speed is chosen in the midrange of the partial load region (6.5 m/s and 8 m/s). The disturbance is set with the bounds of $\pm$1 m/s, which is considered to be the maximum variance in the model of wind speed errors.

In Fig. 3-8, the performances of the TSR control and the proposed IMPPT control are compared. Under Norm-bounded disturbances, the optimal references derived from conventional MPPT and IMPPT are very close at most operating points, but when a gusty wind speed or a gradient wind occurs, IMPPT control can capture more wind power than TSR control.

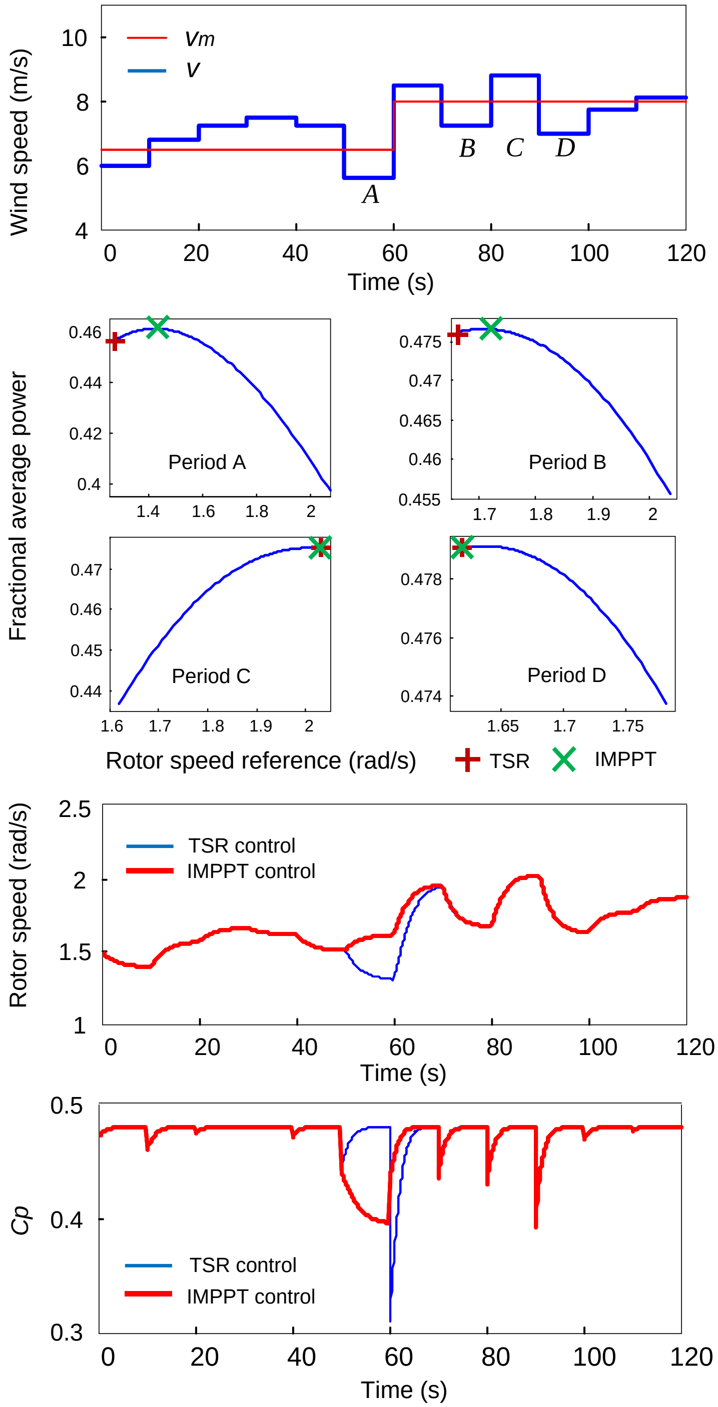

Fig. 3–8. Results of MPPT and IMPPT.

Table 3-3 IMPPT efficiency under different wind speed variations.

η_2/η_1	**4 m/s**	**5 m/s**	**6 m/s**	**7 m/s**	**8 m/s**	**9 m/s**	**10 m/s**	**11 m/s**
4 m/s	1.0	1.00.3	1.010	1.023	1.043	1.070	1.011	1.156
5m/s	1.001	1.0	1.001	1.004	1.010	1.018	1.029	1.044
6m/s	1.000	1.000	1.0	1.000	1.002	1.004	1.008	1.013
7m/s	1.001	1.001	1.000	1.0	1.000	1.0051	1.002	1.004
8m/s	1.001	1.001	1.000	1.0	1.0	1.000	1.0001	1.001
9m/s	1.001	1.001	1.000	1.000	1.000	1.0	1.000	1.001
10m/s	1.001	1.001	1.000	1.000	1.000	1.000	1.0	1.000
11m/s	1.000	1.000	1.000	1.000	1.000	1.000	1.000	1.0

Table 3-4 IMPPT efficiency of different wind turbines.

Wind turbine [MW]	0.75	1.5	2	3	5
Rate η_2/η_1	1.021	1.023	1.019	1.023	1.020

In addition, different wind speed variation ranges on a 1.5 MW wind turbine are studied and the corresponding η_2/η_1 values are calculated. We also fix the tracking bandwidth of MPPT and implement similar simulations on different wind turbines with the parameters in Table 3.2. The results are listed in Table 3-3 and Table 3-4, respectively.

Also, it should be noted that several efficient techniques are proposed in the recent literature to improve the efficiency of MPPT during the dynamic process [41]-[43]. Compared with these prior methods, IMPPT presents three advantages: 1) the tracking distance is shortened and the control system's dynamic characteristic is improved; 2) the acceleration time of mechanical components is reduced and the corresponding mechanical damage is alleviated; and 3) no extra power electronic device is required, and system complexity and operation cost is only slightly increased.

Moreover, as opposed to the approaches to reduce the effect of inertia in the literature [41], the proposed IMPPT algorithm optimizes the rotor reference and shortens the tracking path to improve MPPT efficiency. This means that all the proposed techniques in the literature can be combined with the IMMPT algorithm since they solve the same problem in different angles. Thus, IMPPT is promising in practice.

3.4.1 Case 2: WECS Control

After the calculation of optimal references, WECS control can be implemented as discussed before. An actual hourly wind speed measured at a 70 meter tower is selected as the mean wind speed for simulation. Then, a perturbation is added to the mean wind speed to mimic the randomness within the norm bound.

From the simulation result in Fig. 3-9, the real-time wind speed fluctuates around the mean wind speed with a bound of 1 m/s. This guarantees that the WECS operates within the physical constraints of the control variables, e.g. limits on the rotor speed ω. Two observations can be obtained with a comparison of the reference rotor speed and the actual rotor speed. First, when the wind speed is high, the wind turbine closely tracks the reference value and captures the high wind power output efficiently. Second, when the wind speed falls into a low range, MPPT efficiency is reduced to mitigate the drive train torsional torque fluctuation. Since the mechanical fatigue of the wind turbine is difficult to quantify and compare with the energy produced, tuning of the weighting coefficients may be based on the wind power operators' experience and perspective.

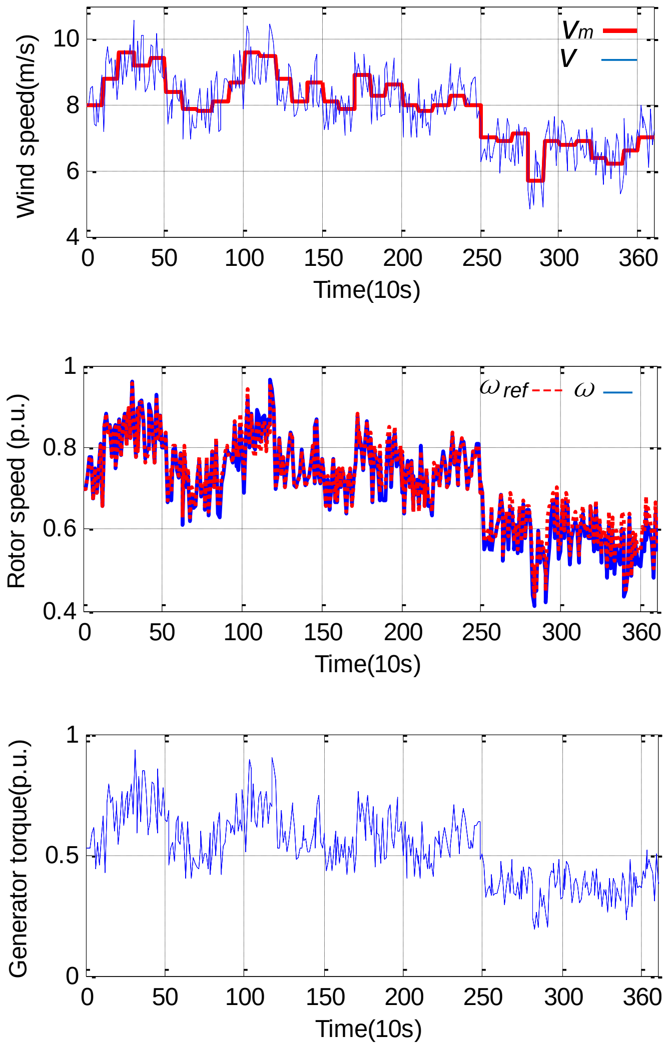

Fig. 3–9. Results of WECS control.

3.5 Conclusion

The contribution of this chapter can be summarized below:

In this chapter, a novel MPPT strategy is proposed for the variable-speed variable-pitch WECS operating in the partial load region. The control strategy aims to achieve a balance between power output maximization and operating costs minimization. It can improve the efficiency of MPPT and increase the life time of mechanical components.

In the proposed approach, the wind speed error is modeled as Norm-Bounded without a known distribution. This likely represents a more realistic model in practice and avoids the assumption of the noise distribution. Moreover, the problem is formulated into a semi-definite programming mode which has not been previously implemented in MPPT control.

Furthermore, dynamic performances of large-scale wind generation systems are considered and an IMPPT algorithm is proposed to increase the system efficiency. As opposed to simply reducing the effect of inertia, the rotor speed reference is regulated in an intelligent way such that the movement of the rotor during the dynamic tracking process is shortened and the mechanical fatigue is reduced. Also, the system’s overall efficiency can be improved, especially when the wind speed experiences a drastic change.

4 Uncertain Communication Delay in WAMSs

In this chapter, the uncertain communication delay in WAMSs is investigated, with special focus on the one in time-critical wide-area applications. First, the real-world communication delay is measured and analyzed. Then, the bounded modeling method is presented for wide-area applications and further applied for system-area and substation-area protection applications, respectively. The proposed bounded modeling method is expected to be an important tool in the planning, design, and operation of time-critical wide-area applications.

4.1 Statistics of Communication Delay

To better understand the uncertain data latency in WAMSs, this work takes advantage of the low-cost and quickly-deployable FNET/GridEye, and measures the communication delay of the FNET/GridEye in one week as shown in Figs. 4-1 and 4-2.

It is observed that the communication delay may vary dramatically in short terms (e.g., one minute), and its probability distribution changes with time periods and locations. Further, a system-wide disturbance may lead to heavy traffic of communication networks, since a number of commands and alarm signals emerge instantaneously. FNET/GridEye as a WAMS example, implies some nature of wide-area communications. The dynamic characteristic of communication delays needs to be taken into account.

4.2 Modeling of Communication Delay

4.2.1 Conventional Modeling Method

IEEE Std C37.118 clarifies that the latency of synchrophasor data is composed of a communication delay t_d and terminal processing delays t_{PMU} and t_{APP}, and provides their typical ranges as shown in Table 4-1. Some literatures further divide the latency into seven terms as follows [44], [101]

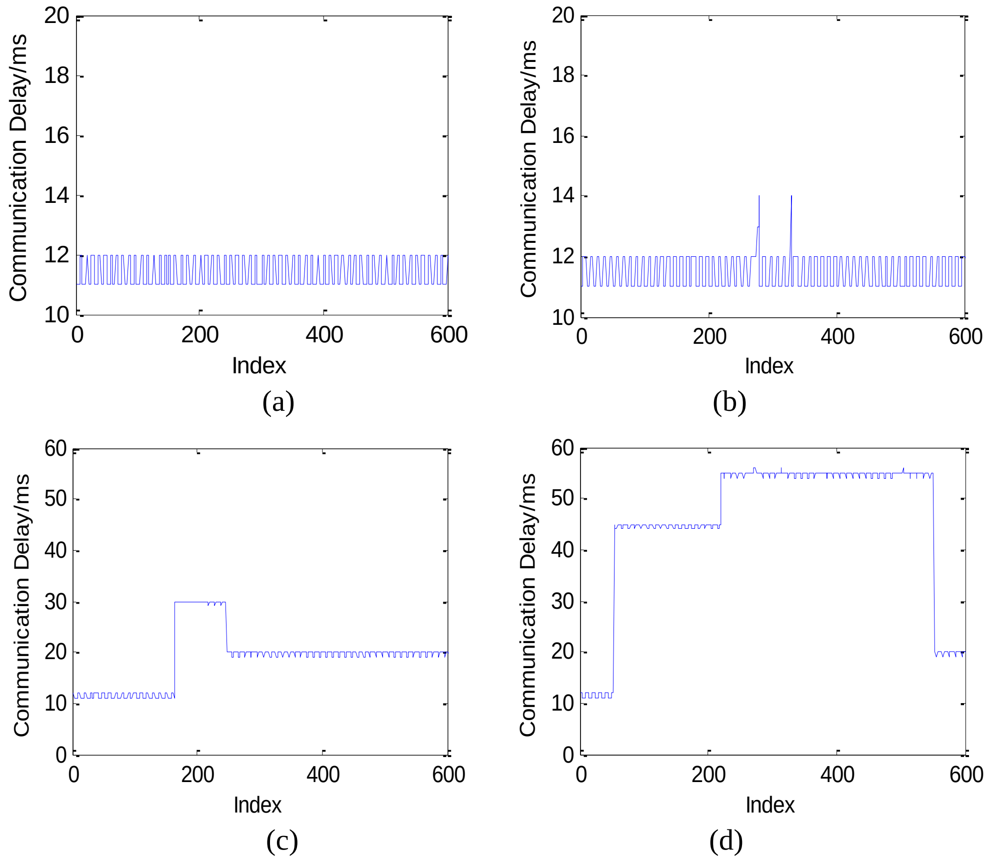

Fig. 4–1. Communication delay measurements in short-term (one minute).

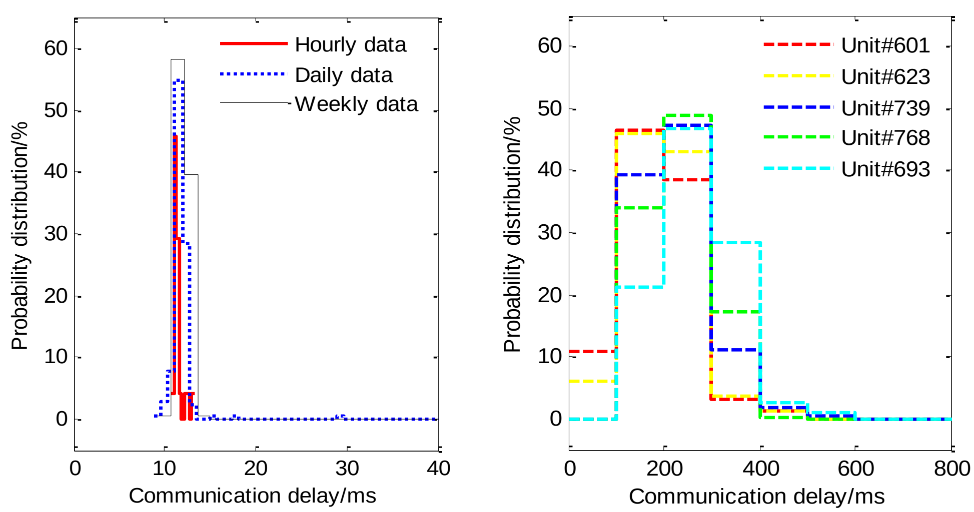

(a) Statistical results of different time spans; (b) Statistical results of different locations.

Fig. 4–2. Communication delay measurements in long-term (a few hours to a few days).

$$
\begin{aligned}
t_{latency} &= t_{PMU} + t_d + t_{APP} \\
&= t_{PMU} + t_{PDC} + t_{que} + t_{trans} + t_{prop} + t_{CC} + t_{APP}
\end{aligned}
\tag{4.1}
$$

where t_{PDC} and t_{CC} denote the processing delays of a PDC and a control center, respectively; transmission delay $t_{trans}=L/B$ is calculated by the packet length L (bit) and the link bandwidth B (bit/s), propagation delay $t_{prop}=D/v$ is calculated by the distance D between nodes and the light speed v in the particular communication medium ($v \doteq 2.0\times10^5\ km/s$ in optical fibers), and queuing delay t_{que} is determined by the traffic behavior of communication networks.

As discussed in Section 2.2, the previous works mainly study the communication delay via theoretical analysis and simulation results, and model the communication delay as constant or stochastic. The theoretical or simulation results may be partially true or idealistic when they are compared with the actual values under various conditions.

4.2.2 Bounded Modeling Method for System-Area Applications

This work proposes a bounded model for the dynamic communication delay. The main idea is to utilize the existing WAMS and guarantee the performance of regional and backbone networks, respectively.

First, PDCs are utilized to limit the communication delay of complex regional networks. The communication delay between PMUs and PDCs primarily stems from the propagation time of synchrophasor data and the processing time of PDCs. Accordingly, the amount of $t_{RN}+t_{PDC}$ depends on the physical distance between PMUs/PDCs and PDCs (the communication path of a regional network is PMU, PDC_1, …, PDC_{NPDC}), and the data arriving and sending-out time in PDCs.

IEEE Std C37.244 defines seventeen PDC functions as shown in Fig. 4-3. In reality, multiple PMU packages with the same time-tag may not arrive at a PDC simultaneously. The PDC assigns the early arriving data to a buffer (data buffering) and aligns the available data after the preset waiting time (data aggregation). The waiting time ensures PDCs sort and forward PMU packages within an acceptable time period instead of waiting for the delayed or lost packages blindly.

Meanwhile, the PDC can calculate the delay between a PMU and a PDC or between a PDC and another PDC using time-tags (data latency calculation).

Hence, this work combines data aggregation, data latency calculation and data buffering functions as shown in Fig. 4-3, and views the complex regional network as a black box. Then, in PDCs, the communication delay can be calculated with time-tags and further bounded through the waiting time as follows

$$\begin{aligned} t_{RN} + t_{PDC} &= [\sum_{k=1}^{N_{PDC}} (t_{cal\_k} + t_{proc\_k}), \sum_{k=1}^{N_{PDC}} (t_{cal\_k} + t_{wait\_k} + t_{proc\_k})] \\ &\doteq [\sum_{k=1}^{N_{PDC}} t_{cal\_k}, \quad D_{RN}/v + \sum_{k=1}^{N_{PDC}} t_{wait\_k}] \end{aligned} \tag{4.2}$$

where N_{PDC} is the number of PDCs, t_{cal_k} is the calculated delay between PMU and PDC_1 or between PDC_{k-1} and PDC_k, t_{wait_k} is the waiting time of PDC_k, and t_{proc_k} is the additional processing time of PDC_k. D_{RN} is the physical distance of the communication path in reginal networks. Normally, t_{proc_k} is much smaller than other terms in (4.2) and is ignored here. The lower delay bound in (4.2) means that the PMU packages experience no waiting time at each PDC (arriving at each PDC simultaneously), and the upper delay bound means that the PMU packages experience the whole preset waiting time at every PDC.

Second, the communication delay over backbone networks is bounded owing to SONET/SDH implementation. Currently, SONET/SDH in Fig. 4-4 is globally deployed. In the U.S., thousands of miles of optical fibers have been installed as parts of power line facilities and SONET-based backbone networks have been employed by many utilities [44]. In China, a large number of power industry backbone networks select optical fibers and SDH as the communication medium and protocol [121], [122]. SONET/SDH not only greatly improves the performance of power system communications, but also provides fast, reliable, and robust communication infrastructure for wide-area protection. Here, the self-healing potential of SONET is utilized to guarantee the QoS of backbone networks, and further determine the bound of communication delays.

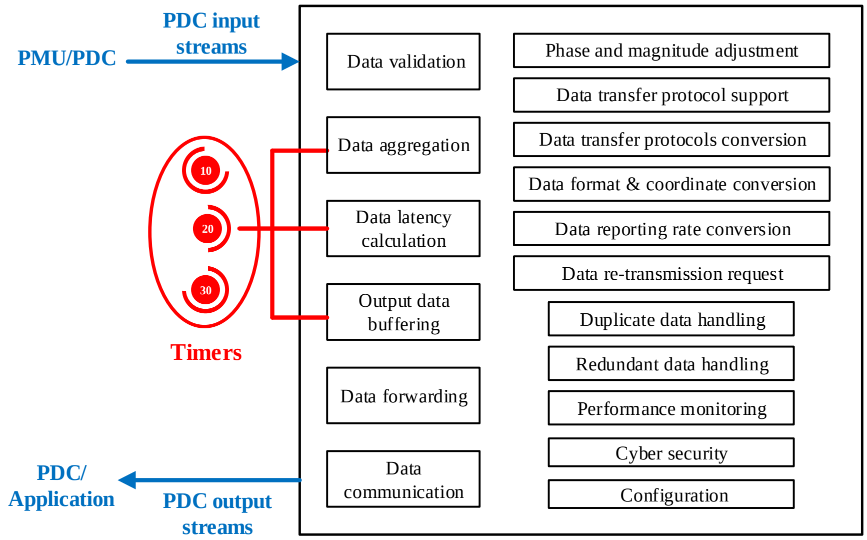

Fig. 4–3. Block diagram of PDC functions.

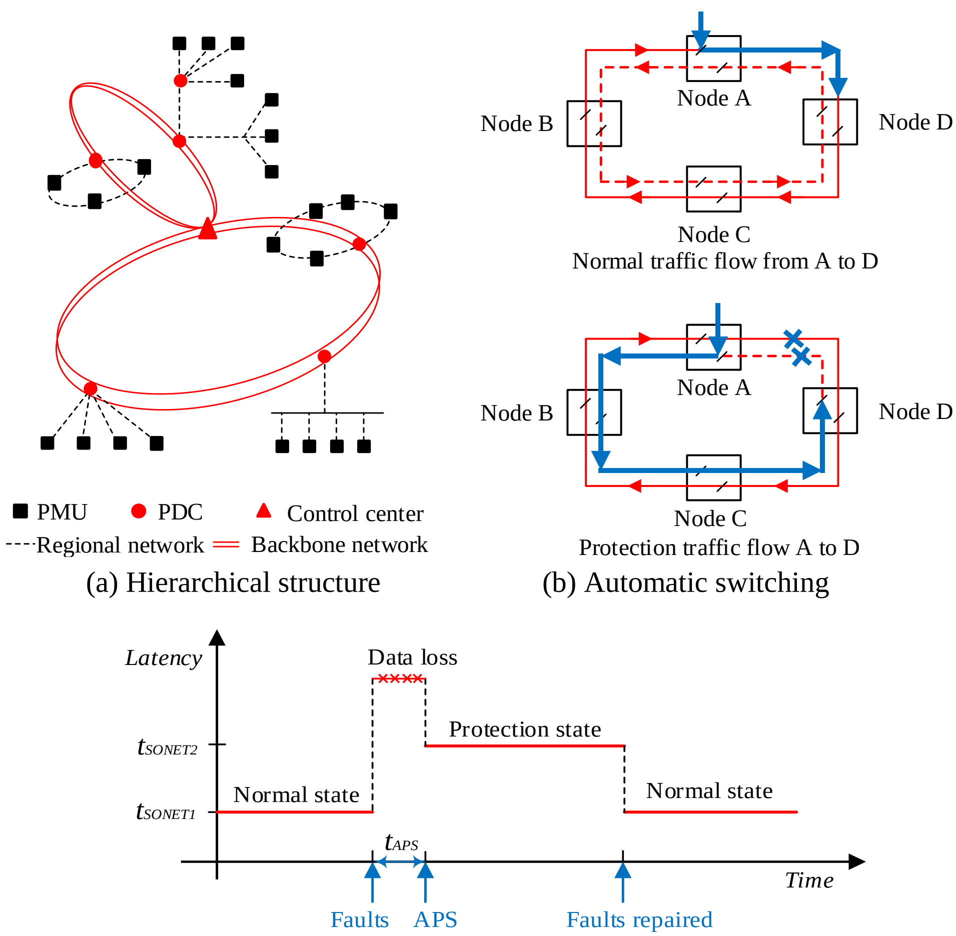

Fig. 4–4. Operating principle of SONT.

Typically, SONET works at the unidirectional path-switched ring (UPSR) or bidirectional line-switched ring (BLSR) mode. SONET realizes the self-healing and redundant communication using its ring topology and automatic protection switching (APS) scheme. In the normal state, the information is transmitted on the primary ring and a copy of the information travels via the protection ring; while in the case of a node or link failure, SONET automatically and quickly switches the information flow from the primary ring to the protection ring, and sends out alarm signals. Also, SONET will resume the information flow to the original route when the equipment or fibers are repaired.

In terms of multiple failures, four-fiber BLSR design can be used to increase SONET's fault tolerance capacities. Hence, SONET can improve the reliability of communication networks and guarantee the QoS of information transmission. The communication delay of SONET based backbone networks becomes predictable as shown in Fig. 4-4 and its bound can be calculated b

$$t_{BN} = [t_{SONET_1}, t_{SONET_2}] + D_{BN} / v \tag{4.3}$$

where t_{SONET1} and t_{SONET2} are the SONET communication delay in the normal state and the protection state, respectively. D_{BN} is the physical distance of the communication path in the backbone network.

Consequently, assuming the communication path of wide-are protection follows the order of *PMU, Regional PDC, Central PDC, SONET, and Application*, the upper bound of the communication delay can be determined as follows

$$t_d \leq D_{RN} / v + (t_{wait\_1} + t_{waitt\_2}) + D_{BN} / v + t_{SONET_2} \tag{4.4}$$

4.2.3 Bounded Modeling Method for Substation-Area Applications

To quantify the communication delay in a substation area network (i.e. switched Ethernet network), two general approaches are used in the literature: stochastic approaches and deterministic approaches [123]-[125].

The former studies the average behavior of a stochastic network and works out the mean statistical or probabilistic delay. For instance, the queuing theory assumes the distribution of delays as Poisson or Bernoulli, and computes the mean value of delays and possibly the quantity of distributions. Regardless, time delays may not always follow a regular distribution in reality and the upper bound of delays may not exist or be computable. In contrast, the latter focuses on the worst-case performance analysis and determines the upper bound of delays, which is mainly implemented using network calculus.

In substation-area protection, a protective relay is expected to effectively detect the fault and trip off the corresponding circuit breaker after a preprogrammed time delay. Meanwhile, SV and GOOSE packages should be transferred to IEDs within the predetermined time; otherwise, they are viewed as corrupted and lost, which may disable the protection functionality and endanger the substation and even the whole power grid. In practice, the time delay of protective relays needs reasonable setting. If the time delay is larger than the transfer time limit (e.g., 3 ms), the protection may be invalid; whereas if the time delay is set to be idealistic, the package losses may frequently occur. The network calculus theory focuses on performance guarantees, instead of the classical queuing theory dealing with average values. Therefore, network calculus is used to model the communication delay here.

Network calculus, as a queueing theory for performance guarantee analysis of computer networks, was first introduced by Cruz for modeling network entities and flows [126]. In the past two decades, it has been generalized by making use of alternate algebras such as min-plus and max-plus algebra to transform complex network systems into analytically tractable systems [126]-[128].

To be specific, it introduces the concepts of arrival and service curves to model the traffic arrival process and the service process of a system, based on which network performance bounds are further analyzed.

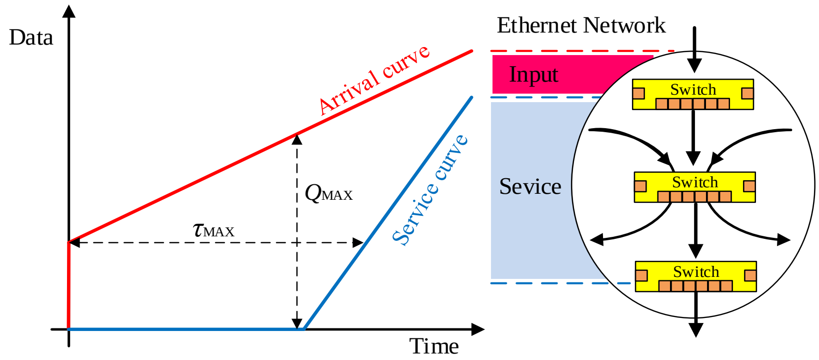

Fig. 4–5. Typical arrival and service curves.

As shown in Fig. 4-5, an arrival curve $\alpha(t)$ in (4.5) upper-bounds the amount of traffic input of a data flow to a network system, a service curve $\beta(t)$ in (4.6) lower-bounds the amount of service provided by the system to the data flow, and these two curves collaboratively determine the delay bound τ_{max} in (4.7) and backlog bound Q_{max} in (4.8).

$$\alpha(t) = rt + b \tag{4.5}$$

$$\beta(t) = R\,[t-\theta]^{+} \tag{4.6}$$

$$\tau(t) \le \sup_{t\ge 0}\left\{\inf\ \left\{\tau_{\max} : \alpha(t) \le \beta(t+\tau_{\max})\right\}\right\} \tag{4.7}$$

$$Q(t) \le Q_{\max} = \sup_{t\ge 0}\left\{\alpha(t) - \beta(t)\right\} \tag{4.8}$$

where (4.5) and (4.6) constraint the arrival and service processes of a data flow, which have average traffic rate r with maximum instantaneous burst b and minimum service rate R with latency parameter θ, respectively. With the assumption of $r \le R$, it can be easily obtained that $\tau_{max} = b/R + \theta$ and $Q_{max}=b+ r\,\theta$. The delay bound τ_{max} and backlog bound Q_{max} are given by the maximum horizontal and vertical distances between $\alpha(t)$ and $\beta(t)$, respectively.

Recently, the network calculus theory has been applied to calculate the delay bound of intra-substation communications in [129]. In addition, the idea of worst-case analysis as in network calculus was adopted in [130]. In the present work, network calculus is employed for delay bound analysis of substation-area communications where priority queuing is used to schedule different types of messages in the network. For this analysis, a summary of the related network calculus results is presented as follows.

For ease of expression, only one flow is used in the following to represent the traffic on the same end-to-end path. Denote the arrival and service curves for the data flow on path *p* with priority level *i* at server *j* as $\alpha_{j,p}^{i}$ and $\beta_{j,p}^{i}$. Accordingly, denote the arrival and service curves for the aggregate data flow on all paths with priority level *i* at server *j* as α_j^i and β_j^i. Let P_j represent the set of paths through server *j*. As to be discussed, in the network, all arrival curves and service curves can be represented using the types of (4.5) and (4.6).

Specifically, the following results are readily obtained from the network calculus theory [44].

(P1) Superposition property

$$\alpha_j^i(t) = r_j^i t + b_j^i$$

with $r_j^i = \sum_{p \in P_j} r_{j,p}^i$ and $b_j^i = \sum_{p \in P_j} b_{j,p}^i$

(P2) "Leftover" service property under priority scheduling

$$\beta_j^i(\mathrm{t}) = R_j^i[\mathrm{t} - \theta_j^i]^+$$

with

$$R_j^i = C - r_j^1 - \cdots r_j^{i-1}$$

$$\theta_j^i = \theta_j \;\; + (b_j^1 + \cdots + b_j^{i-1})/R_j^i$$

(P2') Leftover service property under FIFO scheduling

$$\beta_{j,p}^i(\mathrm{t}) = R_{j,p}^i[\mathrm{t} - \theta_{j,p}^i]^+$$

with

$$R_{j,p}^i = R_j^i - r_j^i + r_{j,p}^i$$

$$\theta_{j,p}^{i} = \theta_{j}^{i} + (b_{j}^{i} - b_{j,p}^{i})/R_{j,p}^{i}$$

(P3) Output property

$$\alpha_{j}^{*i}(t) = r_{j}^{i} t + (b_{j}^{i} + r_{j}^{i}\theta_{j}^{i})$$

$$\alpha_{j,p}^{*i}(t) = r_{j,p}^{i} t + (b_{j,p}^{i} + r_{j,p}^{i}\theta_{j,p}^{i})$$

(P4) Concatenation property

$$\beta_{p}^{i}(\mathrm{t}) = \beta_{1,p}^{i}(\mathrm{t}) \otimes \cdots \otimes \beta_{n,p}^{i}(\mathrm{t})$$

With these properties as well as the delay and backlog service guarantee analysis property (P5), delay bounds for a feedforward network can be derived under a rather general and intuitive stability condition $r_{j}^{i} \leq R_{j}^{i}$. In fact, under a stricter condition on the throughput, delay bound analysis can be extended to arbitrary network topology.

For the system considered in this work, the arrival and service curves of GOOSE and SV messages tagged with the highest and high priorities, at the first hop, can be written as (4.9) and (4.10) below.

$$\begin{cases} \alpha_{1,p}^{GS}(t) = r_{1,p}^{GS} t + b_{1,j}^{GS} = (L^{GS} \times f^{GS})t + L^{GS} \\ \alpha_{1,p}^{SV}(t) = r_{1,p}^{SV} t + b_{1,j}^{SV} = (L^{SV} \times f^{SV})t + L^{SV} \end{cases} \tag{4.9}$$

$$\begin{cases} \beta_{1}^{GS}(t) = R_{1}^{GS}[t - \theta_{1}^{GS}]^{+} = C[t - \frac{L^{GS}}{C}]^{+} \\ \beta_{1}^{SV}(t) = R_{1}^{SV}[t - \theta_{1}^{SV}]^{+} = (C - r_{1}^{GS})[t - \frac{L^{GS} + b_{1}^{GS}}{C - r_{1}^{GS}}]^{+} \end{cases} \tag{4.10}$$

where L^{GS} and L^{SV} are the maximum message lengths of GOOSE and SV messages, respectively; f^{Gs} and f^{SV} are the frequencies of generating GOOSE and SV messages, respectively; and C is the switch port rate.

In this work, L^{GS}, L^{SV}, f^{Gs}, f^{SV} and C are selected as 226 bytes, 230 bytes, 10 sps, 4000 sps, and 1000 Mbps, respectively. A detailed explanation on the delay bound calculation using network calculus is presented in the Appendix section.

4.3 Case Study

In engineering, each protection or control application has specific requirements on the communication delay. For instance, the delay is required below 10 ms for primary protection, and from tens of milliseconds to a few seconds for backup protection in [44].

To further discuss the proposed bounded model for the protection and control applications, the test studies of wide-area protection, substation-area protection and wide-area dimpling control are performed in this section.

4.3.1 Case 1: System-Area Protection

In this case, the bounded modeling method for system-area protection is employed in the IEEE 14 bus system as shown in Fig. 4-6, which is dived into three areas according their geographical locations and voltage levels.

The parameters of the IEEE 14 bus system can be found in [44], the PMU package length is 2000 bit, the bandwidths of regional and backbone networks are 155 Mbps and 622 Mbps, respectively, and the preset waiting time of PDC1, PDC2, and PDC3 is 1.50 ms, 0.80 ms, and 1.00 ms, respectively.

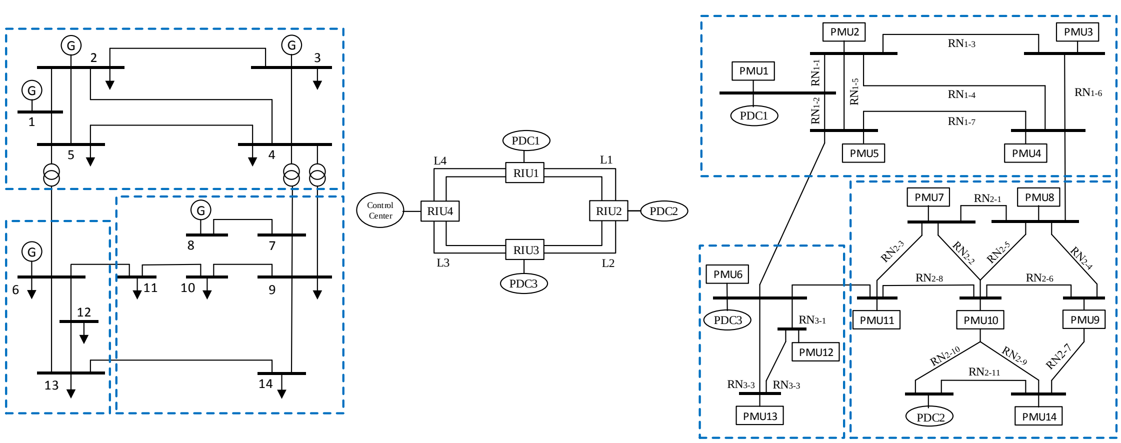

Fig. 4–6. IEEE 14 bus test system.

Table 4-1 Communication delays between PMUs and PDCs.

Conditions	Area	Max t_{prop} /ms	Min t_{prop}/ms	t_{RN}+ t_{PDC}/ms
Light traffic	Area 1	1.408	0.573	1.408
	Area 2	0.653	0.258	0.653
	Area 3	0.768	0.013	0.768
Heavy traffic	Area 1	1.408+	0.573	2.073
	Area 2	0.653+	0.258	1.058
	Area 3	0.768+	0.013	1.013

P.S. "+" denotes the additional propagation delay under heavy traffic.

Table 4-2 Communication delays between PMUs and applications.

Conditions	Area	t_{RN}+ t_{PDC}/ms	t_{BN}/ms	t_d/ms
Light traffic	Area 1	1.408	1.459	2.867
	Area 2	0.653	1.056	1.709
	Area 3	0.788	0.603	1.391
Heavy traffic	Area 1	2.073	1.459	3.532
	Area 2	1.058	1.056	2.114
	Area 3	1.013	0.603	1.616
Heavy traffic + L1 break	Area 1	2.073	2.860	4.933
	Area 2	1.058	1.053	2.111
	Area 3	1.013	1.506	2.519
Heavy traffic + L2 break	Area 1	2.073	1.956	4.029
	Area 2	1.058	2.460	3.518
	Area 3	1.013	0.602	1.615
Heavy traffic + L3 break	Area 1	2.073	0.753	2.826
	Area 2	1.058	1.154	2.212
	Area 3	1.013	1.610	2.623

Assume the regional network experiences the ideal and worst traffic, respectively, and the backbone network suffers the L1, L2, and L3 break, respectively. The corresponding results are listed in Tables 4-1 and 4-2.

It is observed that the communication delays under various traffics are bounded between 1.391 ms and 4.933 ms. The communication infrastructure in [44] provides a fast and reliable platform for wide-area protection.

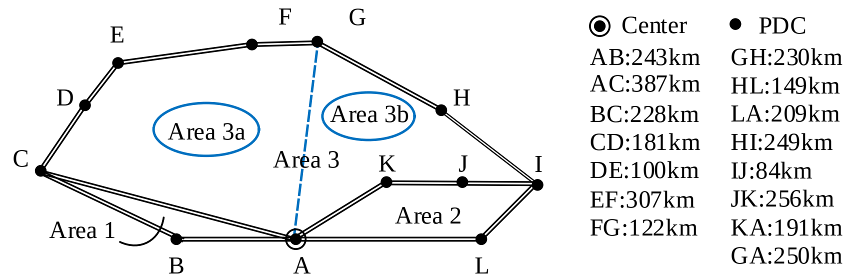

Fig. 4–7. SDH of China Southern Power Grid.

Table 4-3 Communication delays under different network scenarios.

Conditions	Area	t_d/ms	Maximum t_d location
Original network	Area 1	[3.360, 4.078]	AB break
	Area 2	[4.413, 6.828]	IJ break
	Area 3	[9.269, 15.284]	FG break
Improved network	Area 3a	[5.566, 9.828]	DE break
	Area 3b	[5.706, 8.191]	IJ Break

Further, the bounded model is deployed in a larger system as shown in Fig. 4-7. For the sake of simplification, the communication between PMUs and PDCs is t_{RN} is assumed as 1 ms globally (about the median value in Table 4-2). The communication delays of three areas are listed in Table 4-3. It can be easily observed that t_d over wide backbone networks (Area 3) may be greater than expected (10 ms). To ensure the normal operation of protective devices, there are two possible solutions: enhance the bandwidth of Network 3 or modify the topology of Area 3. Here, we adopt the latter due to its economy and add the link between AG. The resultant results are presented in Table 4-3. Hence, the advantages of the bounded model are two-fold. It not only provides latency bounds for relay setting, but assists in the planning, design, and assessment of SIPS networks.

Admittedly, the relay setting especially the delay setting is not constrained by communications only. Some protective relays like three-stage current relays and backup relays, shorten or prolong the time delay intentionally according to the protection scheme design. Therefore, in the SIPS design, communication constraints, SIPS operation requirements, and engineering experience need to be considered collectively.

4.3.2 Case 2: Substation-Area Protection

In terms of substation-area protection, the proposed bounded model is applied in IEC 61850 T2-2 substation system as shown in Fig. 4.8 [44]. The upper bounded communication delay in the T2-2 substation is calculated at 0.120 ms using the deterministic network calculus method. Meanwhile, the simulation is carried out with OPNET modeler, which is widely used for substation-communication simulation. The parameters can be found in [44], and the corresponding simulation results are shown in Fig. 4-9.

In addition to the communication in a substation, the communication between two substations is also performed. Two IEC 61850 T2-2 substation systems 100 km apart are used and the communication follows the IEC 61850-90-1 standard. The upper bounded communication delay is calculated as 0.572 ms and the simulation results are presented in Fig. 4-10.

Figs. 4-9 and 4-10 show that the communication delays varies under different traffic conditions (the data stream rate is set to 35% for light traffic and 75% for heavy traffic). The communication delays in reality may violate the fixed or average value of constant or stochastic models; while they are all below the deterministic upper bounds 0.120 ms and 0.572 ms.

As aforementioned, power system protection is a kind of time critical and reliability oriented applications. Protection engineers are demanded to design and examine the communication infrastructure thoroughly to ensure all the measurements will be delivered to protective devices below the maximum allowable delays. Therefore, the proposed bounded communication delay is promising in practice.

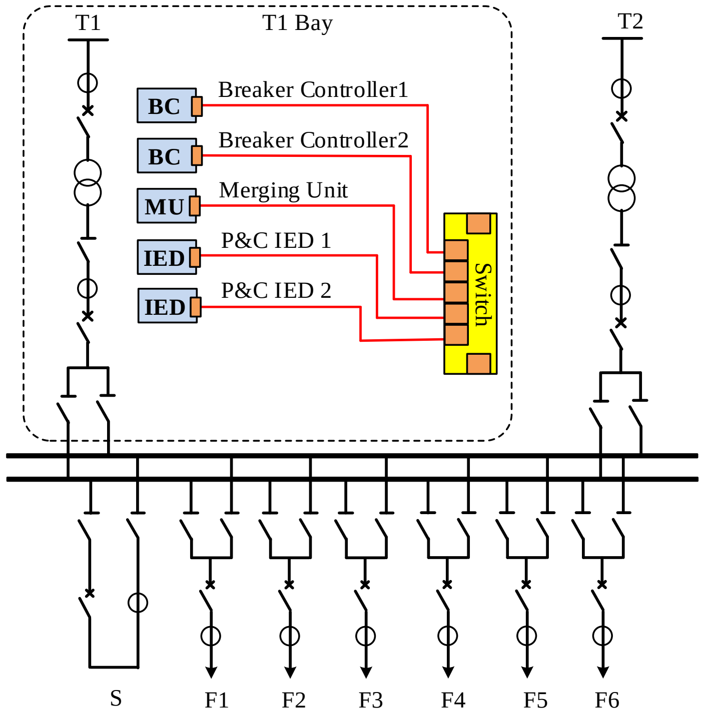

(a) Component connection diagram

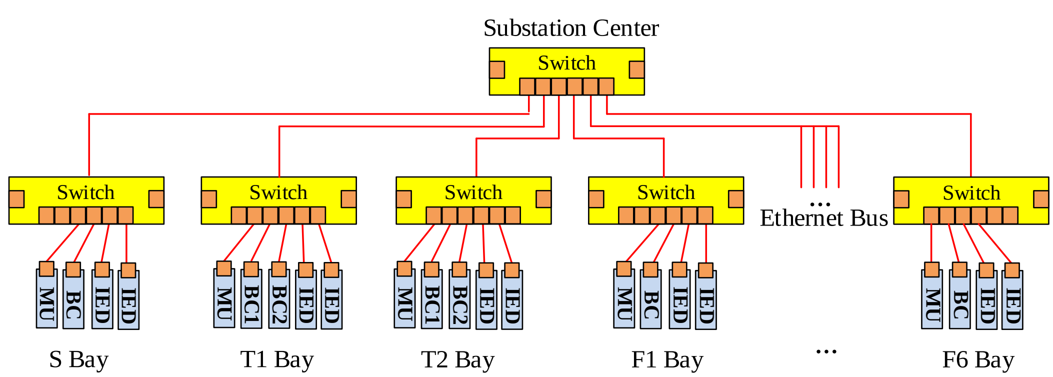

(b) Network connection diagram

Fig. 4–8. IEC 61850 T2-2 substation system.

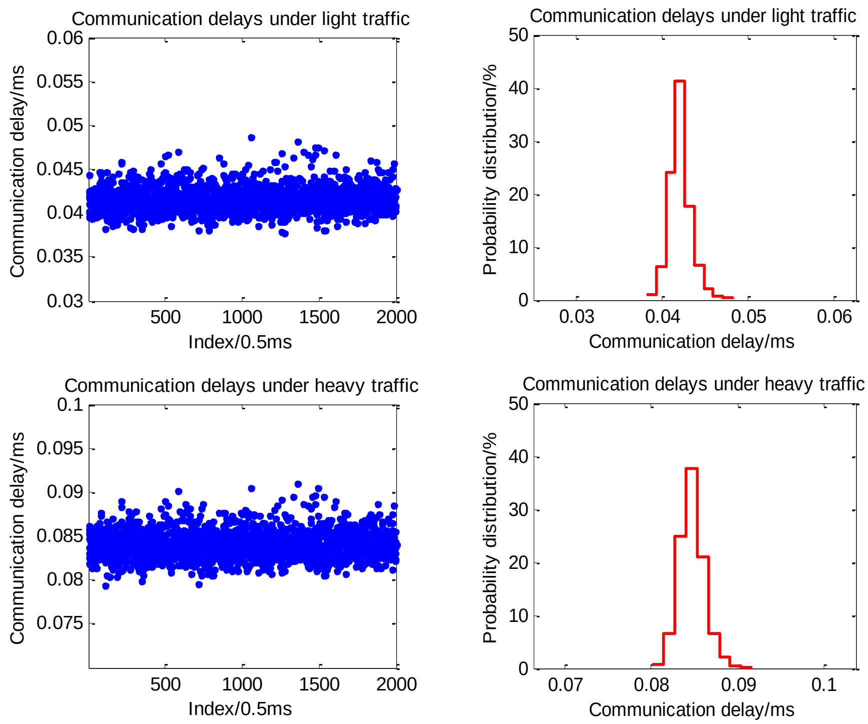

Fig. 4–9. SV delays in a substation: records and statistics.

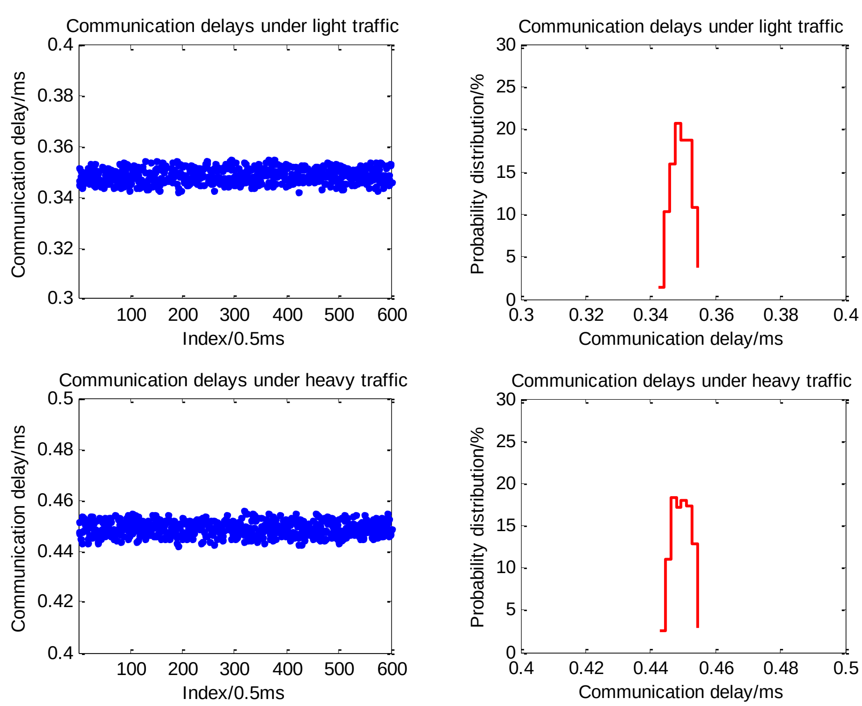

Fig. 4–10. GOOSE delays between two substations: records and statistics.

4.4 Conclusion

The SIPS has received extensive attention in the last decade, especially with the rapid development of WAMS and IEC 61850 technologies. The SIPS extends the protection scope from local equipment to the integrity of a power system, and thus requires fast and reliable communications. This work focuses on the SIPS latency and proposes the new modeling method for the communication delay. The contributions of this research work can be summarized as follows.

First, the communication delay is investigated over wide areas and long terms, and a bounded model is proposed for the communication delay of wide-area protection. Since protection applications expect predictable or predetermined time delays for relay setting, the bounded model is more favorable than the constant or stochastic model in the literature. Specifically, the bounded model is derived from the existing infrastructure (e.g., PDC, SONET/SDH, and switched Ethernet network), which does not demand any not-yet-implemented hardware or technologies.

Second, the bounded model is applied for the communication delay of substation-area protection as well. Here, the network calculus theory is used, which deals with performance guarantees instead of average values in the classical queuing theory. Meanwhile, the various factors such as the priorities of GOOSE and SV messages, the communications in a substation (IEC 61850-9-2), and the communications between substations (IEC 61850-90-1) are considered. The bounded model suggests the network's worst-case performance, and thus can be viewed as an important tool for protection engineers.

Moreover, the proposed model is employed in IEC 61850 T2-2 substation system, IEEE 14 bus system, and China Southern Power Grid SDH system. It is founded that the proposed model not only provides latency bounds for relay setting, but plays an advantageous role in the planning, design and assessment of SIPS networks.

5 Uncertain Communication Loss in WAMSs

In this chapter, the uncertain data loss events in WAMSs are investigated, with special focus on the synchronization signal loss and synchrophasor data loss events. First, the statistics of historical synchronization signal loss events are presented and analyzed, and the potential reasons and solutions of synchronization signal loss are discussed. Second, the statistics of historical synchrophasor data loss events are provided, which suggest that the majority of synchrophasor data loss events only involve one to three continuous package losses. Hence, the scenario of a small amount of synchrophasor data loss is studied and a set of estimation methods are applied for synchrophasor data loss.

5.1 Statistics of Data Loss

To better understand the uncertain data loss in WAMSs, the historical PMU data and FDR data from OpenPDC and FNET/GridEye are used, and the related events including synchronization signal loss and synchrophasor data loss events are extracted and analyzed, respectively.

5.1.1 Statistics of Synchronization Signal Loss

In reality, synchronization signal (i.e. GPS-timing single) loss is the main factor affecting synchronization measurement accuracy, since most PMUs and FDRs use the GPS-timing single as time synchronization references. The GPS-timing-signal loss events in historical PMU and FDR data are studied first.

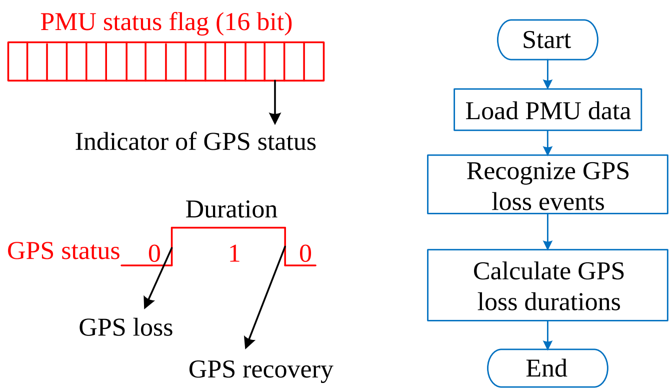

(a) Status flag (b) Flow chart

Fig. 5–1. Statistical approaches.

The PMU data frame contains a one-bit GPS status flag as shown in Fig. 5-1 (a), in which the GPS state “1” or “0” means whether the GPS loss occurs, and the variance of GPS states suggests when the GPS loss starts and ends. Then, the number and the duration of GPS loss events can be obtained as shown in Fig. 5-1 (b).

In this way, the numbers of the PMUs suffering GPS loss with different time periods (e.g., annually, monthly, and hourly), and the numbers of the related PMUs with different GPS-loss durations are obtained in Fig. 5-2 (a)-(d), respectively. Fig. 5-2 (a) shows the number of the surveyed PMUs increased from 26 in 2009 to 83 in 2012, and Fig. 5-2 (b) shows the distribution of the GPS loss events from 2009 to 2012 over different time durations.

The FDR data frame does not include the GPS status flag, but records GPS signal strengths. To be specific, an FDR updates the number of locked GPS satellites in every minute, which represents the strength of GPS signals and further implies the possibility of GPS loss events. For example, four FDRs with different GPS signal strengths are shown in Fig. 5-3: (a) strong strength (i.e. the FDR always locks 6-12 GPS satellites), (b) medium strength (i.e. the FDR locks 2-6 GPS satellites), (c) weak strength (i.e. the FDR only locks 0 or 1 GPS satellite and GPS-signal- loss events frequently occur), and (d) variable strength, in which the number of locked GPS satellites varies in a random way or with certain patterns.

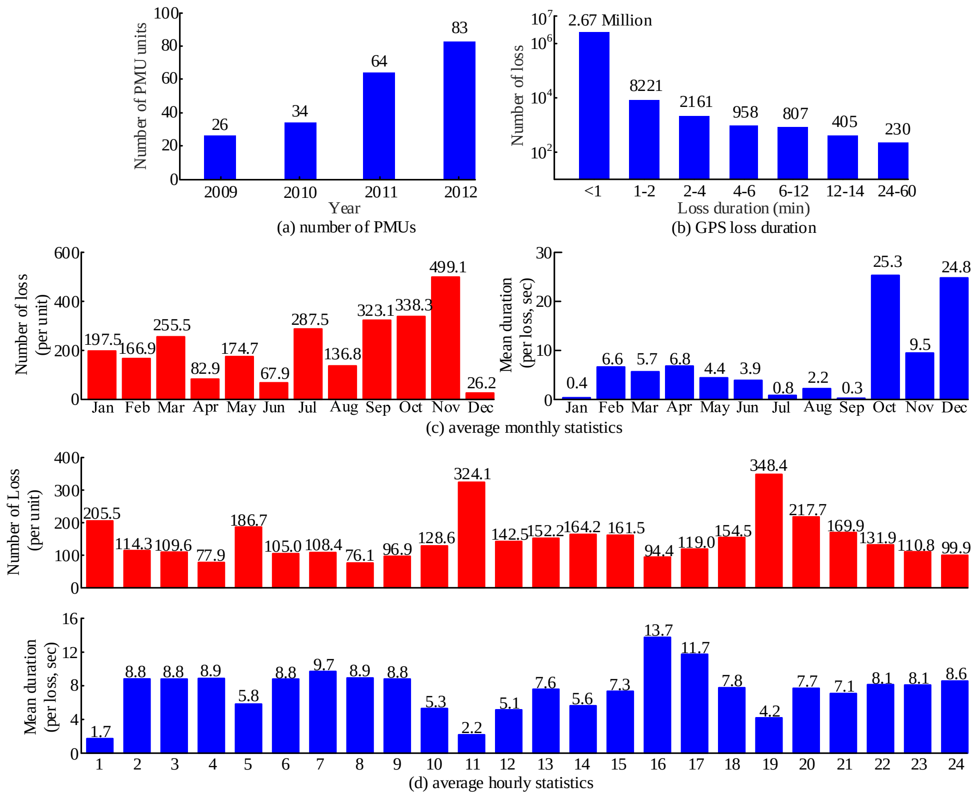

Fig. 5–2. Statistical results of GPS loss events in PMUs from 2009 to 2012.

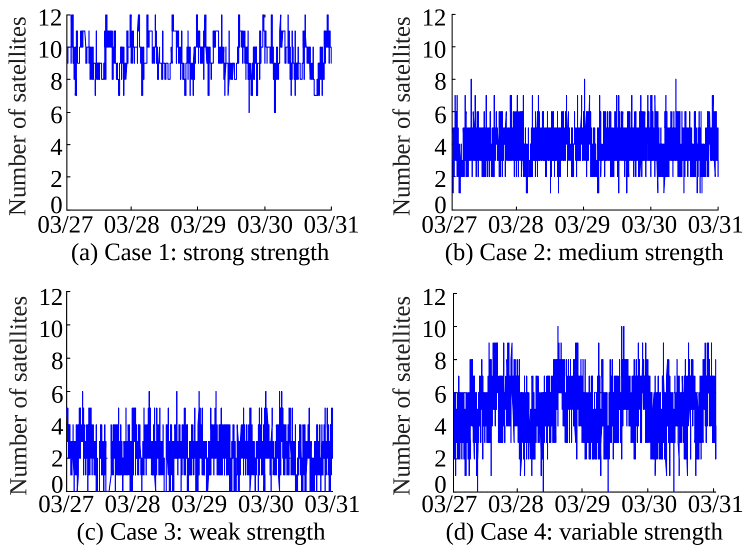

Fig. 5–3. Statistical results of locked satellites in FDRs.

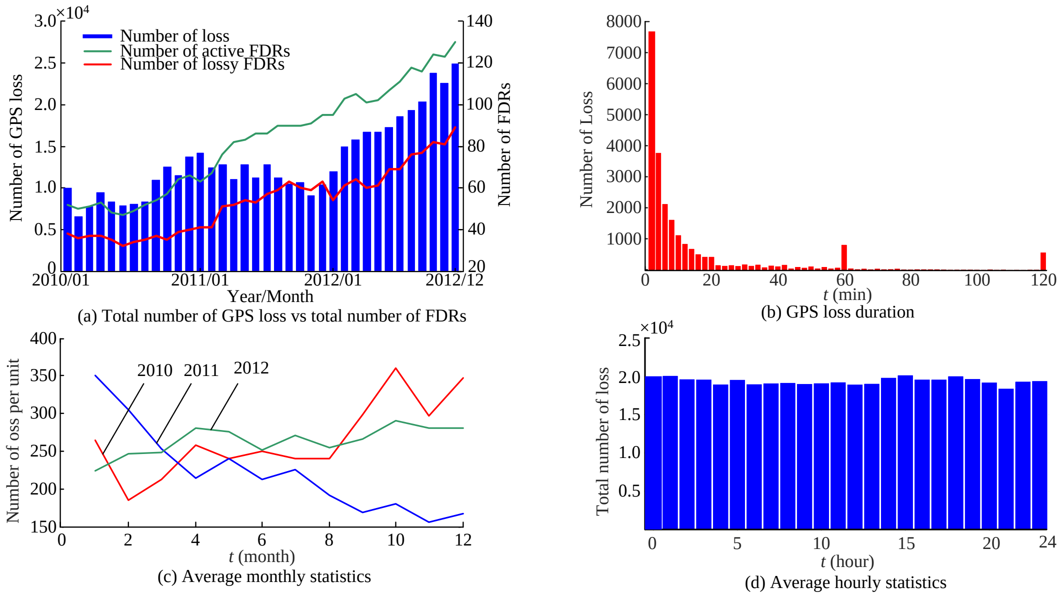

Fig. 5–4. Statistical results of GPS loss events in FDRs from 2010 to 2012.

Using the similar statistical approaches in Fig. 5-1 (b), the numbers of the FDRs suffering GPS loss with different time periods (e.g., annually, monthly, and hourly), and the numbers of the related FDRs with different GPS-loss duration are presented in Fig. 5-4 (a)-(d), respectively.

Figs. 5-2 (a)-(b) and 5-4 (a)-(b) show that a large number of PMUs and FDRs experienced GPS loss, and as PMUs and FDRs were increasingly deployed in the past years, the numbers of GPS loss events grew constantly. The average GPS loss rate and average GPS loss duration for the PMU from 2009 to 2012 were 5 times per day and 6.7 second, respectively, and the average GPS loss rate for the FDR from 2010 to 2012 was about 6 to 10 times per day. Moreover, the statistical results of both PMUs and FDRs suggest that the majority of GPS loss events recover within a short period of time, and the number of GPS loss events decrease exponentially as the GPS recovery time increases. Note that FDRs stop sending data if lose GPS timing signals over 1 or 2 hours, which leads to high count values at 60 minutes and 120 minutes in Fig. 5-4(b).

Figs. 5-2 (c)-(d) and 5-4 (c)-(d) show monthly and hourly trends of the surveyed GPS loss events of PMUs and FDRs, respectively. It is observed that 1) the GPS loss events of PMUs more frequently occurred at certain hours in a day, e.g., 11 AM and 7 PM UTC (Coordinated Universal

Time), whereas the GPS loss events of FDRs evenly distributed over a day; and 2) some specific pattern were diluted in a large amount of statistical data, suggesting no obvious seasonal or monthly trend or universal daily pattern that matches for all the units.

Moreover, the large amount of statistical data can be used for big data and machine learning studies, which are becoming very popular in modern power systems. This study will be followed up in the future work.

5.1.2 Statistics of Synchrophasor Data Loss

Partially for confidential reasons, there are no public data or statistics showing PMU data loss and/or latency events in details. This work takes advantage of the GPS-synchronized wide-area FNET/GridEye and records the FDR data loss and latency events over four weeks in Fig. 5-5.

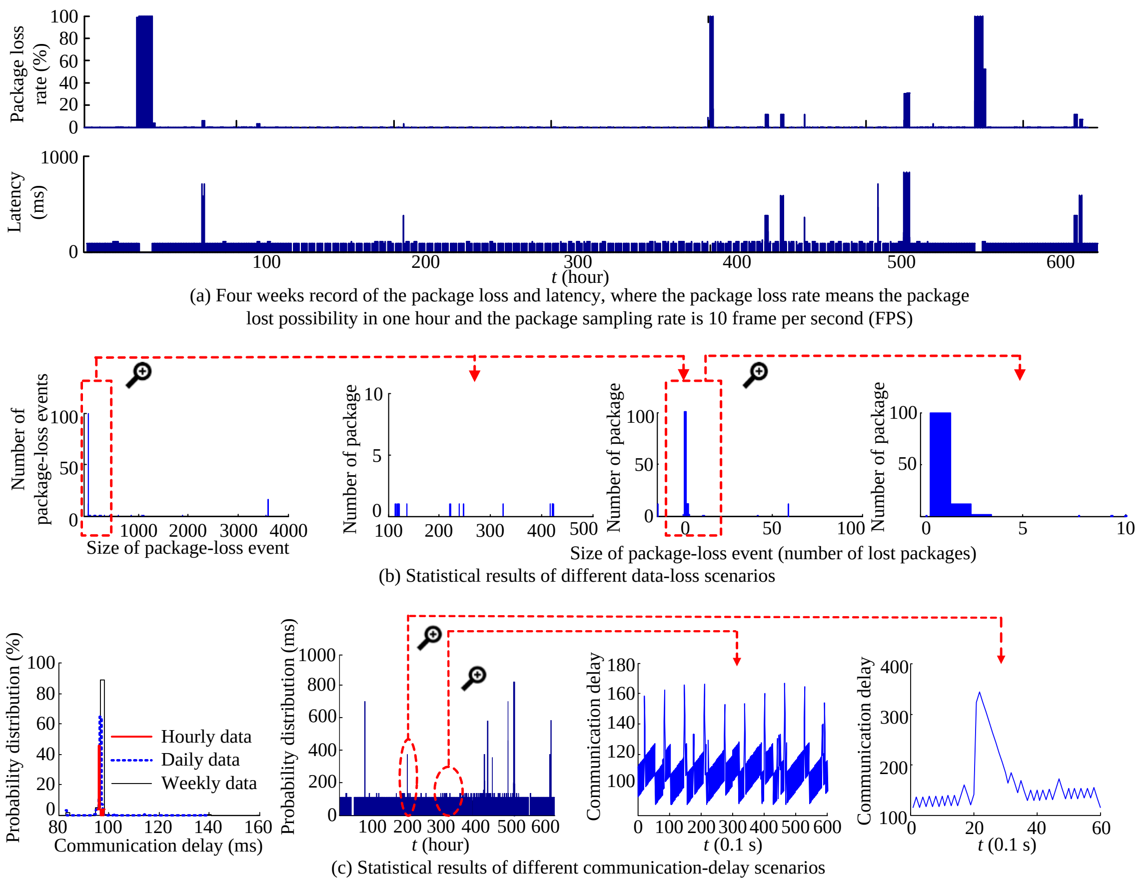

Fig. 5–5. Data loss and latency events in FNET/GridEye.

It is observed from Figs. 5-5 (a) and (b) that the data loss events randomly occur and are often accompanied by high communication delays. Also, the data loss events display diverse scenarios but 95% of them only involve one to three continuous package losses. This implies that the large amounts of package losses are small probability events.

5.2 Solutions of Data Loss

5.2.1 Potential Reasons and Solutions for Synchronization Signal Loss

Accurate and reliable synchronization signals play a critical role in synchrophasor systems. They provide the common timing reference for data measurement and synchronization, and largely determine the accuracy and availability of synchrophasor data. However, according to the statistics in section 5.1, a large number of PMUs and FDRs experienced timing signal loss (i.e. GPS signal loss). The potential reasons and solutions are explored in this section.

A. Potential Reasons

Theoretically, the GPS signal availability, especially the strength, might be affected by two factors: the weather and the surrounding of GPS antennas.

The weather events primarily refer to the ionospheric scintillation and solar radio burst, which can degrade GPS signal performances [46]. In particular, the strongest scintillation normally occurs at the equatorial regions. This means more interference signals will be applied to the GPS antenna located in the low latitude.

In order to investigate the impact of weather events on GPS signal loss, two studies are performed. First, the average yearly GPS-signal-loss events of the FDR from 2010 to 2012 are counted.

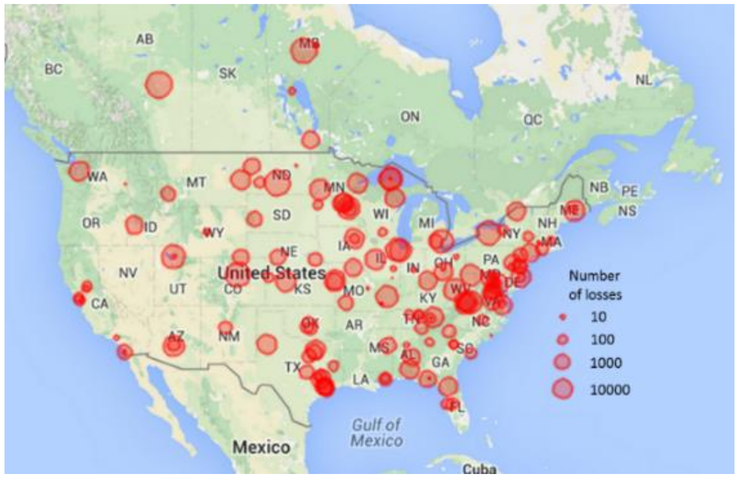

Fig. 5–6. Spatial distribution of GPS signal loss in North America.

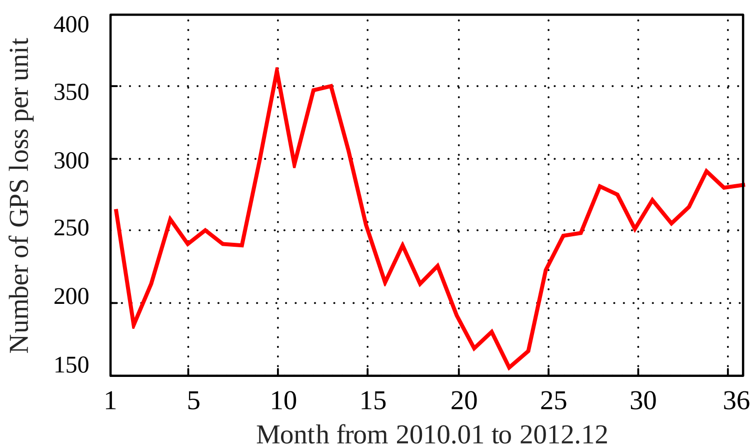

Fig. 5–7. Temporal distribution of GPS signal loss from 2010 to 2012.

As shown in Fig. 5-6, the GPS-signal-loss events of all FDRs across North America are depicted in the spatial manner, while no clear geological pattern is identified from the historical data. Second, the average monthly GPS-signal-loss events of the FDR from 2010 to 2012 are calculated as shown in Fig. 5-7, and the historical solar activities from 2010 to 2012 are reviewed (it is reported that the largest solar activity happened on March 7, 2012 00:24 UTC – the sun unleashed an X5.4-class solar flare). By comparing the trend in Fig. 5-7 and the trend in the reference, no obvious relationship between GPS signal loss and solar radio bursts is found. These two studies imply that the overall GPS signal availability is not significantly affected by the weather.

In addition, the GPS signal availability is also affected by the surrounding of GPS antennas [46]. For example, an FDR is usually installed indoor with a directional GPS antenna instead of an omnidirectional GPS antenna. The performance of the antenna or antenna reception may be affected by the surrounding. For instance, whether the antenna is installed near a window with an open view to the sky, and whether the antenna reception is located nearby the buildings or obstacle that frequently reflect or block GPS signals.

2.2 Potential Solutions

To improve the accuracy and availability of GPS signals, the performance of GPS receivers should be considered first. For instance, if a PMU uses an on board GPS receiver, the PMU can parse the GPS signal strength information, e.g., the number of locked satellites from a GPS receiver, and further track the GPS signal strength; and if a PMU uses GPS signals as synchronization signals, the GPS signal strength can be enhanced through installing omnidirectional antenna on the roof with the open sky.

Note that the antenna type will impact the GPS signal availability. Directional antennas transmit and receive signals in a particular direction, so they are generally subject to a particular reception pattern (e.g., they would lower the signal availability when the directional path is affected). In contrast, omnidirectional antennas transmit and receive signals in all horizontal directions, enabling users to use the GPS antenna without concerning the antenna's reception pattern. Therefore, omnidirectional antennas can improve reception in such terrains where directional path would be affected.

Some emerging data analytics solutions can also improve the timing accuracy of synchrophasor measurements. For the lost or drifted timing signals, the context data in the time range with available and accurate timing, or the data from other units, can help reconstruct the missing information. Data interpolation and data realignment tools also provide the possibility to patch the timestamp or shift the data back to its correct position.

Moreover, since the availability of GPS signals is difficult to be guaranteed, some backup synchronized timing sources can be used, such as network time protocol (NTP), e-Loran, and chip scale atomic clock (CSAC). Several backup synchronized timing technologies have been employed for synchrophasor measurement. It is demonstrated that they provide ultra-high timing accuracy and reliability to meet IEEE Standards [45], [46].

5.2.2 Proposed Estimation Methods for Synchrophasor Data Loss

As discussed in Part I, a number of synchrophasor applications (e.g., Class-A applications) prefer accurate and complete synchrophasor data. The data loss issue may lower and even disable the performances of certain synchrophasor applications. The incomplete or missing data can make the power grid unobservable and vulnerable, and even aggravate the cascading effects in large-scale blackouts [131]-[140]. PMU Application Requirements Task Force at North American Synchrophasor Initiative (NASPI) has been working on standardizing and quantifying the requirements of synchrophasor applications.

To address the data loss issue, several advanced data recovery techniques were proposed in the literature [121]. Those data recovery techniques are applicable for off-line applications but indeed costly for the majority of real-time applications. Moreover, as discovered previously, about 95% data loss events involve only one to three lost packages and a large amount of data lost is a small probability event. Hence, this work focuses on the scenario of a small amount of package losses, and examines a set of estimation methods to mitigate the corrupted and missing data, including substitution, interpolation, and prediction.

A. Lagrange Interpolating Polynomial Method

Currently, there is no standardized method to address the issues of synchrophasor data loss. Most commercial PDCs use the substitution method, in which the lost data are simply set to zero. Obviously, this method will lower the data accuracy and completeness. One alternative method is interpolation, and a Lagrange interpolating polynomial method is presented below.

In general, the Lagrange polynomial $L(x)$ passes through a set of given data points $(x_1, y_1) = f(x_1)$, $(x_2, y_2) = f(x_2)$,..., $(x_n, y_n) = f(x_n)$, and other points can be approximatively calculated with

$$L(x) = \sum_{j=1}^{n} y_j \cdot \ell_j(x) = \sum_{j=1}^{n} y_j \cdot \prod_{\substack{k=1 \\ k \neq j}}^{n} \frac{x - x_k}{x_j - x_k} \tag{5.1}$$

where $\ell_j(x)$ is the coefficient in the Lagrange polynomial.

Considering the trade-off between algorithm accuracy and hardware-cost, n is selected as 3 and (5.1) can be rewritten as the quadratic interpolation in (5.2).

$$\begin{aligned} L(x) = {} & y_1 \frac{(x - x_2)(x - x_3)}{(x_1 - x_2)(x_1 - x_3)} + y_2 \frac{(x - x_1)(x - x_3)}{(x_2 - x_1)(x_2 - x_3)} \\ & + y_3 \frac{(x - x_1)(x - x_2)}{(x_3 - x_1)(x_3 - x_2)} \end{aligned} \tag{5.2}$$

The first case assumes only one synchrophasor package is lost. The simple lost data can be estimated with the quadratic interpolation in (5.2).

Also, since only three points are required in the estimation, the lost data can be further estimated with the weighted interpolation. For instance, the lost point v_4 as shown in Fig. 5-8(a) can be calculated with (5.2) in the following ways

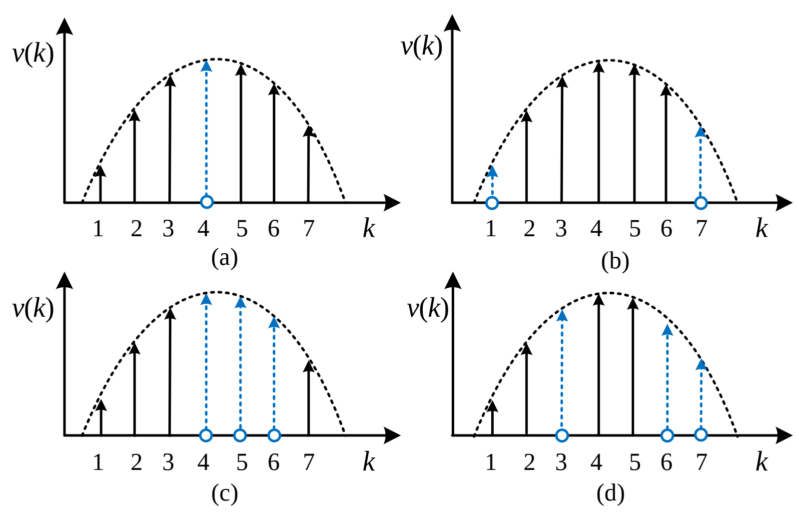

Fig. 5–8. Synchrophasor data loss with different conditions.

$$\hat{v}_4\big|_{1,2,3} = v_1 - 3v_2 + 3v_3 \tag{5.3}$$

$$\hat{v}_4\big|_{2,3,5} = -\frac{1}{3}v_2 + v_3 + \frac{1}{3}v_5 \tag{5.4}$$

$$\hat{v}_4\big|_{3,5,6} = \frac{1}{3}v_3 + v_5 - \frac{1}{3}v_6 \tag{5.5}$$

$$\hat{v}_4\big|_{5,6,7} = 3v_5 - 3v_6 + v_7 \tag{5.6}$$

$$\hat{v}_4 = c_1\hat{v}_4\big|_{1,2,3} + c_2\hat{v}_4\big|_{2,3,5} + c_3\hat{v}_4\big|_{3,5,6} + c_4\hat{v}_4\big|_{5,6,7} \tag{5.7}$$

where c_1, c_2, c_3 and c_4 are the coefficients in the weighted interpolation. The average weights are used here since their practicality and simplicity.

The special condition as depicted in Fig. 5-8(b) is considered, in which the first or last package in a dataset is lost. Then, the estimates can be calculated with the polynomial extrapolation in (5.8) and (5.9), respectively.

$$\hat{v}_1 = 3v_2 - 3v_3 + v_4 \tag{5.8}$$

$$\hat{v}_7 = v_4 - 3v_5 + 3v_6 \tag{5.9}$$

The second case considers the continuous package loss and the lost data can be estimated with the extrapolation as well. For instance, three points as shown in Fig. 5-8(c) are lost and they can be recursively estimated as follows

$$\hat{v}_4 = v_1 - 3v_2 + 3v_3 \tag{5.10}$$

$$\hat{v}_5 = v_2 - 3v_3 + 3\hat{v}_4 \tag{5.11}$$

$$\hat{v}_6 = v_3 - 3\hat{v}_4 + 3\hat{v}_5 \tag{5.12}$$

Note that the extrapolation assumes the data are smooth and performs poorly for the dramatically changing data. Also, a maximum package loss amount is normally preset in power system engineering, and an alarm will arise when the actual package loss number exceeds the maximum amount.

In addition, the practical synchrophasor package may be lost discontinuously and randomly, and they can be compensated with the interpolation and extrapolation collectively. A simple example is presented in Fig. 5-8(d) and the discontinuous points can be calculated as follows

$$\hat{v}_3 = \frac{v_2}{3} + v_4 - \frac{v_5}{3} \tag{5.13}$$

$$\hat{v}_6 = \hat{v}_3 - 3v_4 + 3v_5 \tag{5.14}$$

$$\hat{v}_7 = v_4 - 3v_5 + 3\hat{v}_6 \tag{5.15}$$

Here, the 3nd point in Fig. 5-8(d) can be further estimated with the weighted interpolation, in which the estimation accuracy is expected to improve. Also, the estimation errors in above estimations are unavoidable and can be expressed as

$$E(x) = f(x) - L(x) = \frac{f^{(n)}(x)}{3!} \cdot \prod_{k=1}^{3} (x - x_k) \tag{5.16}$$

Further, for the current and voltage with harmonics as $v_k = v_0 + \sum_{h=1}^{\infty} v_h \sin(h\omega t + \phi_h)$, the related estimation error can be written as

$$E(t) \le \frac{\omega^3}{3!} \sum_{h=1}^{\infty} (v_h h^3) \left| \prod_{j=1}^{3} (t - t_j) \right| \tag{5.17}$$

Typically, for the ROCOF or frequency measurement, its accuracy is evaluated with absolute errors (e.g., frequency error Hz or ROCOF error Hz/s), while for the phasor measurement, its accuracy is evaluated with the TVE as

$$\mathrm{TVE}(n) = \sqrt{\frac{(\hat{X}_r(n) - X_r(n))^2 + (\hat{X}_i(n) - X_i(n))^2}{(X_r(n))^2 + (X_i(n))^2}} \tag{5-18}$$

where $X_r(n)$ and $X_i(n)$ are the sequences of theoretical values of the input signal at the instant of time (n), and $\hat{X}_r(n)$ and $\hat{X}_i(n)$ are the sequences of estimates. The TVE of P class and M class PMUs is required to be less than 1% in steady-state in IEEE Standard C37.118.

B. Forecasting Method

In addition to the substitution and interpolation, the prediction is also widely used in data estimation [141]-[142]. Here, the synchrophasor data are viewed as an observed time series driven by a stochastic process and represented by a state equation and a measurement equation as follows:

$$x_{k+1} = A_k x_k + B_k \omega_k \tag{5.19}$$

$$y_k = C_k x_k + D_k v_k \tag{5.20}$$

where x_{k+1} is the state that characterizes the measurement y_k; it is a variable of the time series determined by the previous state x_k and the noise term ω_k introduced at each k; A_k, B_k, C_k and D_k denote the corresponding coefficients.

The unknown system parameters $\theta_k=\{A_k, B_k, C_k, D_k\}$ and states $\{x_k\}_k$ can be estimated through a finite set of received signal measurement data $\{y_1, y_2, \ldots\}$. Also, the parameters in (5.19) and (5.20) are estimated using the prediction error minimization (PEM) algorithm here, with the objective of minimizing prediction errors. The PEM updates the measurement set every time when the new measurement comes in, such that the whole model is updated with the new measurement set to keep up with time-varying parameters. The PEM algorithm estimates the system parameters by minimizing a least square cost function as follows:

$$\min J_N = \min \frac{1}{N} \sum_{k=0}^{N-1} \left\| y_k - \hat{y}_k \right\|_2^2 \tag{5.21}$$

When the lost synchrophasor data are treated as the synchrophasor data in future, it can be recursively predicted on the basis of the previous states and estimated parameters. In particular, the PEM algorithm employs a finite number of stored measurements for the next prediction where the store size can be chosen as small as the algorithm has a solution. Thus, different from the widely used artificial neural networks based prediction approaches which require large historical data for data modeling and training, the proposed prediction method results in acceptable hardware cost and it is applicable for the data estimation of on-line applications [45], [46].

5.3 Case Study

In order to demonstrate the performance of the proposed methods, the simulation with MATLAB is performed here. Because the power system data may vary regularly in normal operation but dramatically change in a fault or disturbance, the real PMU data in a fault event are used as inputs as shown in Fig. 5-9.

Because of the limited space, three groups of twenty samples are selected from the pre-fault, in-fault, and post-fault states and further used as the test data as shown in Fig. 5-10.

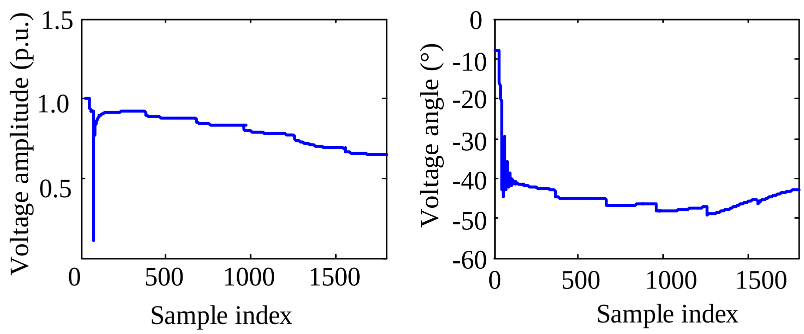

(a) Voltage amplitude (b) Voltage angle

Fig. 5–9. PMU data profile in one minute.

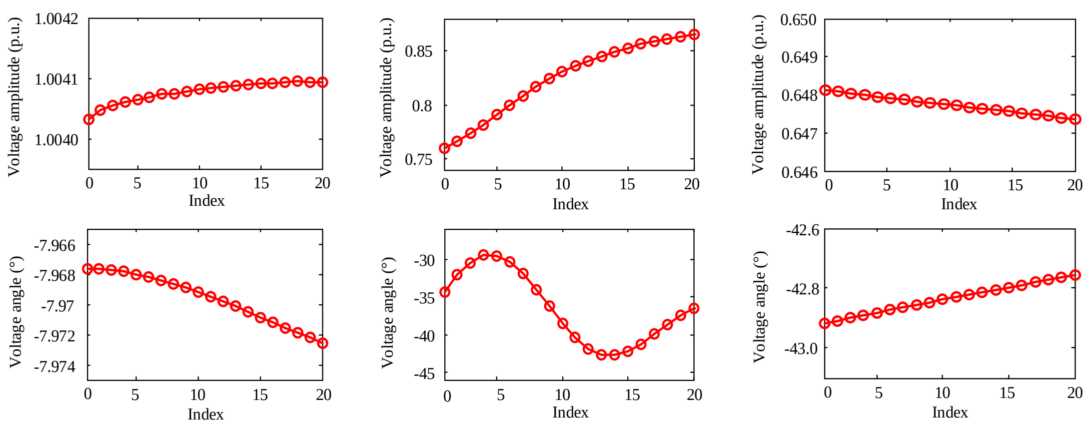

(a) Data in the pre-fault state, (b) Data in the fault state, and (c) Data in the post-fault state.

Fig. 5–10. Test Data in diverse conditions.

5.3.1 Case 1: Substitution and Interpolation based Estimation

The substitution and the interpolation based estimation methods are tested. First, three sets of twenty samples in Fig.6 representing the different conditions in power grids are used as test inputs. Then, the 5^{th}, (5^{th}, 6^{th}), (5^{th}, 6^{th}, 7^{th}),…, (5^{th}, …, 14^{th}) samples are manually set lost, and the proposed weighted interpolation method with different times of estimation (e.g., two times and three times of estimation) is applied to estimate the lost data. The corresponding simulation results are presented in Fig. 5-11.

Note that this work focuses on the scenario of a small amount of synchrophasor data loss and the simulation studies the scenario of one to ten continuous package losses. Hence, the twenty samples are good enough for the maximum continuous package losses.

For the substitution, the lost sample is treated as "zero" and its TVE sharply increases to 100%. Hence, the continuous data loss will lower the accuracy of synchrophasor data and even lead to the malfunction of certain synchrophasor applications.

For the interpolation, it is observed that in the pre-fault and post-fault states, the lost data can be efficiently estimated (TVE<1%), whereas in the faulty state, the estimation error is acceptable only in the scenarios of one or two continuous package losses.

Moreover, the estimation accuracy is improved by the weighted interpolation, e.g., the three times estimation normally presents lower TVE than the one time estimation. The estimation accuracy is also affected by the nature of synchrophasor data, e.g., the TVE of the scenario of nine continuous data loss in Fig. 5-11(b) suddenly drops to 1% since the data changes gently in this field. Therefore, the proposed interpolation method can adaptively estimate the missing data in different conditions, and the estimation results are acceptable in the scenario of the small amount of data loss.

Further, the proposed Lagrange interpolating polynomial algorithm only includes simple addition and multiplication as shown in (5.2)-(5.15), which can be embedded in a lookup table. Thus, the proposed interpolation method can be efficiently employed in a PDC in practice.

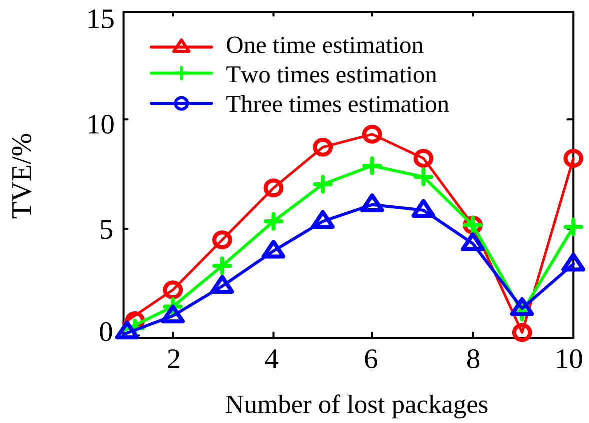

(a) Simulation results in the pre-fault state

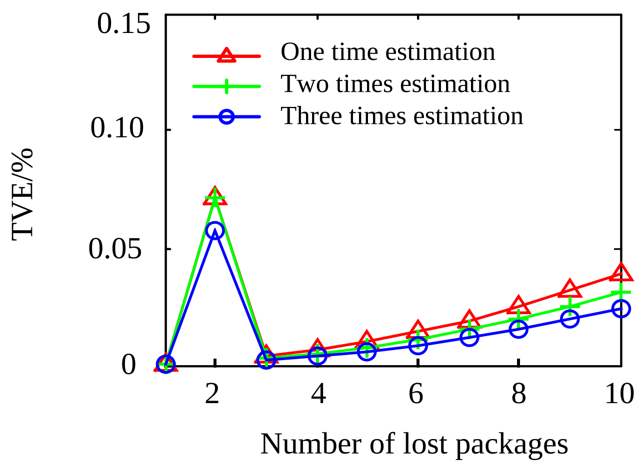

(b) Simulation results in the fault state

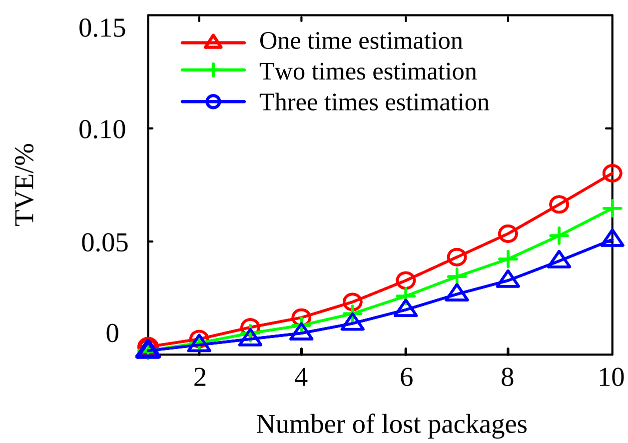

(c) Simulation results in the post-fault state

Fig. 5–11. Simulation results of the weighted interpolation method.

5.3.2 Case 2: Prediction based Estimation

The perdition method with the same inputs in Figs. 5-10 (b) and (c) is tested as well. It is observed from the simulation results in Figs. 5-12 and 5-13 that the prediction method can estimate the lost data with high accuracy, while a bit high prediction error still exists in the scenario of continuous data loss and/or dynamic data changes.

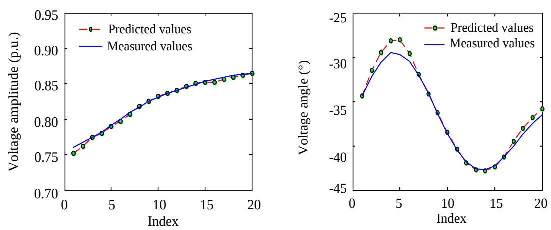

Case 1: One package loss in the fault state.

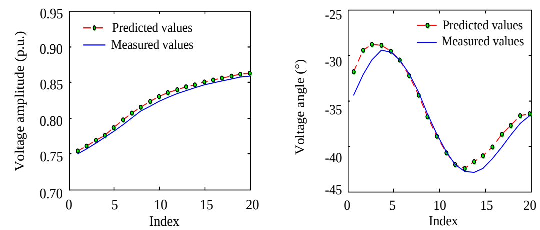

Case 2: Two package losses in the fault state.

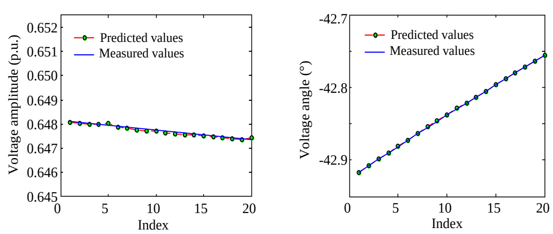

Case 3: One package loss in the post-fault state.

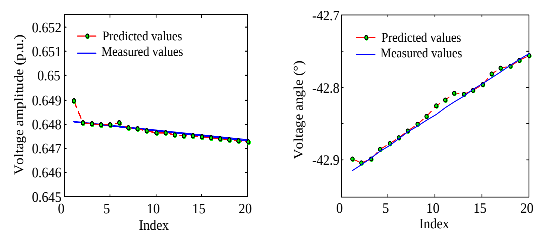

Case 4: Two package losses in the post fault state.

Fig. 5–12. Simulation results of the prediction method.

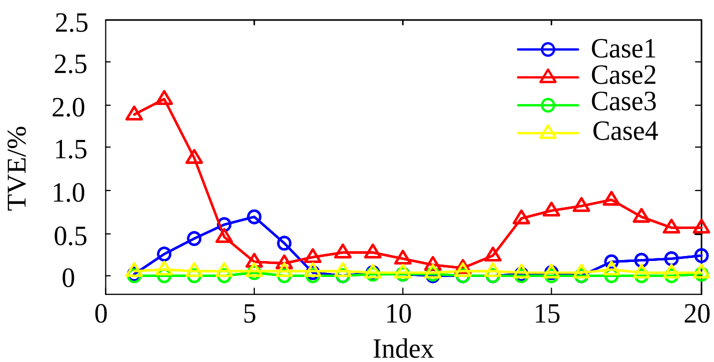

Fig. 5–13. TVE results of the prediction method.

Table 5-1 A brief review of the three estimation methods.

Estimation Method	Substitution	Interpolation	Prediction
Accuracy	Low	High	High
Speed	Ultra-Fast	Very-Fast	Fast
Complexity	Low	Medium	High

For example, for the voltage angle values in Figs. 5-8 (b) and (d), the high prediction accuracy is obtained for the voltage angle varying in a small range whereas the high prediction errors happen to certain voltage angles dynamically changing.

According to the above analysis, a brief review of the three estimation methods is provided in Table 5-1. The interpolation method presents comparable estimation accuracy as the prediction method but requires less hardware cost. Therefore, the interpolation method achieves the trade-off between accuracy and complexity. It is favorable for the estimation of the corrupted and missing synchrophasor data.

5.4 Conclusion

A number of synchrophasor applications prefer accurate, complete, and timely data, and their performances may be impacted or even disabled due to data quality issues. This chapter investigates the uncertain data loss issue for synchrophasor applications and pays particular attention to the synchronization signal loss and synchrophasor data loss events.

First, the historical synchronization signal loss events are analyzed, and the potential reasons and solutions are discussed. It is found that a large number of PMUs and FDRs experienced GPS signal loss, and this issue might get worse under the bad weather and surrounding. It is ad-vantage to optimize the location of GPS antennas and deploy advanced ICTs and backup schemes.

Second, the issue of synchrophasor data missing and incomplete is studied. For the off-line applications, the missing data can be processed in the control center with advanced information recovery techniques; while for the real-time applications, the incomplete data normally are directly delivered to the applications, which is unfavorable for certain applications.

Further, it is observed from the statistics in Part I that about 95% data loss events involve only one to three lost packages. Hence, this work focuses on the scenario of a small amount of synchrophasor data loss and proposes the estimation method with Lagrange interpolating polynomial algorithms. Compared with the substitution and the prediction methods, the interpolation method can estimate the lost data in diverse conditions adaptively and achieve the trade-off between accuracy and complexity. Moreover, the interpolation method requires simple calculations only, and thus can be embedded in a lookup table and implemented efficiently in a practical PDC.

6 Conclusion and Future Work

6.1 Summary of Contributions

The research work in this dissertation investigates the uncertainties in Smart Grid, with special focus on the uncertain wind power generation in WECSs and the uncertain wide-area communication in WAMSs. The contributions can be summarized as follows:

This research studies the uncertain wind power generation in WECSs. First, the challenges of WECSs are analyzed, especially the uncertain wind power generation in WECSs. Second, the new modeling and control methods of WECSs are developed. The new modeling method considers the spatial and temporal distribution of wind speed disturbances, and deploys a box uncertain set in wind speed models, which is more realistic for practicing engineers. The improved control method takes wind speed forecasting and wind turbine dynamics into account, which achieves a balance between power outputs maximization and operating costs minimization and further improves the overall efficiency of wind power generation. In specific, through the proposed modeling and control methods, the wind power control problem is developed as a min-max optimal problem and efficiently solved with semi-definite programming.

This research also works on the uncertain wide-area communication in WAMSs, especially the uncertain communication delay and the uncertain communication failure (i.e. data loss). First, the real-world communication delay is measured and analyzed, and the bounded modeling method for the communication delay is proposed for wide-area applications and further applied for system-area and substation-area protection applications, respectively. The proposed bounded modeling method could be an important tool in the planning, design, and operation of time-critical wide-area applications. Second, the real synchronization signal loss and synchrophasor data loss events are measured and analyzed. For the synchronization signal loss, the potential reasons and solutions are explored. For the synchrophasor data loss, interpolation and forecasting based estimation methods are presented, respectively. The proposed methods could improve the accuracy and availability of WAMSs, and mitigate the effect of communication failure and data loss on wide-area applications.

6.2 Future Works

The following directions may be considered in future works.

First, innovative short-term wind speed forecasting methods may be applied to the proposed WECS control, in which the values of the norm-bound and the optimal tracking reference can be obtained through the forecasting.

Second, the bounded model of the communication delay may be applied to wide-area dimpling control applications, and the quantitative method may be developed to determine the maximum acceptable communication delay for wide-area control systems.

Third, in view of the communication failure and data loss in state estimation application, advanced forecasting methods may be deployed to forecast the power system states and forecasting-aided dynamic state estimation systems may be developed.

References

[1] P. Kundur, *Power System Stability and Control*, McGraw-Hill, 1994.

[2] A. Ipakchi and F. Albuyeh, "Grid of the future," *IEEE Power & Energy Mag*., vol. 7, no. 2, pp. 52-62, Mar.-Apr. 2009.

[3] F. Li, W. Qiao, H. Sun, H. Wan, J. Wang, Y. Xia, Z. Xu, and P. Zhang, "Smart transmission grid: Vision and framework," *IEEE Transactions on Smart Grid*, vol. 1, no. 2, pp.168-177, Sep. 2010.

[4] U.S. Department of Energy, "The smart grid: An introduction", 2008. [Online] Available: http://energy.gov/sites/prod/files/oeprod/DocumentsandMedia/DOE_SG_Book_Single_Pages%281%29.pdf

[5] U.S. Department of Energy, "Smart Grid", 2013. [Online] Available: http://energy.gov/oe/services/technology-development/smart-grid

[6] Electric Power Research Institute, "Smart Grid". [Online] Available: http://smartgrid.epri.com/Index.aspx

[7] National Institute of Standards and Technology, "Smart Grid: A Beginner's Guide". [Online] Available: http://www.nist.gov/smartgrid/beginnersguide.cfm

[8] European Commission, "European technology platform smart-grids: Vision and strategy for Europe's electricity networks of the future", 2006. [Online] Available: http://ec.europa.eu/research/energy/pdf/smartgrids_en.pdf.

[9] Z. Liu, *Global Energy Interconnection*, Academic Press, 2015.

[10] S. Rahman and M. Pipattanasomporn, "Smart grid information Clearinghouse: Overview of projects and deployment experience," in *Proc. IEEE PES Conference on ISTG Latin America*, 2011, pp.1-7.

[11] Y. Liu, S. Gao, H. Cui, and L. Yu, "Probabilistic load flow considering correlations of input variables following arbitrary distributions," *Electric Power Systems Research*, in Press.

[12] X. Fang, F. Li, Y. Wei, and Q. Hu, "Strategic CBDR bidding considering FTR and wind power," *IET Generation, Transmission and Distribution*, in Press.

[13] J. Xiao, Z. Zhang, L. Bai, H. Liang, "Determination of the optimal installation site and capacity of battery energy storage system in distribution network integrated with distributed generation," *IET Generation Transmission and Distribution*, vol.10, no.3, pp. 601-607, 2016.

[14] X. Fang, F. Li, Y. Wei, R. Azim, and Y. Xu, "Reactive power planning under high penetration of wind energy using benders decomposition," *IET Generation, Transmission and Distribution*, vol. 9, issue 14, pp. 1835-1844, Nov. 2015.

[15] L. Bai, T. Jiang, F. Li, H. Jia, Q. Shi, H. Chen, and G. Li, "Confidence interval estimates for loading margin sensitivity for voltage stability monitoring in the presence of renewable energy," in *Proc. 2016 IEEE PES General Meeting*, pp. 1-5.

[16] J. A. Weber, W. Gao, X. Kou, and J. Z. Zhai, "Small scale mobile hybrid integrated renewable energy system (HI-RES) for rapid recovery and emergency response," in *Proc. 2015 7th Annual IEEE Green Technologies Conference*, pp. 50-57.

[17] Q. Shi, H. Hu, W. Xu, and J. Yong, “Low-order harmonic characteristics of photovoltaic inverters,” *International Transactions on Electrical Energy Systems*, vol. 26, no. 2, pp. 347-364, Feb. 2016.

[18] J. Xiao, L Bai, Z Lu, and K Wang, “Method, implementation and application of energy storage system designing,” *International Transactions on Electrical Energy Systems*, vol. 24, no. 3, pp. 378-394, 2014.

[19] H. Hu, Q. Shi, Z. He, J. H, and S. Gao, “Potential harmonic resonance impacts of PV inverter filters on distribution systems,” *IEEE Transactions on Sustainable Energy*, vol.6, no.1, pp.151-161, Jan. 2015.

[20] J. Xiao, L. Bai, F. Li, H. Liang, and C. Wang, “Sizing of energy storage and diesel generators in an isolated microgrid using discrete fourier transform (DFT),” *IEEE Transactions on Sustainable Energy*, vol. 5, no. 3, pp. 907-916, Jul. 2014.

[21] Y. Xu, F. Li, Z. Jin, and M. Hassani Variani, “Dynamic gain-tuning control (DGTC) approach for AGC with effects of wind power,” *IEEE Transactions on Power Systems*, in Press.

[22] Y. Xu, F. Li, Z. Jin, and C. Huang, “Flatness-based adaptive control (FBAC) for STATCOM,” *Electric Power Systems Research*, vol. 122, pp. 76-85, May 2015.

[23] Y. Xu and F. Li, “Adaptive PI control of STATCOM for voltage regulation,” *IEEE Transactions on Power Delivery*, vol. 29, no. 3, pp. 1002-1011, June 2014.

[24] Z. Zhao, J. Zhao, and C. Huang, “An improved capacitor voltage balancing method for five-level diode-clamped converters with high modulation index,” *IEEE Transactions on Power Electronics*, vol. 31, no. 4, pp. 3189-3202, Apr. 2016.

[25] J. Mei, et al, “Balancing control scheme for modular multilevel converters using virtual loop mapping with fault-tolerance capabilities,” *IEEE Transactions on Industrial Electr*onics, vol. 63, no. 1, pp. 38-48, Jan. 2016.

[26] X. Shi, B. Liu, Z. Wang, Y. Li, L. Tolbert, and F. Wang, “Modeling, control design, and analysis of a startup scheme for modular multilevel converters,” *IEEE Transactions on Industrial Electronics*, vol. 62, no. 11, pp. 7009-7024, Nov. 2015.

[27] X. Shi, Z. Wang, B. Liu, Y. Liu, L. Tolbert, and F. Wang, “Characteristic investigation and control of modular multilevel converter based HVDC system under single-line-to-ground fault conditions,” *IEEE Transactions on Power Electronics*, vol. 30, no. 1, pp. 408-421, Jan. 2015.

[28] J. Mei, Y. Ji, X. Du, T. Ma, C. Huang, and Q. Hu, “Quasi-fixed-frequency hysteresis current tracking control strategy for modular multilevel converters,” *Journal of Power Electronics*, vol. 14, no.6, pp. 1147-1156, Nov. 2014.

[29] T. Jiang, H. Jia, H. Yuan, N. Zhou, and F. Li, “Projection pursuit: A general methodology of wide-area coherency detection in bulk power grid,” *IEEE Transactions on Power Systems*, vol. 31, no. 4, pp. 2776–2786, July 2016.

[30] H. Yuan, T. Jiang, H. Jia, F. Li, Y. Mishra, H. Chen, and G. Li, “Real-time wide-area loading margin sensitivity (WALMS) in power systems,” in *Proc. 2015 IEEE PES General Meeting*, pp. 1-5.

[31] H. Cui, F. Li, Q. Hu, L. Bai, and X. Fang, "Day-ahead coordinated operation of utility-scale electricity and natural gas networks considering demand response based virtual power plants," *Applied Energy*, vol.176, no. 15, pp. 183-195, Aug. 2016.

[32] L. Bai, F. Li, H. Cui, T. Jiang, H. Sun, and J. Zhu, "Interval optimization based operating strategy for gas-electricity integrated energy systems considering demand response and wind uncertainty," *Applied Energy*, vol. 167, pp. 270-279, Apr. 2016.

[33] H. Cui, F. Li, X. Fang, and R. Long, "Distribution network reconfiguration with aggregated electric vehicle charging strategy," in *Proc. 2015 IEEE PES General Meeting*, pp. 1-5.

[34] R. Torquato, Q. Shi, W. Xu, and W. Freitas, "A Monte Carlo simulation platform for studying low voltage residential networks," *IEEE Transactions on Smart Grid*, vol.5, no.6, pp.2766-2776, Nov. 2014.

[35] M. Mahmoudi, J. Dong, K. Tomsovic, and S. Djouadi, "Application of distributed control to mitigate disturbance propagations in large power networks," in *Proc. 2015 North American Power Symposium*, pp. 1-6.

[36] X. Ma, J. Dong, S. M. Djouadi, J. J. Nutaro, and T. Kuruganti, "Stochastic control of energy efficient buildings: A semidefinite programming approach," in *Proc. 2015 IEEE International Conference on Smart Grid Communications*, pp. 780-785.

[37] Q. Hu and F. Li, "Hardware design of smart home energy management system with dynamic price response," *IEEE Transactions on Smart Grid*, vol. 4, no. 4, pp. 1878-1887, Dec. 2013.

[38] X. Li and F. Li, "Estimation of the largest eigenvalue in Chebyshev preconditioner for parallel conjugate gradient method based power flow computation," *IET Generation, Transmission and Distribution*, vol. 10, no. 1, pp. 123-130, Jan. 2016.

[39] X. Li and F. Li, "GPU-based power flow analysis with Chebyshev preconditioner and conjugate gradient method," *Electric Power Systems Research*, vol. 116, pp. 87-93, Nov. 2014.

[40] C. Zhu, C. Huang, J. Zheng, and Y. Yue, "Real-time measurement of communication subsystem of intelligent electronic devices," in *Proc. 2011 International Conference on ICEICE*, pp. 626-629.

[41] C. Huang, F. Li, and Z. Jin, "Maximum power point tracking strategy for large-scale wind generation systems considering wind turbine dynamics," *IEEE Transactions on Industrial Electronics*, vol. 62, no. 4, pp. 2530-2539, Apr. 2015.

[42] C. Huang, F. Li, T. Ding, Z. Jin, and X. Ma, "Second-order cone programming-based optimal control strategy for wind energy conversion systems over complete operating regions," *IEEE Transactions on Sustainable Energy*, vol. 6, no.1, pp. 263-271, Jan. 2015.

[43] Z. Jin and C. Huang, "DFIG voltage control based on dynamically adjusted control gains," *Journal of Power and Energy Engineering*, vol. 2, no. 8, pp. 45-58, Aug. 2014.

[44] C. Huang, F. Li, T. Ding, Y. Jiang, J. Guo, and Y. Liu, "A bounded model of the communication delay for system integrity protection systems (SIPS)," *IEEE Transactions on Power Delivery*, vol. 31 no. 4, pp. 1921-1933, Aug 2016.

[45] C. Huang, et al, “Data quality issues for synchronous applications Part I: A review,” *Journal of Modern Power System and Clean Energy*, vol. 4, no. 3, pp. 342–352, July 2016.

[46] C. Huang, et al, “Data quality issues for synchronous applications Part II: Problem formulation and potential solutions,” *Journal of Modern Power System and Clean Energy*, vol. 4, no. 3, pp. 353–361, July 2016.

[47] C. Huang, et al, “LabVIEW FPGA based power system digital simulator for electromagnetic transient and electromechanical transient programs,” in *Proc. 2016 IEEE PES Asia-Pacific Power and Energy Engineering Conference*, submitted.

[48] C. Huang, Y. Xu, C. Harley, D. Masters, and F. Li, “LabVIEW FPGA based electromagnetic transient simulator using nodal analysis methods and state-space analysis methods,” in *Proc. 2015 International Conference on Electric Utility Deregulation and Restructuring and Power Technologies*, pp. 1-5.

[49] J. Guo, et al, “An ensemble photovoltaic power forecasting model through statistical learning of historical weather dataset,” in *Proc. 2016 IEEE PES General Meeting, pp. 1-5.*

[50] T. Ding, et al, “Interval arithmetic based optimal curtailment for infeasibility of SCED in the presence of wind power uncertainty,” in *Proc. 2015 IEEE PES General Meeting*, pp.1-5.

[51] S. Heier, *Grid Integration of Wind Energy Conversion Systems*, Wiley, 2006.

[52] F. D. Bianchi, H. Battista, and R. J. Mantz, *Wind Turbine Control Systems: Principles, Modeling and Gain Scheduling Design*. Springer Verlag, 2007.

[53] L. Fan and Z. Miao, *Modeling and Analysis of Doubly Fed Induction Generator Wind Energy Systems*, Elsevier Limited, Oxford, 2015.

[54] P. Wu, B. Xia, J. Pienaa, and X. Zhao, “The past, present and future of carbon labelling for construction materials-a review,” *Building and Environment*, vol. 77, pp. 160-168, July 2014.

[55] P. Wu, B. Xia, and X. Zhao, “The importance of use and end-of-life phases to the life cycle greenhouse gas (GHG) emissions of concrete - A review,” *Renewable and Sustainable Energy Reviews*, vol. 37, pp. 360-369, Sep. 2014.

[56] The Global Wind Energy Council (GWEC): Global Wind Statistics, 2015. [Online] Available: http://www.gwec.net/wp-content/uploads/vip/GWEC-PRstats-2015_LR.pdf

[57] I. Munteanu, A. I. Bratcu, N. A. Cutululis, and E. Ceanga, *Optimal Control of Wind Energy Systems: Towards a Global Approach*, Springer-Verlag 2008.

[58] E. H. Camm, et al, “Characteristics of wind turbine generators for wind power plants,” in *Proc. 2009 IEEE PES General Meeting*, pp. 1-5.

[59] D. Zhou, F. Blaabjerg, T. Franke, M. Tonnes, and M. Lau, “Comparison of wind power converters reliability with low-speed and medium-speed permanent-magnet synchronous generators,” *IEEE Transactions on Industrial Electronics*, vol. 62, no. 10, pp. 6575–6584, Oct. 2015.

[60] Y. Zhao, C. Wei, Z. Zhang, and W. Qiao, "A review on position/speed sensorless control for permanent-magnet synchronous machine-based wind energy conversion systems," *IEEE Journal of Emerging and Selected Topics in Power Electronics*, vol. 1, no. 4, pp. 203–216, Dec. 2013.

[61] A. G. Phadke and J. S. Thorp, *Synchronized Phasor Measurements and Their Applications*, New York: Springer, 2008.

[62] J. De La Ree, V. Centeno, J. S. Thorp, and A. G. Phadke, "Synchronized phasor measurement applications in power systems," *IEEE Transactions on Smart Grid*, vol. 1, no. 1, pp. 20–27, June 2010.

[63] V. Terzija, G. Valerde, D. Cai, P. Regulski, V. Mandani, J. Fitch, S. Skok, M. Begovic, and A. Phadke, "Wide-area monitoring, protection, and control of future electric power networks," *Proc. IEEE*, vol. 99, no. 1, pp. 80–93, Jan. 2011.

[64] K. Tomsovic, D. Bakken, V. Venkatasubramanian, and A. Bose, "Designing the next generation of real-time control, communication, and computations for large power systems", *Proc. IEEE*, vol. 93, no. 5, pp. 965–979, May 2005.

[65] NASPI, NASPI 2014 Survey of Synchrophasor System Networks - Results and Findings, July 2015, United States. [Online] Available: https://www.naspi.org/documents

[66] Y. Liu, et al., "Wide-area measurement system development at the distribution level: an FNET/GridEye example," *IEEE Transactions on Power delivery*, vol. 31, no. 2, pp. 721-731, April 2016.

[67] Y. Liu, et al, "Recent developments of FNET/GridEye – A situational awareness tool for the smart grid," *CSEE Journal of Power and Energy Systems*, in Press.

[68] H. Liu, et al, "ARMAX-based transfer function model identification using wide-area measurement for adaptive and coordinated damping control," *IEEE Transactions on Smart Grid*, in Press.

[69] D. Zhou, et al, "Distributed data analytics platform for wide-area synchrophasor measurement systems," *IEEE Transactions on Smart Grid*, in Press.

[70] J. Guo et al., "Design and implementation of a real-time off-grid operation detection tool from a wide-area measurements perspective," *IEEE Transactions on Smart Grid*, vol. 6, no. 4, pp. 2080-2087, July 2015.

[71] K. E. Johnson, "Adaptive torque control of variable speed wind turbines," *Natl. Renew. Energy Lab., Golden, CO, NREL/TP-500-36265*, Aug. 2004.

[72] K. E. Johnson, L. Y. Pao, M. Balas, and L. Fingersh, "Control of variable speed wind turbines: standard and adaptive techniques for maximizing energy capture," *IEEE Control Systems Magazine*, vol. 26, no. 3, pp. 70–81, Jun. 2006.

[73] Z. Chen, J. M. Guerrero, and F. Blaabjerg, "A review of the state of the art of power electronics for wind turbines," *IEEE Transactions on Power Electron*., vol. 24, no. 8, pp.1859–1875, Aug. 2009.

[74] E. A. Bossanyi, "The design of closed loop controllers for wind turbines," *Wind Energy*, vol. 3, pp. 149-163, 2000.

[75] Y. Mishra, S. Mishra, F. Li, Z. Y. Dong, and R. C. Bansal, "Small-signal stability analysis of a DFIG-based wind power system under different modes of operation," *IEEE Transactions on Energy Conversion*., vol. 24, no. 4, pp. 972-982, Dec. 2009.

[76] E. B. Muhando, T. Senjyu, A. Uehara, T. Funabashi, and C. Kim, "LQG design for megawatt-class WECS with DFIG based on functional models fidelity prerequisites," *IEEE Transactions on Energy Conversion*, vol. 24, no. 4, pp. 893-904, Dec. 2009.

[77] F. D. Bianchi, R. J. Mantz, and C. F. Christiansen, "Control of variable-speed wind turbines by LPV gain scheduling," *Wind Energy*, vol. 7, pp.1-8, 2004.

[78] M. Soliman, O. P. Malik, and D. T. Westwick, "Multiple model multiple-input multiple-output predictive control for variable speed variable pitch wind energy conversion systems," *IET Renewable Power Generation*, vol. 5, no. 2, pp. 124-136, 2011.

[79] M. Soliman, O. P. Malik, and D. T. Westwick, "Multiple model predictive control for wind turbines with doubly fed induction generators," *IEEE Transactions on Sustain. Energy*, vol. 2, no. 3, pp. 215-225, Jul. 2011.

[80] Z. Jin, F. Li, X. Ma, and S. M. Djouadi, "Semi-definite programming for power output control in wind energy conversion system," *IEEE Transactions on Sustain. Energy*, vol. 5, no. 3, pp. 466-475, Apr. 2014.

[81] *IEEE Standard for Synchrophasers for Power Systems*, IEEE Std. 1344-1995(R2001), 1995.

[82] *IEEE Standard for Synchrophasors for Power Systems*, IEEE Std. C37.118-2005 (Revision of IEEE Std 1344-1995), 2006.

[83] *IEEE Standard for Synchrophasor Measurements for Power Systems*, IEEE Std. C37.118.1-2011, 2011.

[84] *IEEE Standard for Synchrophasor Data Transfer for Power Systems*, IEEE Std. C37.118.2-2011, 2011.

[85] *IEEE Guide for Synchronization, Calibration, Testing, and Installation of Phasor Measurement Units (PMUs) for Power System Protection and Contro*l, IEEE Std C37.242-2013, March 2013.

[86] *IEEE Guide for Phasor Data Concentrator Requirements for Power System Protection, Control, and Monitoring*, IEEE Std. C37.244- 2013, May 2013.

[87] K. E. Martin, "Synchrophasor standards and guides for the smart grid," in *Proc. 2013 IEEE PES General Meeting*, pp. 1-5, 2013.

[88] K. E. Martin et al., "Exploring the IEEE standard C37.118-2005 synchrophasors for power systems," *IEEE Transactions on Power Del*ivery, vol. 23, no. 4, pp. 1805–1811, Oct. 2008.

[89] K. E. Martin et al., "An overview of the IEEE standard C37.118.2—Synchrophasor data transfer for power systems," *IEEE Transactions on Smart Grid*, vol. 5, no. 4, pp. 1980-1984, July 2014.

[90] K. E. Martin, "Synchrophasor measurements under the IEEE standard C37.118.1-2011 with amendment C37.118.1a," *IEEE Transactions on Power Del*ivery, vol. 30, no. 3, pp. 1514–1522, Jun. 2015.

[91] NASPI (2008 and accessed October 12, 2014), Phasor application classification. [Online]. Available: https://www.naspi.org/File.aspx?fileID=604

[92] NASPI (2009), Actual and potential phasor data applications. [Online]. Available: https://www.naspi.org/File.aspx?fileID=537

[93] NERC (2010), Real-time applications of synchrophasors for improving reliability. [Online]. Available: https://www.naspi.org/File.aspx?fileID=519

[94] NASPI (2015), Synchrophasor maturity model [Online]. Available: https://www.naspi.org/File.aspx?fileID=1496

[95] NASPI (2015 draft), Categorizing phasor measurement units by application data requirements [Online]. Available: https://www.naspi.org/home

[96] C. Huang, J. Zheng, L. Su, and J. Mei, "Configuration of electronic transformers," *Electric Power Automation Equipment*, vol. 30, no. 3, pp. 137-140, 2010.

[97] C. Zhu, C. Huang, J. Mei, and J. Zheng, "Design of smart merging unit based on FPGA and ARM," *Power System Technology*, vol. 35, no.6, pp 10-14, 2011.

[98] I. Kamwa, S. R. Samantaray, and G. Joos, "Wide frequency range adaptive phasor and frequency PMU algorithms," *IEEE Transactions on Smart Grid*, vol. 5, no. 2, pp. 569–579, Mar. 2014.

[99] L. Zhan, Y. Liu, J. Culliss, J. Zhao, and Y. Liu, "Dynamic single-phase synchronized phase and frequency estimation at the distribution level," *IEEE Transactions on Smart Grid*, vol. 6, no. 4, pp. 2013-2022, July 2015.

[100] L. Zhan, Y. Liu, and Y. Liu, "A Clarke transformation-based DFT phasor and frequency algorithm for wide frequency range," *IEEE Transactions on Smart Grid*, vol. pp, no. 99, pp. 1-1, 2016.

[101] F. Zhang, Y. Sun, L. Cheng, X. Li, J. H. Chow, and W. Zhao, "Measurement and modeling of delays in wide-area closed-loop control systems," *IEEE Transactions on Power Systems*, vol. 30, no. 5, pp. 2426-2433, Sept. 2015.

[102] C. Huang, C. Xiao, Y. Fang, and J. Zheng, "A method to deal with packet transfer delay of sampled value in smart substation," *Power System Technology*, vol. 35, no. 1, pp. 5–10, 2011.

[103] N. T. Anh, L. Vanfretti, J. Driesen, and D. Van Hertem, "A quantitative method to determine ICT delay requirements for wide-area power system damping controllers," *IEEE Transactions on Power Systems*, vol. 30, no. 4, pp. 2023-2030, July 2015.

[104] F. Bai, et al., "Measurement-based correlation approach for power system dynamic response estimation," *IET Generation, Transmission & Distribution*, vol.9, no.12, pp.1474-1484, Sept. 2015.

[105] X. Zhao, Y. Sun, N. Li, Z. Wei, G. Sun, and C. Huang, "Robust H_∞ load frequency control of delayed multi-area power system with stochastic disturbances," *Neurocomputing*, vol. 193, pp. 58-6712, June 2016.

[106] K. Zhu, M. Chenine, and L. Nordström, "ICT architecture impact on wide area monitoring and control systems' reliability," *IEEE Transactions on Power Delivery*, vol. 26, pp.2801-2808, 2011.

[107] P. Kansal and A. Bose, “Bandwidth and latency requirements for smart transmission grid applications,” *IEEE Transactions on Smart Grid*, vol. 3, no. 3, pp. 1344-1352, 2012.

[108] Y. Wang, W. Li, and J. Lu, “Reliability analysis of wide-area measurement system,” *IEEE Transactions on Power Delivery,* vol. 25, no. 3, pp. 1483–1491, Jul. 2010.

[109] K. Zhu and L. Nordström, “Design of wide-area damping systems based on the capabilities of the supporting information communication technology infrastructure,” *IET Generation, Transmission & Distribution*, vol. 8, no. 4, pp. 640-650, 2014.

[110] D. Duan, L. Yang, and L. L. Scharf, “Phasor state estimation from PMU measurements with bad data,” in *Proc. IEEE Workshop on CAMSAP 2011*, pp. 121-124.

[111] S. Zhang and V. Vittal, “Design of wide-area power system damping controllers resilient to communication failures,” *IEEE Transactions on Power Systems*, vol. 28, no. 4, pp. 4292-4300, Nov. 2013.

[112] P. Gao, M. Wang, S. G. Ghiocel, J. H. Chow, B. Fardanesh, and G. Stefopoulos, “Missing data recovery by exploiting low-dimensionality in power system synchrophasor measurements,” *IEEE Transactions on Power Systems*, vol. 31, no. 2, pp. 1006–1013, Mar. 2016.

[113] K. Tan and S. Island, “Optimum control strategies in energy conversion of PMSG wind turbine system without mechanical sensors,” *IEEE Transactions on Energy Conversion*, vol. 19, no. 2, pp. 392-399. Jun. 2004.

[114] M. Narayana, G. Putrus, M. Jovanovic, and P. S. Leung, “Predictive control of wind turbines by considering wind speed forecasting techniques,” *in Proc. 44th International Universities Power Engineering (UPEC*), Glasgow, pp. 1–4, Sept. 2009.

[115] A. G. Abo-Khalil and D.-C. Lee, “MPPT control of wind generation systems based on estimated wind speed using SVR,” *IEEE Trans. Ind. Electron.*, vol. 55, no. 3, pp. 1489–1490, Mar. 2008.

[116] W. Qiao, X. Yang, and X. Gong, “Wind speed and rotor position sensorless control for direct-drive PMG wind turbines,” *IEEE Trans. Ind. Appl.*, vol. 48, no. 1, pp. 3–11, Jan./Feb. 2012.

[117] C. W. Potter, and M. Negnevitsky, “Very short-term wind forecasting for Tasmanian power generation,” *IEEE Transactions on Power Systems*, vol. 21, no. 2, pp. 965–972, May 2006.

[118] J. Zeng and W Qiao, “Short-term wind power prediction using a wavelet support vector machine,” *IEEE Transactions on Sustainable Energy*, vol. 3, no. 2, pp. 255–264, Apr. 2012.

[119] G. Zhang, H. Li, and M. Gan, “Design a wind speed prediction model using probabilistic fuzzy system,” *IEEE Transactions on Ind. Inf.*, vol. 8, no. 4, pp. 819–827, Nov. 2012.

[120] D. Bertsimas and D. Brown, “Constrained stochastic LQC: A tractable approach,” *IEEE Transactions on Automatic Control*, vol. 52, no. 10, pp. 1826–1841, Oct. 2007.

[121] DL/T 364–2010 General Specification of Transmitting Protection Information on Optical Channel, China Electricity Council, 2010.

[122] W. Zhang, “Calculation and analysis about transmission time delay of SDH self-healing loop network,” *Telecommunications for Electric Power System*, vol. 26, no. 154, pp. 56–60, Aug, 2005.

[123] N.-K. C. Nair and D.L.P Jenkins, “IEC 61850 enabled automatic bus transfer scheme for primary distribution substations,” *IEEE Trans. Smart Grid*, vol. 4, no. 4, pp. 1821–1828, Dec. 2013.

[124] Y. Jiang, “Network calculus and queueing theory: two sides of one coin,” in *Proc. of 4th International Conference on Performance Evaluation Methodologies and Tools (VALUETOOLS)*, 2009, pp. 1-11.

[125] Y. Jiang and Y. Liu, *Stochastic Network Calculus*. Springer, 2008

[126] R. L. Cruz. “A calculus for network delay, part I and part II”. *IEEE Trans. Information Theory*, vol. 37, no. 1, pp. 114–141, Jan. 1991.

[127] J.-Y. Le Boudec and P. Thiran. *Network Calculus: A Theory of Detministic Queueing Systems for the Internet*. Springer-Verlag, 2001.

[128] Y. Jiang. “Delay Bounds for a Network of Guaranteed Rate Servers with FIFO Aggregation,” *Computer Networks*, vol. 40, no. 6, pp. 683-694, 2002.

[129] H. Georg, N. Dorsch, M. Putzke, and C. Wietfeld, “Performance evaluation of time-critical communication networks for smart grids based on IEC 61850,” in *Proc. 2013 IEEE INFOCOM*, pp. 143–148.

[130] N. Dorsch, H. Georg, and C. Wietfeld, “Analyzing the real-time-capability of wide area communication in smart grids,” in *Proc. 2014 IEEE INFOCOM*, pp. 682-687.

[131] T. Ding, K. Sun, C. Huang, Z. Bie, and F. Li, “Mixed integer linear programming-based splitting strategies for power system islanding operation considering network connectivity,” *IEEE Systems Journal*, in Press.

[132] L. Yang, J. Wang, Y. Ma, J. Wang, X. Zhang, L. M. Tolbert, F. Wang and K. Tomsovic, “Three-phase power converter based real-time synchronous generator emulation,” *IEEE Transactions on Power Electronics*, in Press.

[133] L. Yang, et al, “Development of converter based reconfigurable power grid emulator,” in *Proc. 2014 IEEE Energy Conversion Congress and Exposition*, pp. 3990-3997.

[134] J. Wang, et al, “Regenerative power converters representation of grid control and actuation emulator,” in *Proc. 2012 IEEE Energy Conversion Congress and Exposition*, pp. 2460-2465.

[135] F. Hu, K. Sun, A. D. Rosso, E. Farantatos, and N. Bhatt, “Measurement-based real-time voltage stability monitoring for load areas,” *IEEE Transactions on Power Systems*, vol. 31, No. 4, pp. 2787-2798, July 2016

[136] B. Wang and K. Sun, “Formulation and characterization of power system electromechanical oscillations,” *IEEE Transactions on Power Systems*, in Press.

[137] J. Qi, W. Ju, and K. Sun, “Estimating the propagation of interdependent cascading outages with multi-type Branching processes,” *IEEE Transactions on Power Systems*, in Press.

[138] T. Jiang, L. Bai, F. Li, H. Jia, Q. Hu, and X. Jin, “Synchrophasor measurement-based correlation approach for dominant mode identification in bulk power systems,” *IET Generation, Transmission and Distribution*, in Press.

[139] T. Jiang, H. Yuan, H. Jia, N. Zhou, and F. Li, "Stochastic subspace identification-based approach for tracking inter-area oscillatory modes in bulk power system utilizing synchrophasor measurements," *IET Generation, Transmission and Distribution*, vol. 9, no. 15, pp. 2409-2418, 2015.

[140] M. Mahmoudi, J. Dong, K. Tomsovic, and S. Djouadi, "Application of distributed control to mitigate disturbance propagations in large power networks," in *Proc. 2015 North American Power Symposium (NAPS)*, pp. 1-6.

[141] D. Jin, X. Ma, S. M. Djouadi, H. Li and T. Kuruganti, "Real-time prediction of power system frequency in FNET: A state space approach," in *Proc. 2013 IEEE International Conference on Smart Grid Communications*, pp. 109-114.

[142] J. Dong, X. Ma, S. M. Djouadi, H. Li and Y. Liu, "Frequency rrediction of power systems in FNET based on state-space approach and uncertain basis functions," *IEEE Transactions on Power Systems*, vol. 29, no. 6, pp. 2602-2612, Nov. 2014.

Appendix

A. Network Calculus Methods

This appendix presents how the two delay bounds discussed in Section 4.3 are derived based on the network calculus theory. To clearly explain the derivation in the limited space, some assumptions and simplifications are made as follows:

(1) The switched Ethernet network in each substation adopts a spanning tree protocol to route traffic. This is a standard setup for Ethernet networks to avoid traffic looping in the network.

(2) Without loss of generality, we assume that the resultant spanning tree for each substation network is the tree where the root switch 1 (RS1) is on the root, all S-bay, T1-bay, T2-bay, F1-bay, …, F5-bay switches are children nodes of the RS1, and MU/BC/IED elements are children nodes of their corresponding S-bay/T1-bay/T2-bay/F1-bay, …,/F5-bay node.

(3) The broadcast feature of Ethernet is adopted for an MU/BC/IED to send messages. This implies that every packet sent by an MU/BC/IED will be received by all other MU/BC/IEDs, as well as the gateway, in the network. As a result, the network operates in the worst case, in terms of traffic load.

(4) In each switch, the messages of different types are served in the priority scheduling manner, whereas the messages of the same type are served in the FIFO manner. Also, the buffer size of each switch is large enough ensuring no packet loss when the traffic is constrained ($r_j^i \leq R_j^i$).

(5) For simplicity in expression, we assume that every MU sends SV messages and every bay is config.d with one IED.

(6) The propagation delay within the substation is ignored.

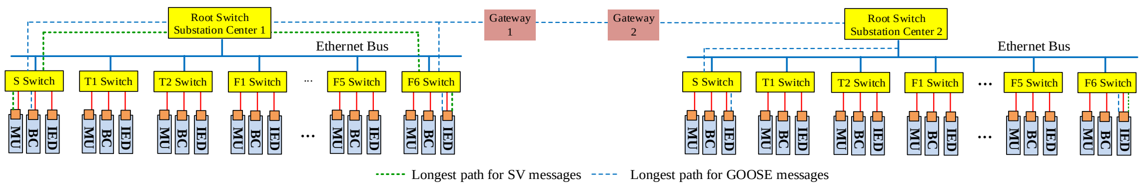

Fig. A1. Diagram of network connection of two substations.

A. Delay Bound for the Single Substation Case

In this case, the longest path for SV messages and the longest path for GOOSE messages are considered for the worst-case analysis, which are MU→S→RS1→F6→IED, and BC/IED →S→RS1→F6→IED, respectively. An illustration of these two paths can be found in Fig. A1.

Step 1: Considering GOOSE has higher priority than SV, the potential effect of GOOSE on the service provided to SV at each link is identified first. This effect in the network calculus theory is dependent on the (worst-case) bustiness of GOOSE traffic, and captured by the arrival curves as follows

$$\alpha_{S/T1/T2/F1/.../F5}^{GS}(t) = 2r^{GS} \cdot t + 2L^{GS} \tag{A1}$$

$$\alpha_{BC \to F6}^{GS}(t) = r^{GS} \cdot t + L^{GS} \tag{A2}$$

$$\alpha_{S/T1/T2/F1/.../F5 \to RS}^{GS}(t) = 2r^{GS} \cdot t + 2L^{GS} + 2r^{GS} \times \tfrac{L}{C} \tag{A3}$$

$$\alpha_{RS}^{GS}(t) = \alpha_{S+...+F5 \to RS}^{GS}(t) = 16r^{GS} \cdot t + (16L^{GS} + 16r^{GS} \times \tfrac{L}{C}) \tag{A4}$$

$$\alpha_{RS \to F6}^{GS}(t) = 16r^{GS} \cdot t + (16L^{GS} + 16r^{GS} \times \tfrac{L}{C} + 16r^{GS} \times \tfrac{L}{C}) \tag{A5}$$

$$\begin{aligned} \alpha_{F6}^{GS}(t) &= \alpha_{RS \to F6}^{GS}(t) + \alpha_{BC \to F6}^{GS}(t) \\ &= 17r^{GS} \cdot t + (17L^{GS} + 32r^{GS} \times \tfrac{L}{C}) \end{aligned} \tag{A6}$$

where α_n^{GS} denotes the arrival curve of GOOSE messages entering each node *n* on the path. *L* denotes max (L^{GS}, L^{SV}).

Step 2: With the effect of GOOSE traffic above, the minimum amount of service that SV traffic may receive at each node *n* is characterized using the service curve β_n^{SV} as

$$\beta_{S/T1/T2/F1/.../F6/RS}(t) = C(t - \tfrac{L}{C})^{+} \tag{A7}$$

$$\beta_{S/T1/T2/F1/.../F5}^{SV}(t) = (C - 2r^{GS})(t - \frac{L + 2L^{GS}}{C - 2r^{GS}})^{+} \tag{A8}$$

$$\begin{aligned}\beta_{RS}^{SV}(t) &= \beta_{RS}(t) - \alpha_{RS}^{GS}(t) \\ &= (C - 16r^{GS})(t - \frac{L + 16L^{GS} + 16L^{GS} \times \frac{L}{C}}{C - 16r^{GS}})^{+}\end{aligned} \tag{A9}$$

$$\begin{aligned}\beta_{F6}^{SV}(t) &= \beta_{F6}(t) - \alpha_{F6}^{GS}(t) \\ &= (C - 17r^{GS})(t - \frac{L + 17L^{GS} + 32L^{GS} \times \frac{L}{C}}{C - 17r^{GS}})^{+}\end{aligned} \tag{A10}$$

Step 3: Accordingly, the arrival curves of SV messages α_n^{SV} at each node *n* can be written in (A11) to (A13).

$$\alpha_{S/T1/T2/F1/.../F6}^{SV}(t) = r^{SV} \cdot t + L^{SV} \tag{A11}$$

$$\alpha_{T1/T2/F1/.../F5 \to RS}^{SV}(t) = r^{SV} \cdot t + L^{SV} + L + 2L^{GS} \tag{A12}$$

$$\alpha_{T1+T2+F1+...+F5 \to RS}^{SV}(t) = 7r^{SV} \cdot t + 7L^{SV} + 7L + 14L^{GS} \tag{A13}$$

Step 4: In this step, an end-to-end service curve for the SV traffic crossing the whole end-to-end path is obtained. The idea here is to take consideration of the effect of FIFO scheduling due to the SV traffic that later joins and shares the longest path. There are two sub-steps.

First, let's view RT+F6 as a virtual server to all SV traffic sharing RS1→F6→IED, where the FIFO effect for the SV traffic generated by MU connected to F6 is taken out.

$$\beta_{RS\rightarrow F6}^{SV}(t)=(\mathrm{C}-17r^{GS}-r^{SV}) \times\left(t-\frac{L+17L^{GS}+32r^{GS}\times\frac{L}{C}}{C-17r^{GS}-r^{SV}}-\frac{L^{SV}}{C-17r^{GS}}\right)^{+} \tag{A14}$$

$$\beta_{RS}^{SV}\otimes\beta_{RS\rightarrow F6}^{SV}(t)=(\mathrm{C}-17r^{GS}-r^{SV}) \times\left(t-\frac{2L+33L^{GS}+48r^{GS}\times\frac{L}{C}}{C-17r^{GS}-r^{SV}}-\frac{L^{SV}}{C-17r^{GS}}\right)^{+} \tag{A15}$$

At the second sub-step, we first take out the FIFO effect from SV traffic generated by MUs connected to T1, T2, F1, … , and F5, at the virtual server RS1+F6, and we denote the obtained service curve by $\beta^{SV-Path}$. Then, we integrate it with the S-bay switch on the path, and use network calculus concatenation property to obtain the end-to-end service curve for the SV traffic crossing the whole path.

$$\beta_{RS+F6}^{SV-Path}(t)=(\mathrm{C}-17r^{GS}-8r^{SV}) \times\left(t-\frac{2L+33L^{GS}+48r^{GS}\times\frac{L}{C}}{C-17r^{GS}-8r^{SV}}-T_2-T_3\right)^{+} \tag{A16}$$

$$\beta_{Path}^{SV}(t)=\beta_{S}^{SV}\otimes\beta_{RS+F6}^{SV-Path}(t) =(\mathrm{C}-17r^{GS}-8r^{SV})(t-T_1-T_2-T_3)^{+} \tag{A17}$$

with $T_1=\frac{3L+35L^{GS}+48r^{GS}\times\frac{L}{C}}{C-17r^{GS}-8r^{SV}}$, $T_2=\frac{7L^{SV}+7L+14L^{GS}}{C-17r^{GS}-r^{SV}}$, and $T_3=\frac{L^{SV}}{C-17r^{GS}}$.

Step 5: In the final step, the delay bound for SV traffic is easily obtained as

$$t_d^{SV}\leq\frac{L^{SV}}{C-17r^{GS}-8r^{SV}}+T_1+T_2+T_3 \tag{A18}$$

In these steps, the various network calculus results as summarized in Section III.B have been applied. Specifically, Step 1 and Step 3 are mainly based on the superposition property and the output property; Step 2 makes use of the left-over service property under priority scheduling; Step 4 relies on the service curve property under FIFO scheduling together with the concatenation property; and Step 5 is a direct application of the service guarantee analysis property.

B. Delay Bound for the Two Substation Case

In this case, GOOSE messages are transmitted between two substations. The resultant longest path becomes: BC→S→RS1 →Gateway1 (GT1)→Gateway2 (GT2)→RS2→S →IED. The analysis follows the similar steps.

Step 1: On the end-to-end path, there are two GOOSE messages flows, generated by BCs and IEDs, which share S-bay switch in the FIFO manner in Substation 1 network. Due to FIFO, both flows have the same end-to-end delay bound, and they can be treated together as one flow, whose arrival curve is

$$\alpha_S^{GS}(t) = 2r^{GS} \cdot t + 2L^{GS} \quad \text{(A19)}$$

Step 2: At the RS1, RS2, and S-bay switch in the Substation 2, there are other GOOSE message flows sharing the respective rest of the longest path in the FIFIO manner. Their arrival curves can be written as

$$\alpha_{T1+T2+F1+...+F6\to RS1}^{GS}(t) = 16r^{GS} \cdot t + 16L^{GS} + 16r^{GS} \times \tfrac{L}{C} \quad \text{(A20)}$$

$$\alpha_{T1+T2+F1+...+F6\to RS2}^{GS}(t) = 16r^{GS} \cdot t + 16L^{GS} + 16r^{GS} \times \tfrac{L}{C} \quad \text{(A21)}$$

$$\alpha_{BC\to S}^{GS}(t) = r^{GS} \cdot t + L^{GS} \quad \text{(A22)}$$

Step 3: In this step, an end-to-end service curve for the GOOSE traffic crossing the whole end-to-end path is obtained. Since GOOSE has the highest priority, the service curve for all GOOSE traffic at every node on the path is as follows

$$\beta_{S/RS1/GT1/GT2/RS2/S}^{GS}(t) = C(t - \tfrac{L}{C})^{+} \quad \text{(A23)}$$

The next is to take consideration of the effect of FIFO scheduling due to the GOOSE traffic that later joins and shares the longest path. Let's first consider the S switch for GOOSE traffic on BC→S→RS1→GT1→GT2→RS2→S, which provides the following service curve.

$$\beta_{\to S}^{GS}(t)=(C-r^{GS})(t-\frac{L}{C-r^{GS}}-\frac{L^{GS}}{C})^{+} \tag{A24}$$

Consider RS2 + S together for all GOOSE traffic that passes them on the path, whose service curve, from the concatenation property, is given by

$$\beta_{RS2+S}^{GS}(t)=(C-r^{GS})(t-\frac{2L}{C-r^{GS}}-\frac{L^{GS}}{C})^{+} \tag{A25}$$

Then for GOOSE traffic on BC→S→RS1→GT1→GT2→ RS2→S, the service curve below is provided to it by RS2 + S.

$$\beta_{\to RS2+S}^{GS}(t)=(C-17r^{GS})(t-\frac{b_1}{C-17r^{GS}}-\frac{b_2}{C-r^{GS}})^{+} \tag{A26}$$

where $b_1=2L+(C-r^{GS})\frac{L^{GS}}{C}$ and $b_2=16L^{GS}+16r^{GS}\times\frac{L}{C}$.

Third, since the GOOSE traffic through RS1, GT1 and GT2 is the same on BC→S→RS1→GT1→GT2→RS2, the service curve for it by the path is easily found based on the concatenation property as

$$\begin{aligned}\beta_{RS1+...+S}^{GS}(t)&=\beta_{RS1}^{GS}\otimes\beta_{GT1}^{GS}\otimes\beta_{GT2}^{GS}\otimes\beta_{\to RS2}^{GS}(t)\\&=(\mathrm{C}-17r^{GS})(t-\frac{3L+b_1+b_2}{C-17r^{GS}})^{+}\end{aligned} \tag{A27}$$

Fourth, at RS1, there is other GOOSE traffic, i.e. from T1/T2/F1/· · ·/F6, joining and sharing the path from RS1 using FIFO. Taking this into consideration, the service provided to GOOSE traffic that is already on the path has a service curve as

$$\beta^{GS}_{\to RS1+...+S}(t) = (\mathrm{C} - 33r^{GS}) \times (t - \frac{3L + b_1 + \frac{C-17r^{GS}}{C-r^{GS}} b_2}{C - 33r^{GS}} - \frac{b_2}{C - 17r^{GS}})^+ \quad \text{(A28)}$$

Following the similar approach, concatenating S with → RS1+ · · ·+ S, the end-to-end path provides the GOOSE traffic from BC and IED at the S-bay switch a service curve as follows

$$\beta^{GS}_{path}(t) = \beta^{GS}_{S+RS1+...+S}(t) = \beta^{GS}_{S} \otimes \beta^{GS}_{\to RS1+...+S}(t)\beta = (\mathrm{C} - 33r^{GS})(t - \frac{4L + b_1 + \frac{C-17r^{GS}}{C-r^{GS}} b_2}{C - 33r^{GS}} - \frac{b_2}{C - 17r^{GS}})^+ \quad \text{(A29)}$$

Step 4: In this step, the following bound on delay for GOOSE traffic is obtained as

$$t^{GS}_d \le \frac{2L^{GS}}{C - 33r^{GS}} + T_1 + T_2 + T_3 \quad \text{(A30)}$$

where $T_1 = \frac{4L + b_1 + \frac{C-17r^{GS}}{C-r^{GS}} b_2}{C - 33r^{GS}}$, $T_2 = \frac{b_2}{C - 17r^{GS}}$, and T_3 is the propagation delay between GT1 and GT2.

B. Selected Publications during Ph.D. Study

Journal Papers

[J1] **Can Huang**, Fangxing Li, Tao Ding, Zhiqiang Jin, and Xiao Ma, "Second-order cone programming-based optimal control strategy for wind energy conversion systems over complete operating regions," *IEEE Transactions on Sustainable Energy*, vol. 6, no.1, pp. 263-271, Jan. 2015.

[J2] **Can Huang**, Fangxing Li, and Zhiqiang Jin, "Maximum power point tracking strategy for large-scale wind generation systems considering wind turbine dynamics," *IEEE Transactions on Industrial Electronics*, vol. 62, no. 4, pp. 2530-2539, April 2015.

[J3] **Can Huang**, Fangxing Li, Jiahui Guo, and Yilu Liu, "A bounded model of the communication delay for system integrity protection systems," *IEEE Transactions on Power Delivery*, vol. 31 no. 4, pp. 1921-1933, Aug 2016.

[J4] **Can Huang**, Fangxing Li, Dao Zhou, Jiahui Guo, Zhuohong Pan, Yong Liu, and Yilu Liu, "Data quality issues for synchrophasor applications Part I: A review," *Journal of Modern Power System and Clean Energy*, vol. 4, no. 3, pp. 342–352, July 2016.

[J5] **Can Huang**, Fangxing Li, Lingwei Zhan, Yao Xu, Qinran Hu, Dao Zhou, and Yilu Liu, "Data quality issues for synchrophasor applications Part II: Problem Formulation and Potential Solutions," *Journal of Modern Power System and Clean Energy*, vol. 4, no. 3, pp. 353–361, July 2016.

[J6] Tao Ding, Kai Sun, **Can Huang**, Z. Bie, and Fangxing Li, "Mixed integer linear programming-based splitting strategies for power system islanding operation considering network connectivity," *IEEE Systems Journal*, in Press.

[J7] Yao Xu, Fangxing Li, Zhiqiang Jin, and **Can Huang**, "Flatness-based adaptive cntrol (FBAC) for STATCOM," *Electric Power Systems Research*, vol. 122, pp. 76-85, May 2015.

Conference Papers

[C1] **Can Huang**, Kumaraguru Prabakar, Fangxing Li, Bailu Xiao, Mark Buckner, Yilu Liu, and Brian MacCleery, "LabVIEW FPGA based Power System Digital Simulator for Electromagnetic Transient and Electromechanical Transient Programs," in *Proc. 2016 IEEE PES Asia-Pacific Power and Energy Engineering Conference*, submitted.

[C2] **Can Huang**, Yao Xu, Chad Harley, Drew Masters, and Fangxing Li, "LabVIEW FPGA based electromagnetic transient simulator using nodal analysis methods and state-space analysis methods," in *Proc. 2015 5th International Conference on Electric Utility Deregulation and Restructuring and Power Technologies*, pp. 1-5.

[C3] T. Ding, **C. Huang**, R. Bo, R. Li, Z. Yang, F. Li, and H. Sun, "Interval arithmetic based optimal curtailment for infeasibility of SCED in the presence of wind power uncertainty," in *Proc. 2015 IEEE PES General Meeting*, pp.1-5.

Vita

Can Huang joined The University of Tennessee at Knoxville in August 2012 to pursue the Ph.D. degree in Electrical Engineering. He received the B.S. degree from Hohai University, Nanjing, China, in 2008, and the M.S. degree from Southeast University, Nanjing, China, in 2011. His research interests include renewable energy integration, power system operation and control, and IT applications in power systems and power electronics.